MICROFLUIDIC DEVICES FOR HIGH THROUGHPUT CELL SORTING AND CHEMICAL TREATMENT

KEVIN LOUTHERBACK

A DISSERTATION
PRESENTED TO THE FACULTY
OF PRINCETON UNIVERSITY
IN CANDIDACY FOR THE DEGREE
OF DOCTOR OF PHILOSOPHY

RECOMMENDED FOR ACCEPTANCE
BY THE DEPARTMENT OF
ELECTRICAL ENGINEERING
ADVISER: JAMES C. STURM

NOVEMBER 2011

Abstract

Separation by size is a fundamental analytical and preparative technique in biology, medicine, and chemistry. Deterministic lateral displacement (DLD) arrays are microfluidic devices capable of high-precision particle sorting based on size. In this thesis, we will discuss improvements in the functionality of DLD arrays and several new applications. We'll first discuss a methodology for performing sequential on-chip chemical treatment by using the DLD array to direct particles in the "bumping" trajectory across co-flowing reagent streams and demonstrates this technique with platelet labeling and washing and *E. Coli* lysis and chromosomal separation. We then discuss a deterministic microfluidic ratchet that could separate particles in an intermediate size range using a DLD array with triangular posts in an oscillating flow. We then extended this idea of using triangular posts in DLD arrays to continuous-flow operation and showed significant performance enhancements over arrays with circular posts when the triangle vertex is used as the displacement edge. Taking this idea of increasing device throughput to the next step, we developed a highly parallelized DLD array architecture for processing macroscopic fluid volumes by operating many arrays in parallel and showed flow rates on the order of 10 mL/min with a single-layer device and applied these high throughput DLD arrays to isolating viable circulating tumor cells from blood and dewatering algae for biofuel production.

Acknowledgements

I am quite proud of the work presented in this thesis and I would like to thank the many people who have contributed, either directly or indirectly. Thanks to my advisor Jim Sturm for providing an environment where I could pursue interesting problems and for guidance when I was uncertain of what to do next. Thanks to my *de facto* co-advisor Bob Austin for always being in the lab and emphasizing the value of pursuing experiments where you do not know what the results will be. Thanks to David Inglis, Keith Morton, and Jason Puchalla for training me when I initially entered the lab and sharing ideas afterwards. Thanks to Naveen Verma for reading this thesis and providing insightful comments and suggestions.

Thanks to my colleagues and friends Guillaume, David, Andre, Liyu, John, Jonas, Amy, and Joseph who made life both in and out of the lab much more enjoyable. Thanks to my friends in Princeton Lorne, Richard, Clinton, Daniel, Eugene, Andrea, Matt, both Noahs, Yifei, Sushobhan, Aman, Abhishek, Sibren & Tanushree, Bhadri, Sri, Anthony, Devin, Andrew and Peter for the countless dinners, trips, movies, and other moments that will make me remember this time as one of the best of my life. Thanks to John Appel and the other members of Popáyan for many hours of soccer after I thought I would never play again. Thanks to my friends Andy and Ann for providing worthwhile diversions in DC and NYC and for visiting me every now and then. Thanks to my friends Andrew, Binh, Jason, David, Haamed, and Kari for making my trips back to California something to look forward to every winter. Finally, thanks for my family for their constant support and encouragement.

For my parents

Contents

Chapter 1

Introduction

1.1 Continuous Flow Separations

A key step in many analytical and preparative techniques in medicine and biology is to separate cells, functionalized beads, or other particles from a solution which may contain other undesirable elements [56]. These separations are classically performed in batch processes, such as centrifugation or filtration, which can be both time consuming and wasteful of required reagents. Borrowing from microfabrication techniques developed by integrated circuits industry, a variety of microfluidic devices have emerged in the last decade that can perform these procedures continuously with better resolution and less use of reagent. Composed of micro- and nano-scale channels defined in a bulk material (usually silicon, glass, plastic, or soft polymer), devices have been developed to separate particles by various properties including size, density, charge, magnetic and dielectric susceptibility [56].

The general principle of microfluidic devices for continuous particle flow separation is that a force applied across a microscale channel displaces particles as they move through the channel, with the magnitude of the displacement corresponding to some property of the particle. This allows particles to be separated spatially as they move through the channel and collected into desired components at the device outlet. This also allows analytical and diagnostic applications as the distribution of particles across the channel can be measured before exiting the device or off chip if they are collected in different output channels. Because it is a continuous process, there is no limit for the amount of sample that can be processed (just keep running it until desired volume has been processed) and precise injection of sample plugs is not required as in batch processes like high-performance liquid chromatography (HPLC). The particular mechanism that will be of interest in this thesis is steric repulsion between particles and obstacles in the flow channel that will selectively displace particles based on size.

Throughout most of this work, and in microfluidics in general, the concept of low Reynolds number flow is important. The Reynolds number Re is a dimensionless number used to characterize the ratio of inertial to viscous forces present in a flow. It is defined as $Re = \rho v L/\mu$, where v and L are characteristic velocities and length scales that describe the flow while ρ is the fluid density and μ is the dynamic viscosity. Low Re flows have a Reynolds number much less than one and are characterized by smooth, laminar motion. This types of flow is prevalent in the world of microorganisms, where the length scales (microns) and velocities (microns/s) are small. Similar conditions are used for the devices presented in this thesis.

Flow in this regime can be described by streamlines, which are curves that are instantaneously tangent to the velocity vector of the flow and show the direction a fluid element will travel in at any point in time. Particles suspended in the fluid will also follow streamlines unless acted on by an external force [59]. Physical intuition of low Re flow is difficult because the world we occupy is mostly characterized by high Re flows that are dominated by inertia. In our world, chaotic motion, vortices, eddies, and other flow instabilities are common and only the average trajectory of elements in a flow can be predicted [40]. This quote from Purcell is useful in giving some sense of the conditions under which low Re devices operate:

> *It helps to imagine under what conditions a man would be swimming at, say, the same Reynolds number as his own sperm. Well you put him in a swimming pool that is full of molasses, and then you forbid him to move any part of his body faster than 1 cm/min. [59]*

Another dimensionless number of consequence is the Péclet number Pe. It expresses the ratio of advection to diffusion of an object in the flow and is expressed symbolically as $Pe = vL/D$ where v and L are characteristic velocities and length scales, and D is the diffusion coefficient of the object. In flows with Pe much greater than one, the rate of advection is much higher than the rate of diffusion and diffusive effects can be ignored. The Péclet number gives you a sense of whether diffusive motion is important for a particle in a fluid. In a flow with high Pe and low Re, which is the predominant condition for the work in this thesis, we can ignore diffusion and assume that particle motion strictly follows streamlines. The flows discussed in microfluidic devices often contain a complex mixture of particles and chemicals, each with a corresponding Péclet number. In general, micron-sized objects flowing through microfluidic channels with velocity of 10s of microns/s or greater will have a high Pe and particle diffusion can be ignored while small molecules will have low to intermediate Pe and advection and diffusion must both be considered together understand their motion in the flow.

1.2 Deterministic Lateral Displacement

1.2.1 Basic Principles

Deterministic lateral displacement (DLD) arrays are microfluidic structures for continuous-flow separation of particles by size [24]. The mechanism of separation is physical displacement by obstacles arrayed in the flow. Figure 1.1 is a schematic showing the relevant parameters and typical particle behavior. An array of posts of

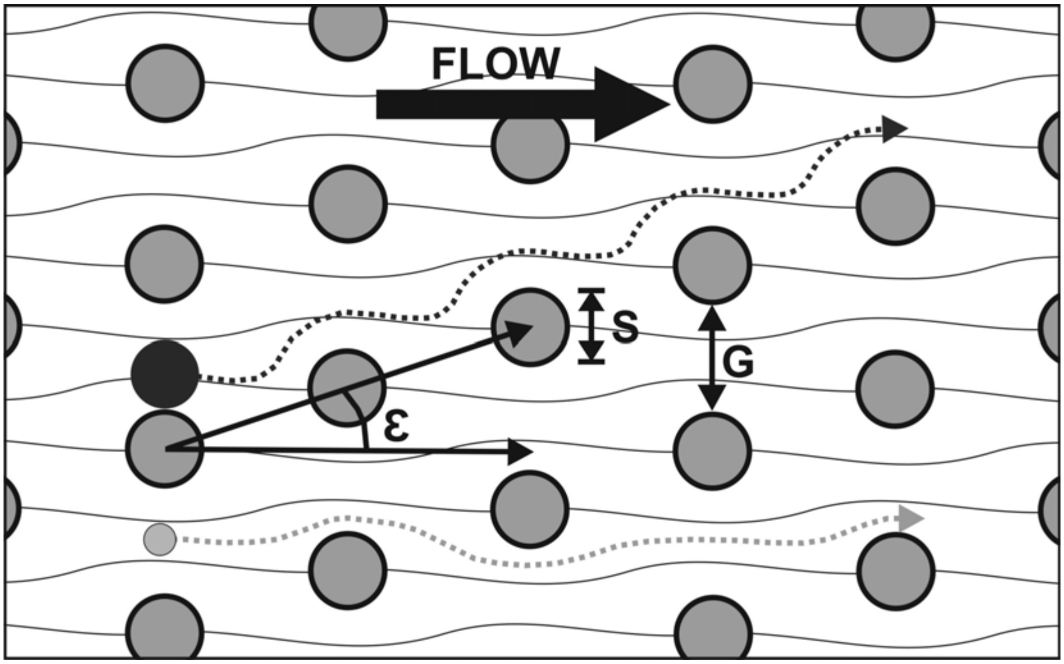

Figure 1.1: **Deterministic Lateral Displacement Array Schematic**. Posts with size S are arrayed in a channel with a gap G between posts such that one axis forms an angle ϵ with the average flow direction. Flow through gaps is divided into $1/\epsilon$ streams separated by stagnation streamlines that begin and end on posts and show how fluid divides around the posts. Small particles move through the array in a "zigzag" trajectory and follow the average flow direction. Large particles are displaced upward by the posts at each column and follow the array axis in a "bumping" trajectory.

side length S and gap G between posts are offset with respect to the direction of bulk fluid flow to produce one array axis tilted an angle ϵ with respect to the fluid flow, where ϵ is chosen such that $1/\epsilon$ is an integer. Typically, this is obtained by tilting a square lattice by the angle ϵ or using a parallelogram lattice as shown in Figure 1.1.

This structure works by asymmetric bifurcation of fluid streams around the posts: the fluid flowing through a gap splits around a post in the next column, with 1-ϵ of the fluid going through the next gap while the other ϵ of fluid goes around the other side of the next post. As a result, the fluid motion can be characterized by $1/\epsilon$ streams that cycle through positions in the gap, but travel straight (horizontally) on average. These streams are separated by stagnation streamlines that begin and end on posts and show how the fluid divides around a structure.

Particles in the flow exhibit one of two behaviors depending on their size relative to the stream next to the post as they move through a gap. Particles whose radii are smaller than the stream width, denoted by the light gray particle with dotted trajectory in Figure 1.1, will not be displaced by the post and will remain bound within one stream as they follow a “zigzag” trajectory that weaves through the posts in the array. Particles whose radii are larger than the stream width, denoted by the dark gray particle with dotted trajectory in Figure 1.1, cannot fit within the stream next to the post as they travel through a gap and will be “bumped” into the adjacent stream. The cyclical way that the streams move through the gaps then locks large particles into being “bumped” into an adjacent stream at every column and the particle will travel along the array tilt angle instead of with the fluid and other small particles.

This displacement can then be exploited to collect particles sorted by size downstream by splitting the flow into several channels that correspond to where particles of a given size are at the end of the array. Because this method relies only on particles following streamlines and displacement by obstacles, the separation effect is independent of flow speed as long as the flow remains laminar. Diffusion plays no role in the separation and degrades separation if particle diffuse across a stream boundary. As a result, the sharpness of the transition between “bumping” and “zigzag” displacement modes is enhanced by increasing the flow rate [24]. This phenomenon of has been employed in microfabricated post arrays for continuous-flow separation separation of particles over a large operating range (100 nm to 30 μm)[11, 53] for a variety of objects including polystyrene beads, DNA [24], bacteria [51], and human blood cells [11, 30, 33, 52], with a resolving power down to 10 nm [24].

The critical size for transition from small to large particle behavior can be predicted following a method proposed by Inglis *et al.*[29]. One divides the flow going through a gap between posts into $1/\epsilon$ streams of equal volume flux, and the critical

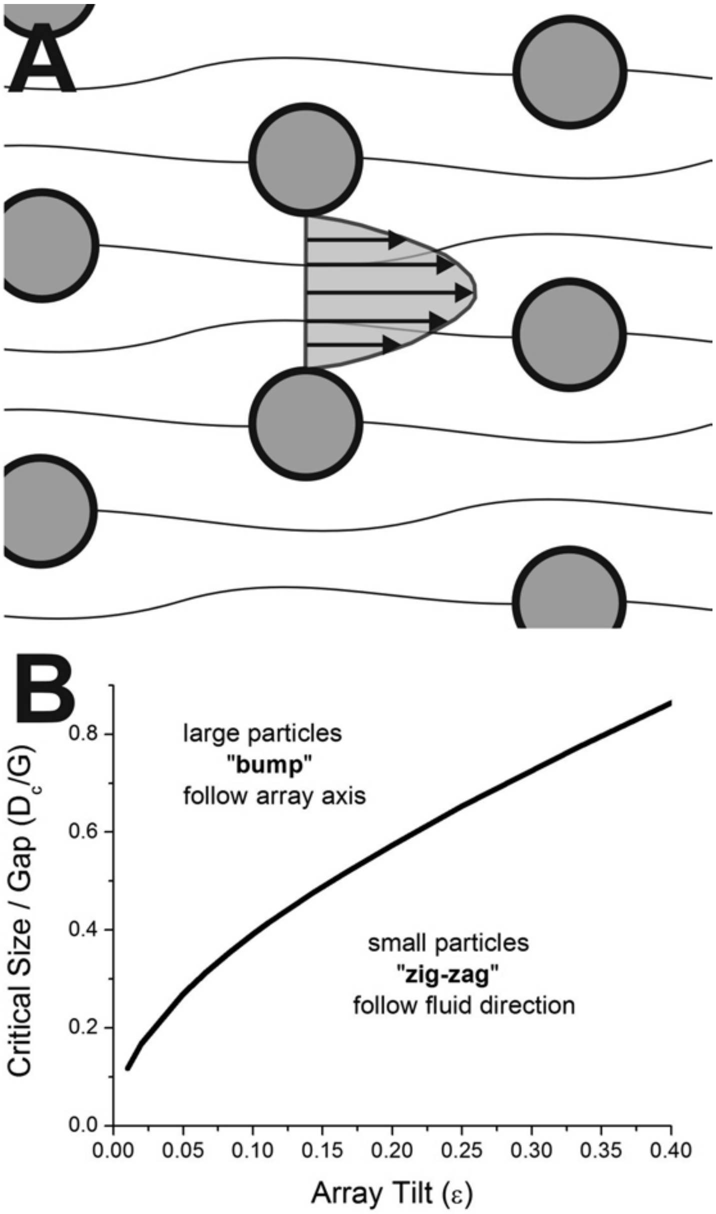

Figure 1.2: **Critical size in DLD arrays**. **A** Velocity profile across gap between posts can be estimated as a parabola akin to fully developed pipe flow. **B** Using this assumption, critical particle D_c sizes can be predicted (normalized to gap G) as a function of array tilt ϵ. Particles above the predicted size should be displaced by array and follow array axis, while particles below should follow the fluid.

particle radius is the width of the stream next to the post on the side of the post that displaces the particle. To find the width of the first stream adjacent to a post, we integrate over the velocity profile from the edge of the gap until the flux equals ϵ times the total flux through a gap. This can be represented symbolically as

$$\epsilon \int_0^G u(s)ds = \int_0^{\frac{D_c}{2}} u(s)ds \tag{1.1}$$

where D_c is the critical particle diameter and $u(s)$ is the total velocity as a function of position in the gap. Assuming a parabolic velocity profile like in fully developed pipe flow[77] for $u(s)$, which was shown to be a good approximation with numerical simulation [29], a prediction for the critical size D_c can be made for a given gap G and array tilt ϵ. This is shown in Figure 1.2B, where the critical size normalized to the gap is plotted as a function of array tilt. Particles whose size is above the predicted critical size should follow a “bumping” trajectory and move at an angle ϵ to the flow while those below will “zigzag” and follow the flow direction and these two different size ranges can be separated.

1.2.2 Device Fabrication

Devices are fabricated in silicon wafers using standard microfabrication techniques (with polydimethylsiloxane (PDMS) replica molding from a silicon master also available). Post arrays like those described in the previous section are defined on a wafer with fluidic inlet and outlet structures using standard photolithography and then etched using deep reactive ion etching (DRIE). A micrograph of the cross section of an array showing the vertical, high-aspect ratio posts is shown in Figure 1.3B. Once devices are etched, through wafer holes are made by sandblasting with silica microparticles or using a second DRIE etch. Devices are then sealed with a thin ~ 30 μm layer of cured PDMS fixed to a glass coverslip. A completed device with etched

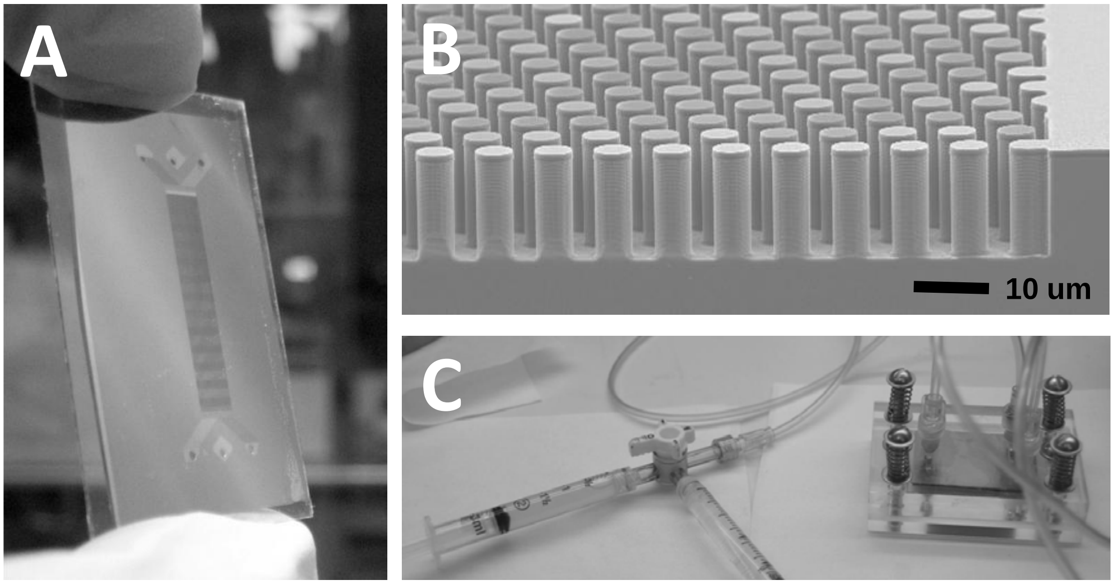

Figure 1.3: **Various steps in fabrication process**. **A** A completed device with array etched into silicon, sandblasted through holes, and PDMS-glass coverslide lid. **B** SEM micrograph of cross section of posts etched into silicon using DRIE. **C** Experimental apparatus with device mounted into acrylic manifold and connected to syringes which drive fluid through the device.

structures, sandblasted through holes and PDMS-glass cover slide is shown in Figure 1.3A. Devices are then mounted in an acrylic manifold like that shown in Figure 1.3C that mates device through holes to macroscopic fluid reservoirs to allow control of fluid flow through the chip by syringe pump or differential air pressure. The transparent cover slide allows optical inspection of devices during operation. Since particles in the device tend to be moving quickly across the field of view, a fluorescent marker is usually applied so that epifluorescent microscopy can be used. In cases where particle size is small ($\leq 1\ \mu m$), labeling is weak, or particle velocity is high ($\geq 5\ mm/s$), a laser source rastered across the field of view with a goniometer is recommended to distinguish the trajectories of single cells. In most other applications, illumination using a mercury lamp is sufficient.

1.2.3 Advanced Configurations

More complex particle separations and manipulations are possible by tiling arrays with different parameters on a single device. Array stages can be placed in series with little difficulty, so long as clogging is limited by ensuring the smallest gap in the series is larger than the largest particle intended to go through the device. As shown in Figure 1.4A, placing arrays with progressively increasing gaps in series creates a device that can separate multiple sizes of particles. In these “chirped” designs, the array tilt and lattice spacing is kept constant while the posts shrink in each section to increase the gap. The critical size is directly proportional to the gap G, so this has the effect of increasing the critical size in each section. This design was used to separate 0.80, 0.90, and 1.03 μm beads and this type of design has been used to analyze the size distributions of populations of cells in the blood as a diagnostic for exposure to bioweapons [30] and for platelet activation [33].

Complex particle trajectories are also possible by changing the array tilt in subsequent sections. This is shown in Figure 1.4B where a large particle is separated upward from a small particle in the first section and brought back together in the next section. This could be used to separate particles to measure the size distribution and then bring them back together for some downstream treatment. Finally, mirroring is possible to focus particles to a central region. Shown in Figure 1.4C, the array is mirrored about a horizontal line bisecting the array so that particles in the bottom section are directed upward while those in the top section are directed downward. Using this configuration, diffuse particles from a single inlet can be concentrated to a narrow band. These are examples of some of the basic elements that can be made by tiling arrays with different parameters in a single device. More complicated functions are possible by combining these elements in various ways [52].

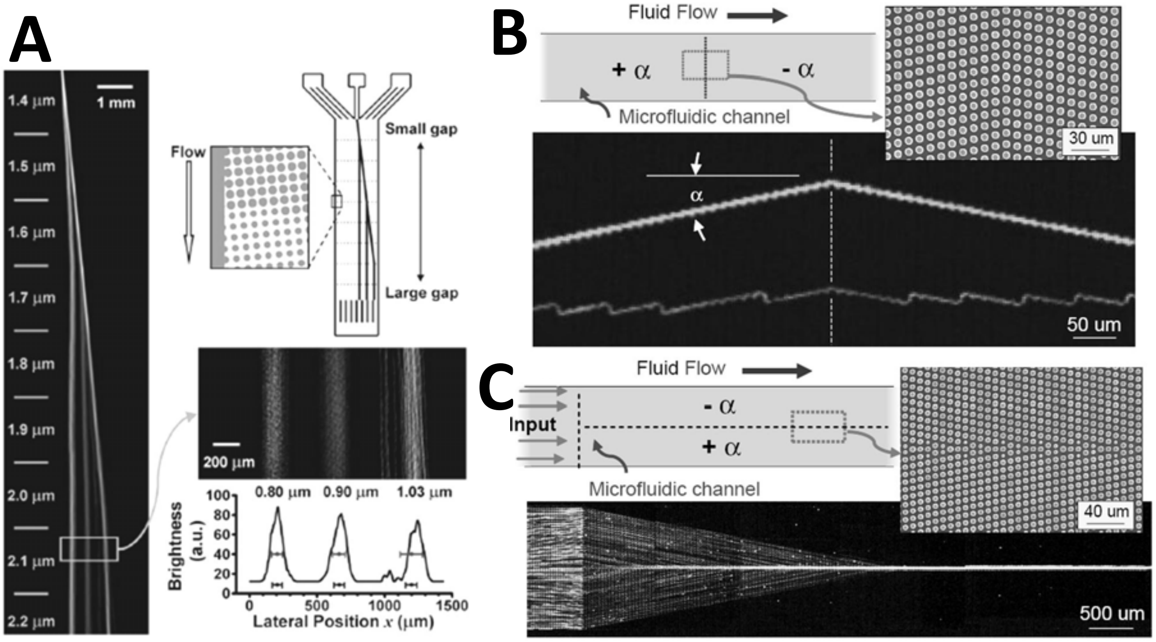

Figure 1.4: **Complex particle separation and manipulation devices A** A "chirped" device for separating particles into several size streams is created by placing arrays with different critical sizes in series. *Courtesy of Huang et al. [24].* **B** A device for separating and then bringing back together particles is created by changing the array tilt from directing particles upward to downward. **C** A particle focusing device is created by mirroring an array about a central horizontal line. *Courtesy of Morton et al. [52]*

1.3 Thesis Outline

Chapter 2 discusses a method for performing sequential on-chip chemical treatments using the DLD array. Biological or analytical preparations frequently require a series of chemical treatments each punctuated by a washing step to remove residual chemicals that may interfere with subsequent treatments. Washing is classically performed by centrifuging cells or particles into a pellet and removing the fluid and is accompanied by a reduction in yield as cells or particles not in the pellet are removed from the processed sample and discarded. This is overcome by using the DLD array to direct particles in the "bumping" trajectory across co-flowing reagent streams with a wash stream between streams to limit cross contamination between steps. Because the device is completely enclosed, there is no loss of cells as particles move through treatment streams. This technique is demonstrated with platelet labeling and washing and *E. Coli* lysis and chromosomal separation.

Chapter 3 discusses the development of a deterministic microfluidic ratchet. Numerous schemes for separating particles using Brownian motion in a ratchet have been demonstrated, but the throughput of these devices cannot be scaled up because the required diffusion is slow, and the weak dependence of diffusion constant on particle size limits resolution. In contrast to these methods, a ratchet that can deterministically separate particles based on size with high resolution and no limits on process throughput is constructed by using a DLD array with triangular posts.

Chapter 4 extends the work with triangular posts in DLD arrays to show significant performance enhancements in continuous flow operation when the triangle vertex is used as the displacement edge. The maximum particle size that a DLD array can accept without clogging is the gap between posts. This distance is on the same order as the critical size, requiring multiple separation stages if the input sample has a broad distribution of particle sizes. Furthermore, the relatively small gaps between the posts can lead to a large pressure drop across the device for a reasonable throughput compared to competing methods that rely on inertial effects and have much larger feature sizes. We show that using triangular posts allows the spacing between posts to be increased compared to circular posts while maintaining the same critical particle size. This results in lower likelihood of clogging and higher throughput for a given applied pressure.

Chapter 5 outlines the development of a highly parallelized DLD array architecture for processing macroscopic fluid volumes and show flow rates on the order of 10 mL/min with a single-layer device. Microfluidic devices have classically focused on processing or analyzing small volumes of fluid, preaching the virtues of less sample and reagent use while taking advantage of the the small channel dimensions to enhance analytical processes that rely on mixing. However, there are many cases, such as searching for rare cells or industrial processing, which require large volumes to be processed, preferably in a short a time as possible. We discuss efforts to produce DLD arrays capable of processing macroscopic fluid volumes. This is accomplished by designing arrays that are capable of being tiled on a single device layer and stacked vertically, allowing many devices to be run in parallel while minimizing external connections. Further increases in throughput are obtained by increasing the driving pressure and using a high-pressure manifold.

Chapter 6 discusses application of high throughput DLD arrays towards isolating viable circulating tumor cells from blood and concentrate algae from culture for biofuel production. Malignant cancer is thought to spread throughout the body to form secondary tumors via the circulatory system. Circulating tumor cells (CTCs) have been identified in the blood of patients with metastatic disease and can be used as a diagnostic for the severity of disease and to assess the efficacy of different treatment strategies. There is a critical need to isolate, propagate and characterize large numbers of viable circulating tumor cells to expand on understanding of the biology of metastasis, enable new methods for studying the emergence of drug resistance, and aid in the development personalized treatments. We demonstrate that high flow rate, continuous-flow capture of viable CTCs from blood is possible using DLD arrays designed to sort CTCs (which are larger than other cells) from blood.

Alternate, renewable energy sources are needed to offset consumption of petroleum-based fuels, minimize the effects of fluctuating oil prices, and meet the needs of increased energy security. Of the potential sources of biomass, microalgae stand out for their ability to produce oil at much higher densities per unit area of land used than crop sources. One current challenge in algael biofuel production is to reduce the cost so that it is competitive with petroleum-based fuels. A significant portion (20-40%) in the traditional processing cost comes from concentrating (dewatering) the algae from the dilute concentrations at which they are cultured to levels necessary for oil extraction. This step is classically performed by centrifugation, which is costly, energy intensive and must operate in a batch processing mode. We present DLD arrays that can continuously concentrate algae from culture and operated passively using the pressure head from a tank.

Chapter 7 summarizes our contributions and make suggestions for future work in this area.

1.4 Relation to Published Work

Chapter 2 is based on work published in *Lab on a Chip* [51]. Material presented in Chapter 3 excluding the discussion on anisotropic conduction was published in *Physical Review Letters*[45]. Chapter 4 contains work published in *Microfluidics and Nanofluidics* [44] and the additional discussion of trimodal separations. Chapters 5 and 6 are being prepared for publication. As it is the policy with most of these journals, we include in the bibliography the appropriate copyright notices whenever we reproduce material directly from published articles.

Chapter 2

On-chip Chemical Treatment

2.1 Introduction

Biological or analytical preparations frequently require a series of chemical treatments. In between each step, a washing step is necessary to remove residual chemicals from the previous step that may interfere with subsequent treatments. Washing is classically performed by centrifuging cells or particles into a pellet, removing the fluid and adding it width an equal volume of a clean solution. This can be performed multiple times to ensure a sufficient reduction in concentration of the background chemical. In cases where there are a limited number of input cells or reagents are expensive, this can be problematic because a reduction in yield will accompany each washing step as cells or particles not in the pellet are removed from the processed sample and discarded.

There is great potential for performing chemical treatments in microfluidic devices because reagent use can be minimized [65], independent streams of chemicals can be maintained with mixing only occuring by diffusion [36], and there will be no loss of cells or particles because the system is completely enclosed. Normally, in the laminar flow that dominates microfluidic devices, migration of objects like cells across streamlines is limited by their slow diffusion in water [36, 38, 76]. A number of techniques have been developed to enhance on-chip mixing of diffusive chemical species [63, 68, 72], but these techniques irreversibly mix the contents, contaminate downstream treatments, and have limited use for species that diffuse slowly, such as cells, beads, and large biomolecules.

In this chapter, we present a methodology for moving selected particles into and across functional streamlines in pressure-driven flow using a DLD array. By designing an array where target particles travel in the "bumping" trajectory, we are able to move objects across functional chemical streams. With this, complex biological objects can be lysed, labeled and analyzed on-chip without cross-contamination. This concept is demonstrated by showing immunofluorescent labeling of platelets followed by washing and *E. Coli* cell lysis with simultaneous separation of bacterial chromosome from the cell contents. These important examples demonstrate the potential to implement complex treatment protocols for on-chip, continuous flow manipulation and analysis of cells, large bio-particles, and functional beads by arraying multiple treatment zones on the same chip [57, 65, 70, 78]. The chapter closes with a detailed analysis of reagent diffusion with adjacent, parallel streams of reagents and how this affects device design.

Work in this chapter was performed in collaboration with Keith Morton. He was responsible for platelet label and wash experiments while I performed *E. Coli* lysis and chromosomal separation experiments. Fabrication and development of key concepts were performed jointly.

2.2 Principle of Operation

Particle treatment is enabled by having one or several independent, co-flowing treatment streams in a DLD array designed so that target particles follow the "bumping" trajectory and travel at an angle with respect to the direction of bulk flow. As shown

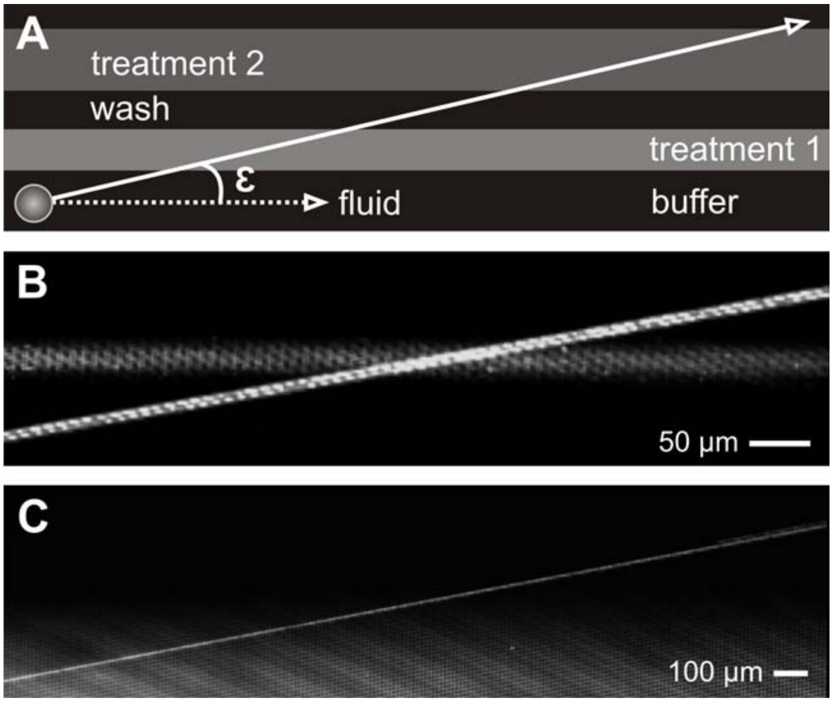

Figure 2.1: **On-chip sequential chemical treatment**. **A** A bump array can direct particles across co-flowing reagent treatment streams spatially isolated by washing streams without chemicals. **B** Epifluorescent time exposure of trajectory of 3.0 μm beads crossing over a stream of 0.5 μm beads. **C** Frame sum of a 3.0 μm fluorescent bead escaping from an area of high Rhodamine dye concentration into a coflowing region with no dye. The array **B** & **C** has 6 μm circular posts, 4 μm gap, $\epsilon = 1/5$ and 2.2 μm critical particle size.

in Figure 2.1A, as a particle is driven horizontally by the fluid flow, the array imparts a vertical displacement that directs it through several independent treatment streams. This method is relevant for the high Peclet number (no mixing between streams), low Reynolds number (laminar) flows that characterize many continuous-flow microfluidic devices [1]. We first demonstrate the capabilities of this technique with fluorescent beads and dye before moving on to on-chip cell treatments.

To illustrate the capabilities of this technique, we use the array to direct beads through streams of smaller beads and dye. Figure 2.1B shows a time exposure of 3.0 μm fluorescent beads crossing a stream of 0.5 μm fluorescent beads. The array in these experiments has 6 μm circular posts, 4 μm gap, $\epsilon = 1/5$ and 2.2 μm critical particle size. The larger beads travel along the array angle ϵ in the bumping mode while the smaller beads follow the overall fluid flow and can be used as a streamline trace. Despite similar and small diffusion constants relative to water ($D_{3.0\mu m} \sim 0.1\, \mu m^2/s, D_{0.5\mu m} \sim 0.9\, \mu m^2/s$) the larger particle enters, is immersed in, and then quickly exits the particle stream. The residence time of a bumping particle in a reagent stream can be increased by increasing the width of stream at the input or changing the array parameters so that the particle drops below the critical particle size. It will then stay in the stream until the array is changed back so that the particle is above the critical particle size. Alternatively, the residence time can be decreased by reducing the width of the stream at the input or increasing the flow speed.

The more common case for cell treatments will be moving a micron-scale particle across a nano-scale chemical agent with much higher diffusion constants than the target particle. In this case, it is important that cross contamination between reagents be reduced by washing a particle of all previous treatments before entering the next reagent stream. An example of on-chip washing from diffusive species is shown in Figure 2.1C. This figure shows the trajectory of a 3.0 μm bead escaping from a region with high concentration of Rhodamine 6G dye (Exciton) into a co-flowing region of no dye. In the 8.0 s that it takes the bead to traverse the 2.5 mm wide panel, it is vertically displaced 500 μm by the post array. In the same time frame, the Rhodamine 6G stream ($D_{R6G} \sim 280\, \mu m^2/s$ [47]) is expected to broaden ($\Delta y = \sqrt{Dt}$) by 65 μm and it is clear from the figure that the bead has been transported from a region of high dye concentration to a region of low dye concentration. (It is possible that a particle carries some solvent from one stream with it after it passes through a stream into the next, but this effect is expected to be minor and has not yet been investigated.) Taken together the two examples in Figure 2.1 demonstrate that we can efficiently transport particles between distinct, non-mixing functional zones.

2.3 Platelet Label and Wash

Labeling and washing target cells are common protocols for many bio-analysis techniques where one wants to detect the presence and quantity of a target cell in a heterogeneous mixture. Here we demonstrate that blood platelet cells can be fluorescently labeled and then immediately washed on-chip. Venous, EDTA-anticoagulated blood (Oklahoma Blood Institute) was used as a source for platelets and lymphocyte white blood cells. The Ficoll-Paque (GE Healthcare) protocol was used to selecting lymphocytes and platelets from whole blood. Following the centrifuge step, the lymphocyte and platelet rich layer was pipetted out and resuspended in running buffer (AutoMACS, Miltenyi Biotech). The solution was centrifuged to pellet the lymphocytes and the supernatant, containing platelets, was removed and used for on-chip platelet labeling. 50 μL of suspended, unlabeled platelets were loaded into the lower input reservoir of a device like that shown in Figure 2.2A.

We use the array to direct unlabeled platelets through a stream of labeling dye and into a clean wash buffer with minimal fluorescence background. The array (10 μm circular posts, $G = 5\,\mu m$, $\epsilon = 1/10$, and 2.0 μm critical size) shown in Figure 2.2A is designed so that platelets travel in the bumping mode across a jet of Phycoerthryin (PE) conjugated CD-41 antigen (eBioscience) into a washing stream. PE-CD41 is a common platelet-specific fluorescent marker that binds to the exterior surface of the cells. Platelets maintain a single trajectory along the array axis and encounter three distinct regions: the running buffer, which is the platelet source; the immunofluorescent labeling jet; and the washing buffer. Unlabeled platelets enter the labeling jet, pick up surface label and then are washed of residual dye on exit. Even though the platelets are only in the labeling stream for a few seconds, Figure 2.2B shows labeled platelets are clearly visible exiting the labeling stream and moving into clean buffer. This label and wash treatment demonstrates the possibilities for on-chip cell treatment.

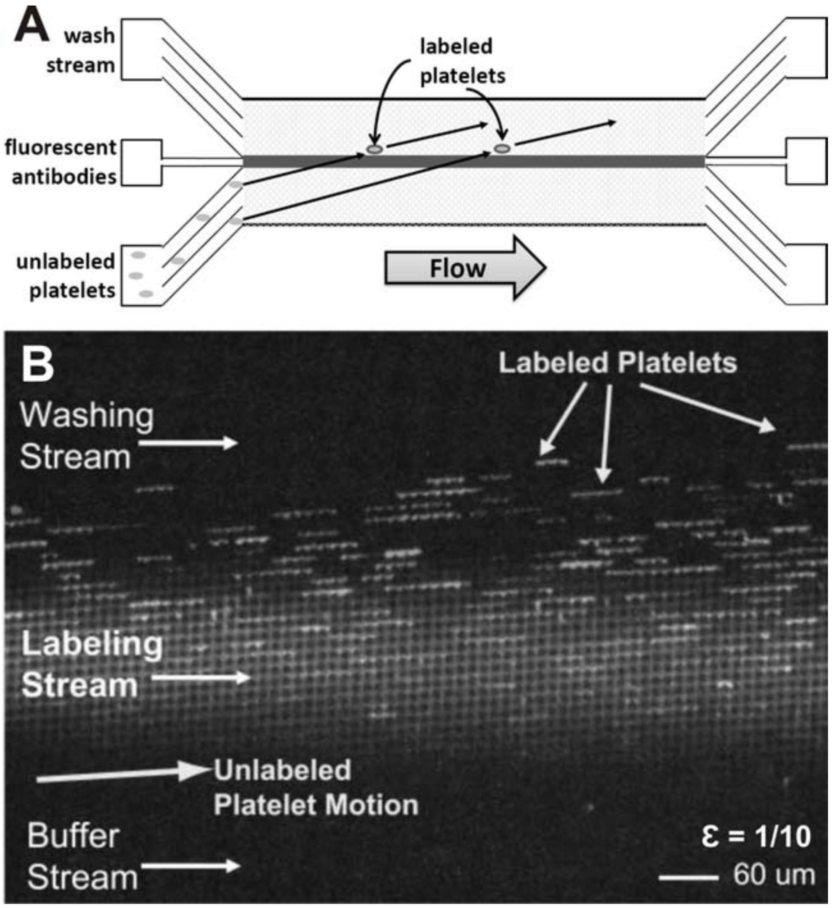

Figure 2.2: **Platelet Label and Wash**. **A** Layout for platelet label and wash experiment. Unlabeled cells enter in lower input, are directed through a jet of fluorescence conjugated antibody dye, and are washed and collected in the upper outlet. **B** Sum of 20 frames showing unlabeled platelets entering labeling jet (not visible), being stained (visible), and being removed to an area with no background fluorescence.

2.4 *E. Coli* Lysis and Chromosomal Separation

A more sophisticated example of the cell processing and separation capabilities using the DLD array can be seen in continuous flow lysis and chromosomal separation of *E. Coli* bacteria. In this case, two co-flowing streams of buffer each occupy one half of an array with critical particle size of 550 nm (2.8 μm circular posts, $G = 1.4\,\mu m$, $\epsilon = 1/10$, and 550 nm critical size). The liquid in the lower section is Tris-EDTA (TE) buffer with 1.1 M sucrose while the upper section is the same with 8% sodium dodecyl sulfate (SDS), a common lysis agent. Cells, following the tilt angle of the array, move from the lower region where they are osmotically stressed by the sucrose to the upper region where the SDS punctures the cell membrane (Figure 2.3A). We used *E. coli* with a green fluorescent protein (GFP) expressing plasmid to track cells and visualize lysis in real time. To ease on-chip lysis, *E. coli* were made into spheroplasts by removing cell wall with lysozyme[6, 58]. Figure 2.3B-E shows the lysis of a single cell in the lysis buffer. The two regions, one with lysing agent and one without, are demarcated by the fluorescent tracer stream. As the cell moves through the array, it is directed into the lysis solution along a bumping trajectory. Once in the lysis solution, the cellular membrane perforates and the cytoplasm empties out. Most of the cellular contents are smaller than the critical particle size so they change trajectory after lysis. This path can be visualized by the GFP since it is also below the critical particle size and will follow the same path as the rest of the subthreshold cellular contents.

While this result demonstrates the capabilities for using array to lyse cells on chip, we are also interested in the *E. Coli* chromosome's trajectory once it is released from the cell. To visualize and track the chromosomes after lysis, the nucleic acid stain SYTO 13 (Invitrogen) is applied to an identical population of the cells used in the previous step. Figure 2.4B-E shows the trajectory of the various E. Coli components after lysis. The small cellular contents, as visualized by the GFP, exit the bumping trajectory and follow the fluid flow after lysis like before. The chromosome, on the other hand, remains larger than the critical particle size and continues along the bumping trajectory of the original cell. A frame sum of the trajectory of a single cell shown in Figure 2.4E shows the separation clearly, with the angle between the GFP trace and the chromosome trace lines matching the array tilt. While both the GFP and SYTO13 dye appear green under 488 nm excitation, the absence of the fluorescent trail in Figure 2.3 and other cells without the nucleic acid stain strongly suggests that the fluorescent particle tracking along the original cell path in Figure 2.4E is the intact chromosome separating from the cellular debris. In this simple setup, there were only

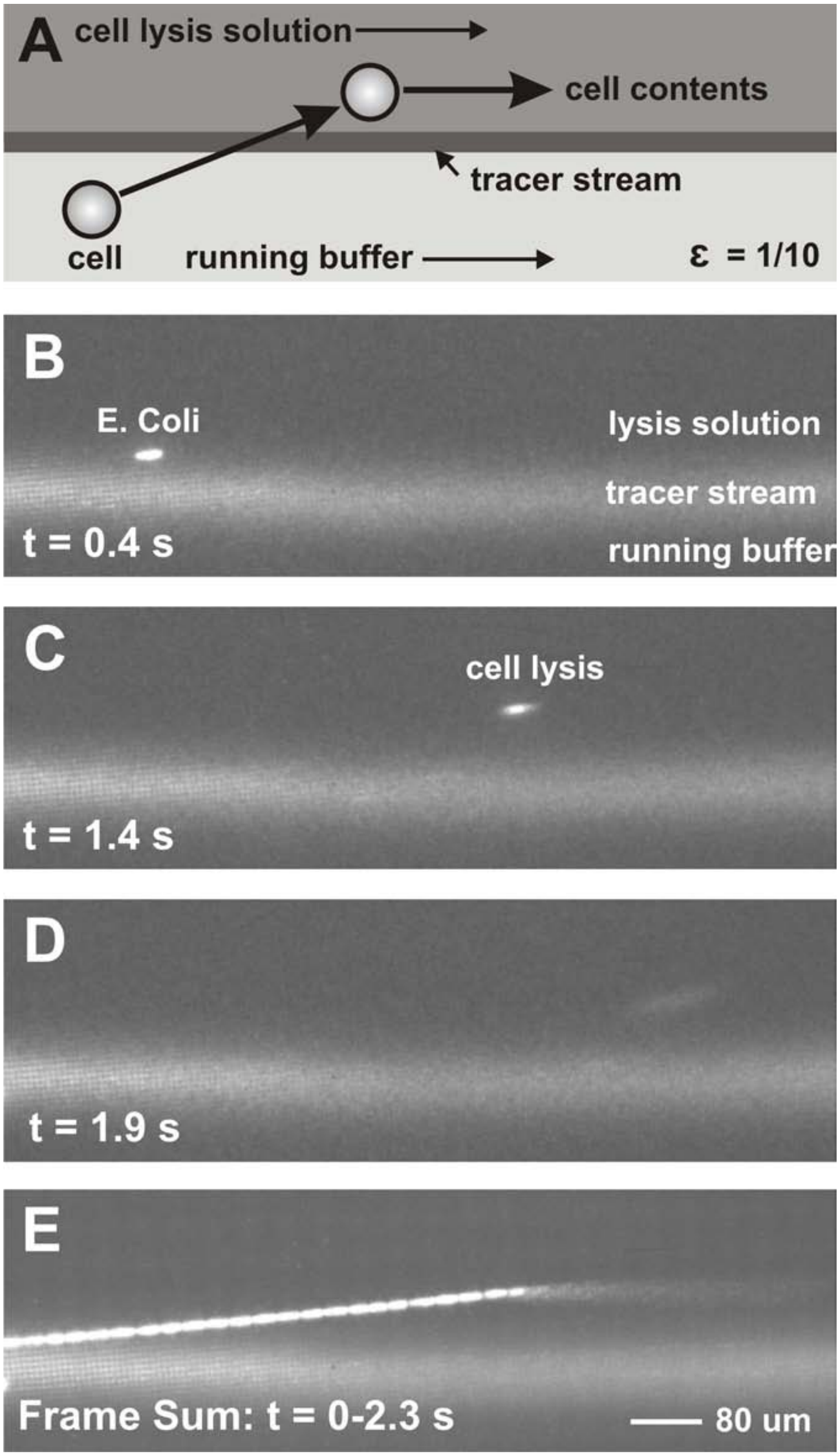

Figure 2.3: **Continous flow, on-chip cell lysis**. **A** Schematic of cell path from the lower half of the device containing running buffer into the upper half containing a cell lysing solution (8% SDS). **B-D**: time lapse trajectory of a single cell as it moves into the lysing solution(**B**), lyses (**C**), and its subthreshold contents begin traveling with the bulk flow (**D**). **E** shows the total cell trajectory over a 2.3 s exposure.

two streams, but future work in this direction could add a third wash stream where the chromosomes can be collected for analysis or transported to another functional region downstream.

2.5 Washing Analysis

We now describe some fundamental and practical considerations for device design. For the device to work properly, we want the vertical distance a “bumping” particle travels from the edge of a treatment stream in a given time frame to be much greater than the diffusive broadening in the same time. This is shown in Figure 2.5. As a particle moves a distance L through the array, it moves a lateral distance (ϵL) while the characteristic diffusion length of the reagent species from the stream diffuses into an adjacent zone ($\sqrt{Dt}$). The time for this transport is $t = L/v$ where v is the average fluid velocity. In analogy to the Peclet number Pe, we define a dimensionless figure of merit M, as the square of the ratio of the lateral displacement to diffusive broadening in the same time span.

$$M = \epsilon^2 L^2 / Dt = \epsilon^2 LV/D = \epsilon^2 Pe \tag{2.1}$$

This parameter tells us that if we want to reduce the background concentration of a treatment chemical with diffusion constant D, we can operate the device faster (increase V), make the device longer so it is further displaced from the chemicals (increase L), or increase the array tilt ϵ so the particle is displaced faster for a given velocity over a fixed length. As a design criteria, this ratio M should be much greater than 1 to ensure that the particle velocity outstrips diffusive motion from chemicals in the treatment stream. For the examples given, this M parameter is ~ 100 for the bead washing example, ~ 5 for the platelet label and wash and ~ 20 for the *E. Coli* lysis and chromosome separation. A more detailed analysis follows to give an estimate

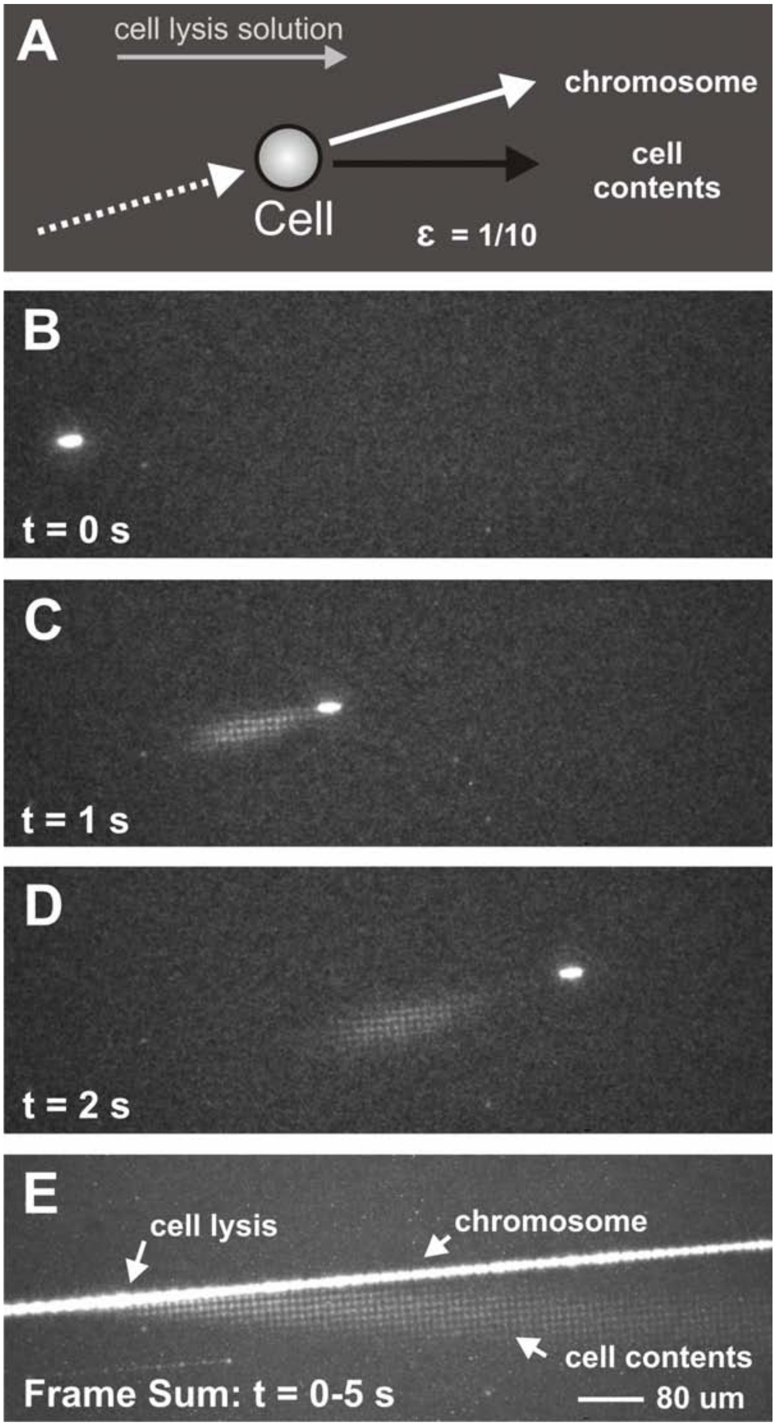

Figure 2.4: **On-chip lysis and chromosomal separation**. **A** Schematic showing paths taken by various cell components before and after lysis. The chromosome of the GFP-expressing *E. Coli* was fluorescently labeled to allow tracking of chromosome trajectory in addition to other cell components, which are visualized by GFP. **B-D**: time lapse trajectory of cell lysis. After cell lysis (**B**), the chromosome continues to track along the bumping trajectory while the rest of the cell contents move with the fluid flow. **E** shows the trajectory of the cell and cellular contents after lysis over a 5.0 s exposure.

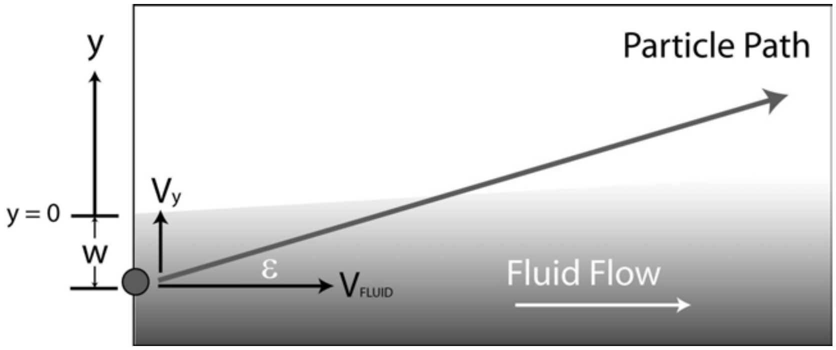

Figure 2.5: **Particle Washing** A particle starts a distance w from the outside edge of a treatment stream. As it moves horizontally with velocity v_{fluid}, the array imparts a vertical velocity $v_y = \epsilon\, v_{fluid}$. At the same time, molecules in the reagent stream diffuse upward at a rate $\sim \sqrt{Dt}$.

of how far a particle should be displaced to produce a concentration reduction by a specific amount, say 100 or 10,000 times. This will also assist in designing devices that have many treatment streams by giving an estimate for they should be placed to limit cross contamination.

As shown in Figure 2.5, assume initially a semi-infinite concentration profile, with concentration C_o for $y < 0$ and 0 for $y > 0$ and that the lateral diffusion of the reagent (in the y direction) is governed by the diffusion equation.

$$\frac{\delta C}{\delta t} = D \frac{\delta^2 C}{\delta x^2} \tag{2.2}$$

This ignores the broadening of the lower edge of the reagent stream to simplify the derivation and will produce a conservative estimate for the spacing because it effectively extends the lower edge of the stream to infinity, giving an unlimitied supply of reagent particles. This assumption also changes the meaning of the stream width w to a parameter that takes into account how long it takes the target particle to get to $y = 0$. If the particle initially starts at the bottom edge of the stream, then w is just the stream width. However, w can also take into account if the particle has some additional displacement from the bottom edge of the reagent stream, or, if the array parameters are changed so the particle follows the streamline mode to increase the

C/C_o	Ψ	C/C_o	Ψ
10^{-1}	0.91	10^{-5}	3.02
10^{-2}	1.65	10^{-6}	3.36
10^{-3}	2.19	10^{-7}	3.68
10^{-4}	2.63	10^{-8}	3.97

Table 2.1: $\Psi(y, t)$ for various degrees of washing

residence time, additional time it takes the particle to get to the edge of the stream. This extra distance/time will result in greater stream broadening and require the particle to be displaced further to achieve the same degree of washing.

The diffusion equation with the given initial conditions has the solution

$$\frac{C(y,t)}{C_o} = \frac{1}{2}(1 - ERF(\frac{y}{\sqrt{4Dt}})) \tag{2.3}$$

where ERF is the error function.

For variables y and t, there exist curves of constant concentration such that the argument of the error function equals a constant $\Psi = \frac{y}{\sqrt{4Dt}}$. Some Ψ for various concentration reductions are presented in Table 2.1.

We can establish a relationship between a particle's location and time by realizing that particles in the bumping mode are vertically displaced at a constant velocity equal to the horizontal fluid velocity v_{fluid} multiplied by the array tilt ϵ. Assuming the particle is initially a distance w from the edge of the stream at time $t = 0$ as shown in Figure 2.5, its position with respect to time is

$$y = \epsilon\, v_{fluid} t - w = v_y t - w \tag{2.4}$$

Solving this relationship for time t, substituting it into $\Psi = \frac{y}{\sqrt{4Dt}}$, performing some algebraic manipulation and dividing by w^2 to get a dimensionless form gives

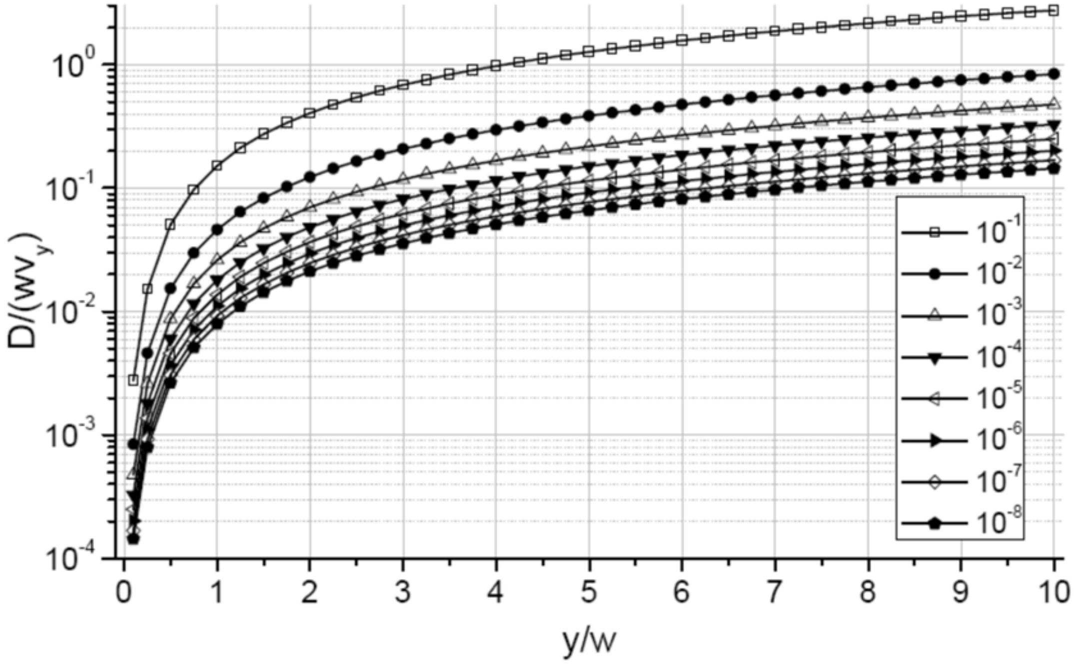

Figure 2.6: Curves that show how far a particle traveling through an array at velocity v_y must be displaced (y) from a chemical treatment stream of width w and diffusion constant D to achieve washing by a desired amount (Ψ).

$$\frac{y^2}{w^2} - 4\Psi^2 \frac{D}{wv_y}\frac{y}{w} - 4\Psi^2 \frac{D}{wv_y} = 0 \tag{2.5}$$

which provides a relationship for how far a particle must be displaced (y) from the treatment stream if it is traveling at given velocity (v_y) to achieve washing by a desired amount (Ψ) from a chemical with a given diffusion constant (D).

From this relationship, we can plot curves for each Ψ listed above. For parameters D, w, and v_y, the spacing y, normalized to w, can be found for any of the concentration reductions just by looking at the graph.

As an example, consider the bead washing demonstration given in Figure 2.1C and assume a width of 50 μm, diffusion constant 300 $\mu m^2/s$ (actual 280 $\mu m^2/s$), and overall fluid flow about 300 $\mu m/s$ (actual 312 $\mu m/s$). For an array tilt of 1/5, this gives a v_y of 60 $\mu m/s$. This gives a ratio of $\frac{D}{wv_y}$ of 1/10. Looking at the graph, we can see that if we were to displace a particle 100 μm away from the edge of the stream, the concentration of dye would decrease by more than 100 times. Displacing it 200 μm would decreases the dye concentration by more than 10,000 times.

Alternatively, we can solve for y/w from the equation 2.5 and (discarding the negative solution) substitute in for the appropriate parameters

$$\frac{y}{w} = 2[\frac{D\Psi^2}{wv_y} + \sqrt{\frac{D\Psi^2}{wv_y}(1 + \frac{D\Psi^2}{wv_y})}] \tag{2.6}$$

Using this approach, we get separations of 86 μm and 178 μm for 100 and 10000 times concentration reduction, respectively.

2.6 Summary

In summary, we presented a versatile tool for continuous-flow, on-chip biological processing. Using the DLD array, we are able to move particles across chemical streams having different reagent constituents, enabling sequential chemical operations to be performed on particles or cells. We have demonstrated this method for on-chip cell treatments such as cell handling, labeling and rinsing, and bacterial chromosomal extraction. We identified critical parameters for successful device design and discussed necessary conditions for separating treatment streams to limit cross-contamination. The washing capabilities of this method are particularly valuable because they allow many analytical or cell treatment procedures to be cascaded on a single chip while still effectively isolating their reagents from cross-contamination. Figure 2.7 is an example of these possibilities. It shows a second generation device demonstration where particles initially suspended in dye are washed as they enter the array, cross another stream of dye, and finally enter into another wash stream. This device comprises five coflowing streams and shows how easily these components can be integrated onto a single device.

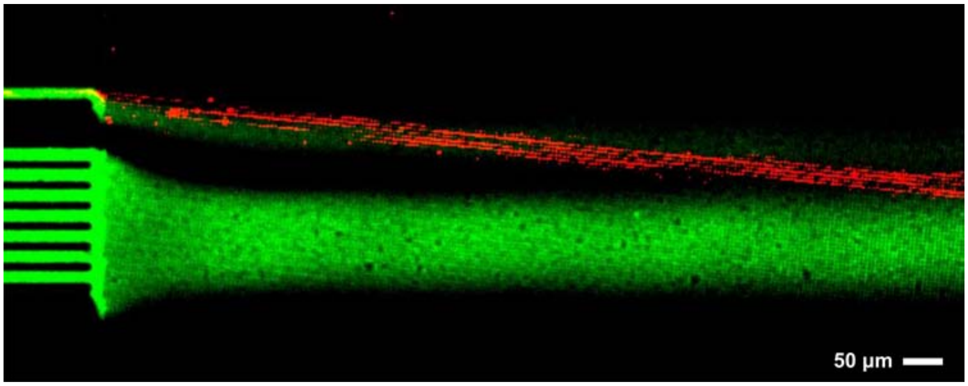

Figure 2.7: Demonstration of second generation cell treatment device with five co-flowing treatment streams. Fluorescent beads are initially in a solution with high concentration of dye. They are displaced downward by the array into a wash stream, into a second dye stream, and finally into a wash stream. Stream functionality from top to bottom are wash-dye-wash-dye-wash.

Chapter 3

Microfluidic Ratchet

3.1 Introduction

Numerous schemes for separating particles using Brownian motion in a ratchet have been demonstrated [8, 12, 49, 74]. These techniques rely on microstructured geometries that bias the motion of a thermally diffusive species. The speed of such devices cannot be scaled up because the required diffusion takes time, and the weak dependence of diffusion constant on particle size limits resolution. In constrast to these methods, a deterministic ratchet with a sharp dependence on particle size that relies only on steric repulsion constructed of a DLD array with triangular posts is presented in this chapter.

3.2 Basic Principles

Microfluidic devices, such as those used in “lab-on-a-chip” applications [16, 65, 66], typically operate at low Reynolds number. In this regime, the fluid flow through an arbitrary geometry can be considered to be time-invariant – reversing the applied pressure gradient that drives the fluid will reverse the flow field because inertial effects are negligible [17]. This allows the Navier-Stokes equation to be reduced to the equation governing creeping or Stokes flow:

$$\mu\nabla^2\vec{v} = -\nabla P \tag{3.1}$$

where μ is the viscosity of the fluid, v is the velocity field and P is the applied pressure.

Reversal of the sign of the pressure gradient $-\nabla P$ reverses the fluid velocity $\vec{v}$. Thus in the absence of diffusion and external forces particle motion is also time-reversible. However irreversible forces exist in our system in the form of steric repulsion between particles suspended in the fluid and posts that obstruct the fluid flow [21]. When a particle in the fluid runs into a post, it is displaced from its initial streamline to an adjacent streamline. As shown in Figure 3.1, if the fluid flow is reversed, it will not return to its original position, but rather travel back along its new streamline unless it is displaced by some other obstacle. This motion by particles across streamlines due to contact forces makes particle movement in the presence of obstacles irreversible in time and is critical to the effect we will describe in this chapter.

3.3 Experiment

A schematic of a bump array to implement a deterministic ratchet is shown in Figure 3.2. In previous uses for continuous-flow particle separation, the posts of the bump array have been round, but here we employ **triangular** posts. This array features right isosceles triangular posts with 6 μm leg length, a gap between posts of approximately 4 μm, and 1/10 array tilt. The array was fabricated in silicon by reactive-ion etching to a depth of approximately 10 μm and then sealed with a PDMS-coated glass slide. Fluid was driven by applied pressure of a hand-operated syringe pump

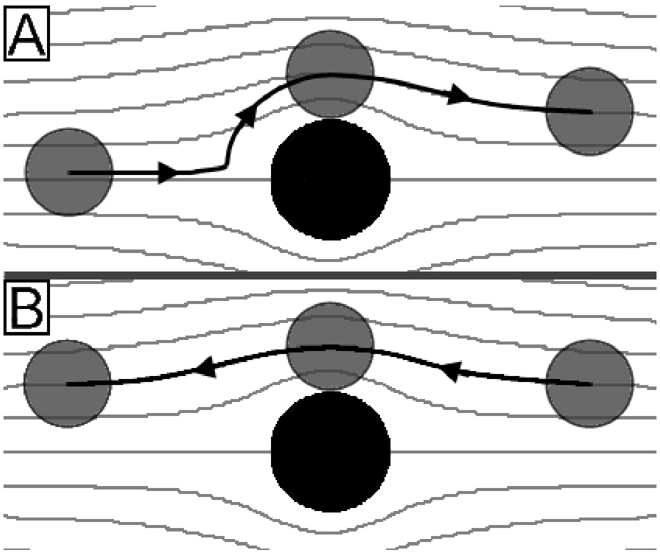

Figure 3.1: Irreversible particle motion results when a particle runs into an obstacle. **A** A particle moving left to right is displaced to a new streamline when it runs into a post. **B** When the flow is reversed, the particle follows its new streamline and returns to a different initial position.

and fluorescent bead trajectories were observed with epifluorescent microscopy. The sign of the pressure gradient was switched after the particle had traversed several periods of array to ensure that the observed behavior was characteristic of a particle of that size.

In addition to the two size-dependent particle trajectories classically observed in the DLD array, a third ratchet trajectory not seen in arrays with circular posts is observed in arrays with triangular posts under an **oscillating** flow. Under continuous flow operation in the bump array, small particles below a critical diameter follow the streamlines of the fluid and travel in the average fluid direction while particles larger than the critical diameter are displaced from one streamline to another by the posts and move at an angle ϵ with respect to the average fluid flow [24]. These particle paths are macroscopically reversible when the fluid flow direction is reversed, and the same behavior is seen the time-lapse images of the motion of small (1.1 μm) and large (3.1 μm) fluorescent polystyrene beads when the fluid flow direction was reversed multiple times as shown in Figure 3.3A&B. In devices with triangular posts, we found that

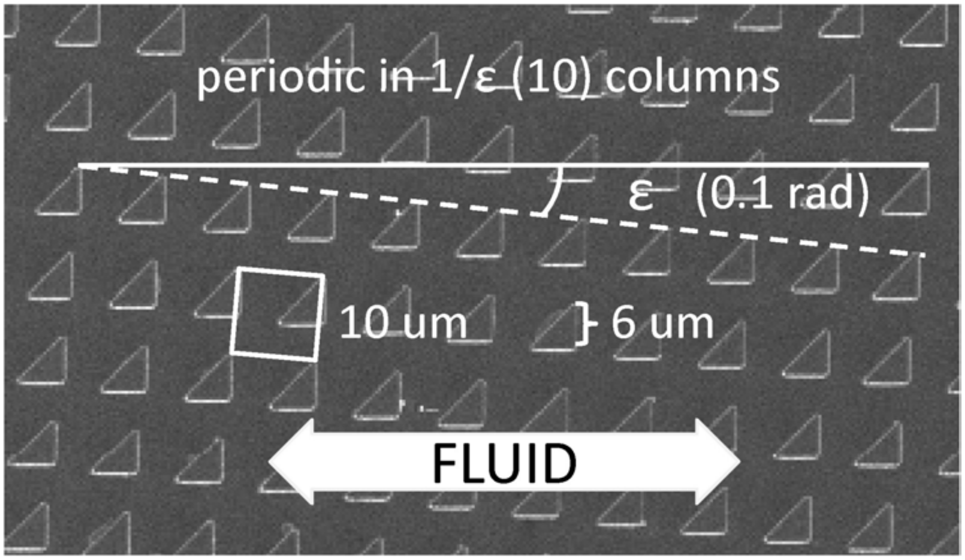

Figure 3.2: Micrograph of triangular post array used in experiments, with critical parameters schematically indicated. The right isosceles triangles are 6 μm on a side with 4 μm gap, with 1/10 tilt angle with respect to the horizontal fluid flow in a tilted square array. Fluid flow was forced to be horizontal by confining walls on the top and bottom of the device.

particles with an intermediate size (1.9 μm) did not retrace their trajectory when the fluid flow was reversed – rather, they followed the trajectory of large particles in one direction and approximately (to be explained further in Chapter 4, Section 4) that of small particles in the other (Figure 3.3C). When the fluid flow was reversed several times, the net motion of these particles was perpendicular to the axis of oscillatory fluid motion, leading the particles to be separated from their original surrounding plug of fluid without any net motion of the fluid. After many cycles of oscillation, these particles were concentrated along the upper edge of the device while "small" and "large" particles remained dispersed throughout the flow chamber.

3.4 Analysis

To understand this effect, consider the particle trajectories shown in Figure 3.4A showing a particle trajectories in an array with with $\epsilon = 1/3$ and circular posts for

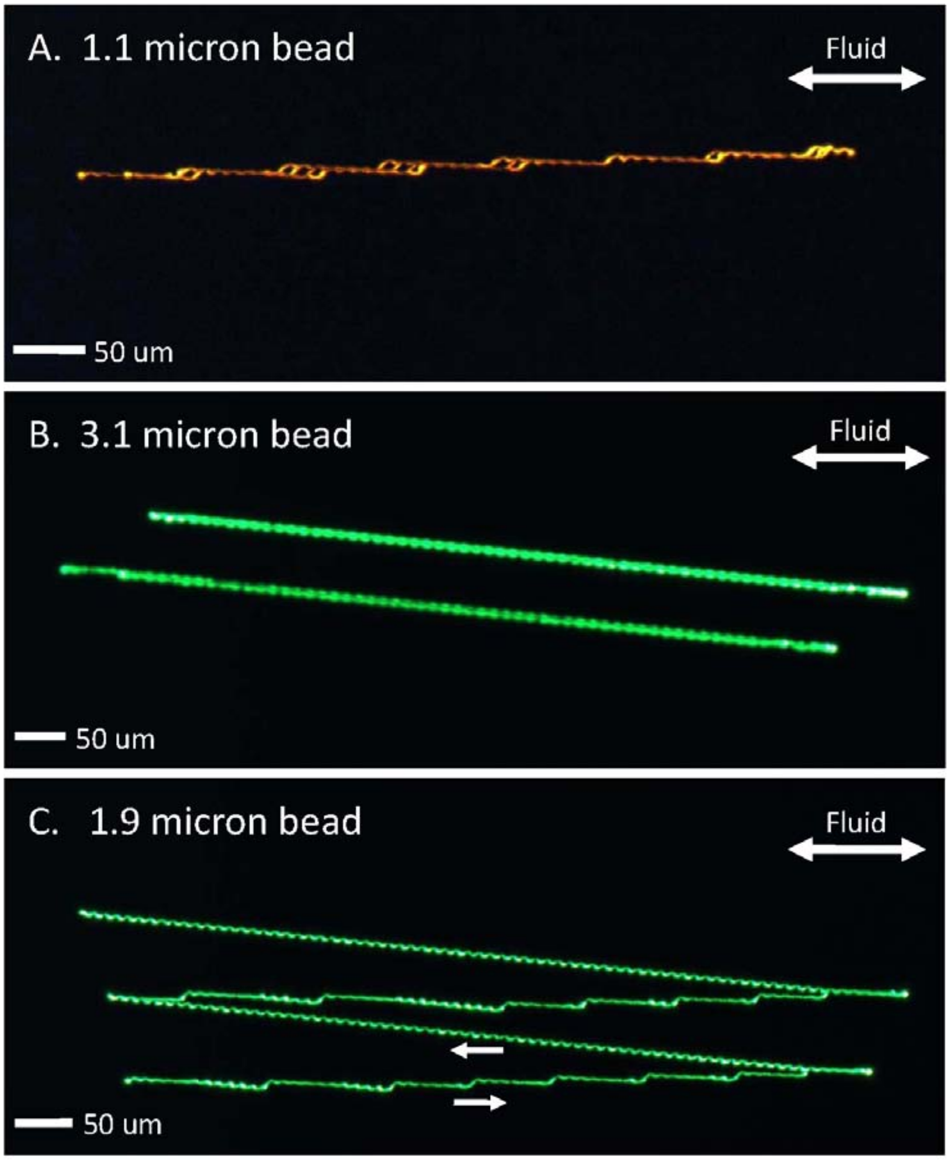

Figure 3.3: Trajectories of spherical polystyrene beads of three different sizes in the array shown in Figure 3.2 as the direction of fluid flow is cycled back and forth twice. Particle sizes are (**A**) 1.1 μm, (**B**) 3.1 μm, and (**C**) 1.9 μm. Particles in (**A**) & (**B**) retrace their paths when the direction of the fluid is switched while the trajectory in (**C**) varies with the direction of the fluid flow. In (**C**), small arrows indicate the direction of the fluid along the particle path.

simplicity. The lines connecting posts in the figure are stagnation streamlines lines that denote how the fluid will divide around posts and bound the three streams that travel through each gap. Particle trajectories are calculated in MATLAB using flow fields (v_x, v_y) extracted from COMSOL simulations of flow through geometries shown in Figure 3.4. Particles of a given size are propagated along streamlines until the particle comes within one radius of an obstacle. The particle is then shifted perpendicular to the surface of the obstacle a small distance ($\leq 50\,nm$) and allowed to continue forward, representing steric repulsion when a particle hits a post. This displacement and propagation scheme continues until the particle has traversed the field. Particle trajectories in the opposite direction are calculated by multiplying both components of the velocity field by -1 and repeating the same steps.

If a particle suspended in the fluid is small compared to the width W_c or W_{tri} of one of these streams, the posts will not affect it as it moves through the array and it will travel following the average fluid flow direction. If the flow direction is reversed, the fluid direction reverses because of time invariance and thus the particle returns along its original path. This is shown in Figure 3.4A.

If the particle radius is larger than that of the first stream next to the post in a gap, the particle will not be able to stay in that stream as it travels towards and then through the gap. Rather, it will be displaced into an adjacent stream. Note that the side of the obstacle that displaces the particle in Figure 3.4A depends on which direction it is moving - it is displaced by the lower edges of the obstacles when moving left to right and by the upper edges of obstacles when moving right to left. Thus the path of large particles is not precisely reversed on a microscopic scale, even though it appears to do so in Figure 3.3B. However, in an array with circular posts, this microscopic difference is of little practical consequence because the array is symmetric under spatial inversion ($\{x, y\} \rightarrow \{-x, -y\}$), which experimentally is the same as reversing the direction of fluid flow. Because of this symmetry, the width

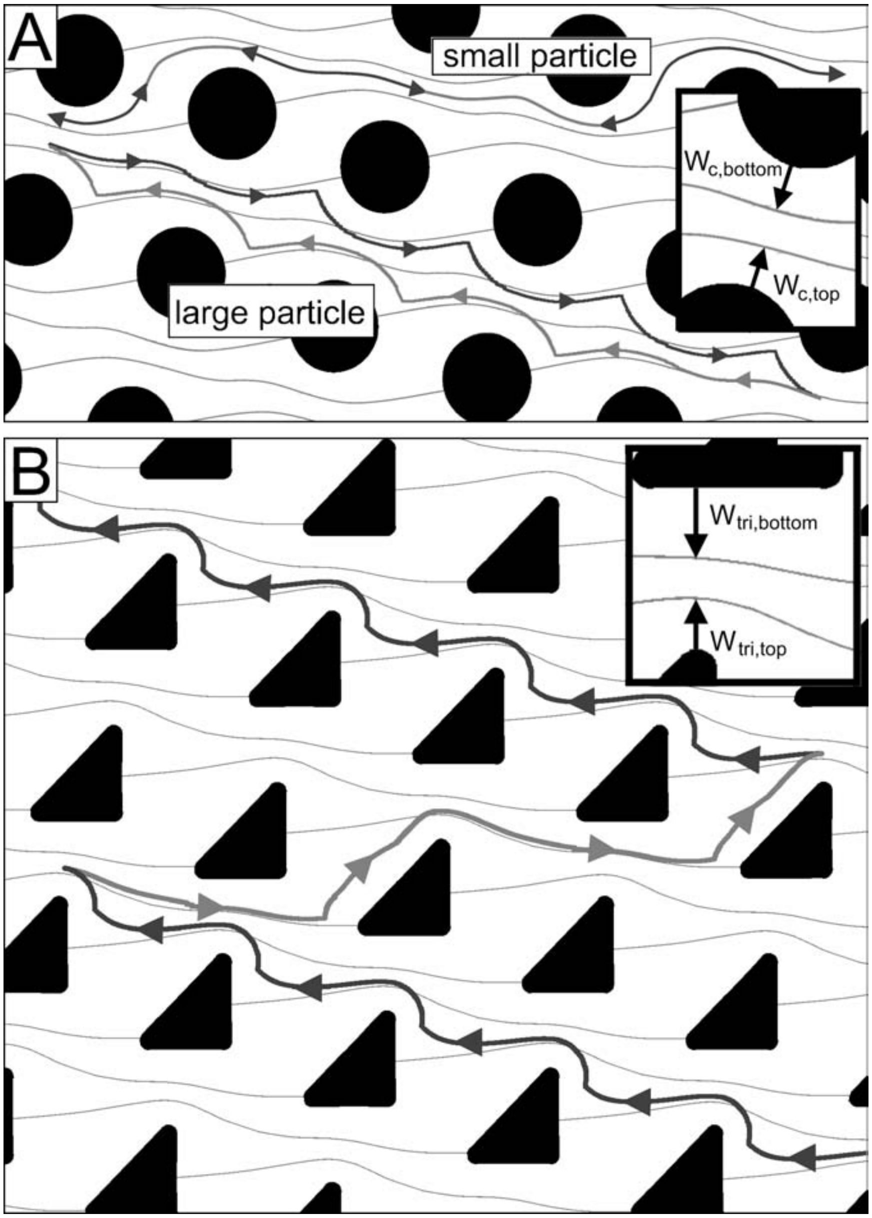

Figure 3.4: Simulated particle trajectories in DLD arrays with epsilon of 1/3 in oscillating flow for (**A**) round and (**B**) triangular posts as in Figure 3.2. Insets indicate the widths of the streams in the gap adjacent to the posts in both cases. **A** Paths of “small” and “large” particles moving both left to right and right to left, both of which macroscopically retrace their paths. **B** Path of a ratcheting particle in an array with triangular posts, where it is acts as a large particle traveling right to left but as a small particle when traveling right to left.

of the first stream above the posts is identical to that of the first stream below the posts so the critical particle size for bumping is the same in either direction.

An array with triangular posts breaks spatial inversion symmetry, which suggests that the critical particle size may be different depending on the flow direction. This is seen in the particle trajectory in Figure 3.4B, where the width of of the first stream above the triangular post (going past the upper vertex of the triangle) is narrower than that of the first streamline below the post (passing along the horizontal edge of the triangle). The particle size relative to this width determines whether a particle is displaced by the array - particles whose radii are greater than this width are displaced into the adjacent stream while smaller particles are not displaced by the post. Thus the critical particle size for particles moving left to right (displaced by the upper edges of the triangular posts) is smaller than that for particles moving right to left (bumping off the lower edges of the posts), explaining the behavior of the intermediate 1.9 μm particles in Figure 3.3C. They act like "small" particles (below the critical size) when moving left to right (when larger particles would bump off the flat edges of the triangle, and behave like "large" particles when moving right to left, displaced by the vertices which protrude from the upper edge of the obstacles into the fluid flow.

To further support this hypothesis, critical particle sizes were calculated from numerical simulations of the flow in the array structure used for the experiments of Figure 3.2, which has $\epsilon = 0.1$, and for a similar array with circular posts. The velocity profiles, normalized for width and peak velocity, extracted from these simulations were virtually independent of array tilts over a large range of array tilt (from 1/3 to 1/100). The calculated fluid velocity profile across gaps between posts are shown in Figure 3.5 for both cases. For round posts, the profile is symmetric about the center of the gap, so there should be no difference in critical particle size for fluid traveling towards the right or left. However, the velocity profile for the triangular

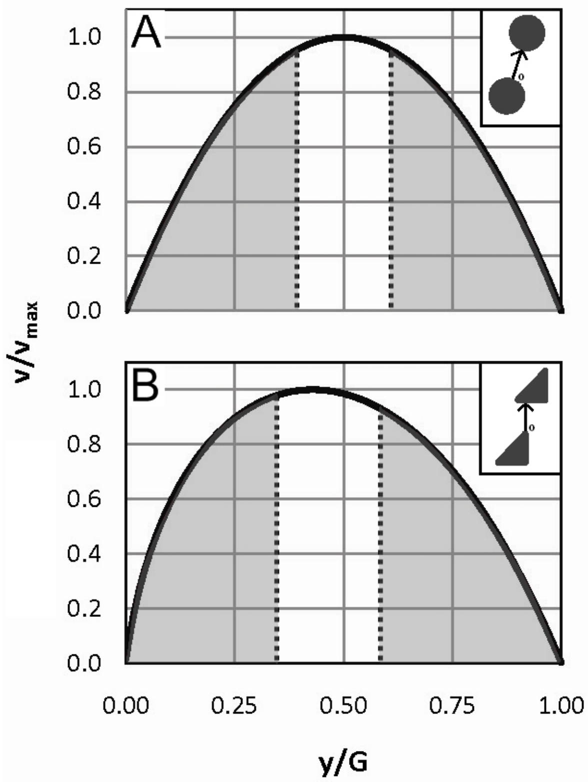

Figure 3.5: Normalized calculated velocity profile across gaps of bump arrays with (A) round and (B) triangular posts. Insets shows orientation of cross-sectional line. Shaded areas bound by dotted lines indicate fluid in characteristic streams closest to post on either side of the gap for $\epsilon = 1/3$.

post array is biased towards the sharp triangular vertex pointing up into the flow stream. Qualitatively, the critical size for a particle to be displaced should be smaller when a particle moves along the vertex of the triangle than it would be for the same particle moving along the flat edge of the triangle. Thus, it is possible to create DLD array with a direction-dependent critical size by using a post geometry that induces an asymmetry in the flow profile through a gap. If a particle falls in between these two critical sizes, it acts like a “small” particle when moving left to right and like a “large” particle when moving right to left. This leads to a ratcheting behavior, as is observed with the intermediate-sized bead in Figure 3.3C and shown schematically in Figure 3.4B. Large particles which are above both critical widths “bump” in both directions and are not ratcheted (Figs. 3.3B & 3.4A).

To quantify the difference in critical particle size between the vertex and the flat of the triangular posts and compare with experimental data, we employed the method used by Inglis *et al.* [29] to determine the critical particle size for an array with circular posts. One assumes $1/\epsilon$ streamlines of equal volume flux through a gap, and the critical particle radii are the widths of the streams nearest to the post on relevant side of the gap. As stated earlier, particles smaller than this size will not be displaced by the posts and travel along the axis of the fluid flow while the particles larger than this size will be displaced by the posts and travel along the array tilt axis. To find the width of the first streamline adjacent to a post, we integrate over the velocity profile from the either edge of the gap until the flux equals ϵ times the total flux through a gap. This can be represented symbolically as

$$\epsilon \int_0^G u(s)ds = \int_0^{\frac{D_v}{2}} u(s)ds = \int_{\frac{D_f}{2}}^G u(s)ds \tag{3.2}$$

where D_v is the critical particle diameter near the vertex, D_f is the critical particle diameter near the flat, and $u(s)$ is the total velocity as a function of position in the gap. For illustration, fluid in streams near the gap edges have been shaded in Figure3.5 for the case of $\epsilon = 1/3$. The width of these streams are 0.34 G (where G is the gap width) for the triangle vertex, 0.42 G for the triangle flat, and 0.39 G for both edges of the circular posts.

Using this method, one can predict what size particles will show ratcheting behavior in arrays with this geometry for different degrees of array tilt. Figure 3.6 shows the calculated critical particle diameter as a ratio of the gap for the vertex and flat of the triangle versus the array tilt angle. The observed data points of Figure 3.3 for $\epsilon = 1/10$ are plotted as crosses. There is excellent agreement between the observed modes of the three particle sizes and prediction. The 1.1 μm (0.24 G) bead is smaller than both critical particle sizes so it travels with the fluid in both directions and shows no net displacement when the fluid direction is cycled. The 3.1 (0.66 G) μm

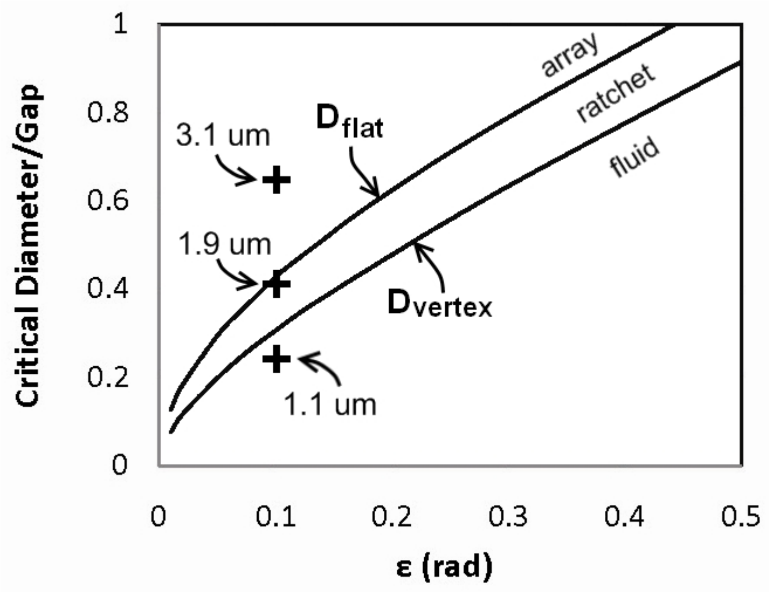

Figure 3.6: Predicted critical diameter as a ratio of gap for flat edge and triangle vertex versus array tilt angle. Central shaded region indicates range of particles that will exhibit ratcheting behavior under oscillatory flow. Experimental results from Figure 3.3 for $\epsilon = 1/10$ indicated by "+" for 3.1 um (0.66 G, bumps in both directions), 1.9 um (0.41 G, ratchet), and 1.1 um (0.24 G, not displaced in either direction) beads.

particle is bigger than both critical particle sizes so it is displaced along the array axis in both directions and shows no net displacement when the fluid direction is cycled. The 1.9 μm (0.41 G) particle is in between the two critical particle sizes so it travels with the fluid when it moves along the flat edge of the triangle and with the array axis when it moves along the vertex of the triangle.

3.5 Anisotropic Conduction

In the course of these experiments, an effect was observed at the interfaces between array sections that suggests fluid conducts anisotropically through arrays with right triangular posts. After the first array section where the data presented was taken, there is a second section with identical array parameters (gap, array tilt, post size), but the right triangular posts are rotated 270° with respect to the post orientation in the first section. The interface between these two arrays is shown in the micrograph in Figure 3.7A. At this interface, the the trajectories of beads and dye deviated substantially from the horizontal flow that is expected with bounding channel walls and a uniformly applied pressure gradient. Figure 3.7B shows the trajectories of 3.1 μm fluorescent particles, which followed the bumping trajectory in the first section. As the particles approached the interface, they transition from a bumping trajectory to a zigzag-like trajectory in the opposite direction of the array tilt. Instead of being directed downward by the array, they move upward, and as they approach the open area with large circular posts between the two sections, they move upward even faster - the number of columns of posts a particle traverses before zigging decreases from four to three as they get within approximately 200 μm of the interface. To ensure that this effect was a result of flow deviation and not a result of particle-post interactions, the flow field was observed using a fluorescent dye injected in lower half of device. Shown in Figure 3.7C the flow deviates upward from the centerline as it approaches the interface in the first section, and then downward towards the centerline in the second section. This suggest that the particle behavior could be explained by a local shift in the direction of fluid motion that changes the effective array tilt. The fluorescent particles, which were bumping far to the left of what is shown in the figure, see an array with a larger critical size as the fluid bending increases the effective array tilt. Conversely, in the second section, particles see an array with a smaller critical size as the fluid bends downward and reduces the effective array tilt. The deviation (250 μm) is on the same order to the expected displacement from the centerline for bumping particles (400 μm).

It is possible that this effect could be used to create a device that exposes particles to an array with a continuously varying array tilt and hence critical size, but it is undesirable for use with the standard DLD array because it breaks the assumption that the bulk flow direction is horizontal throughout the array. Developing a thorough

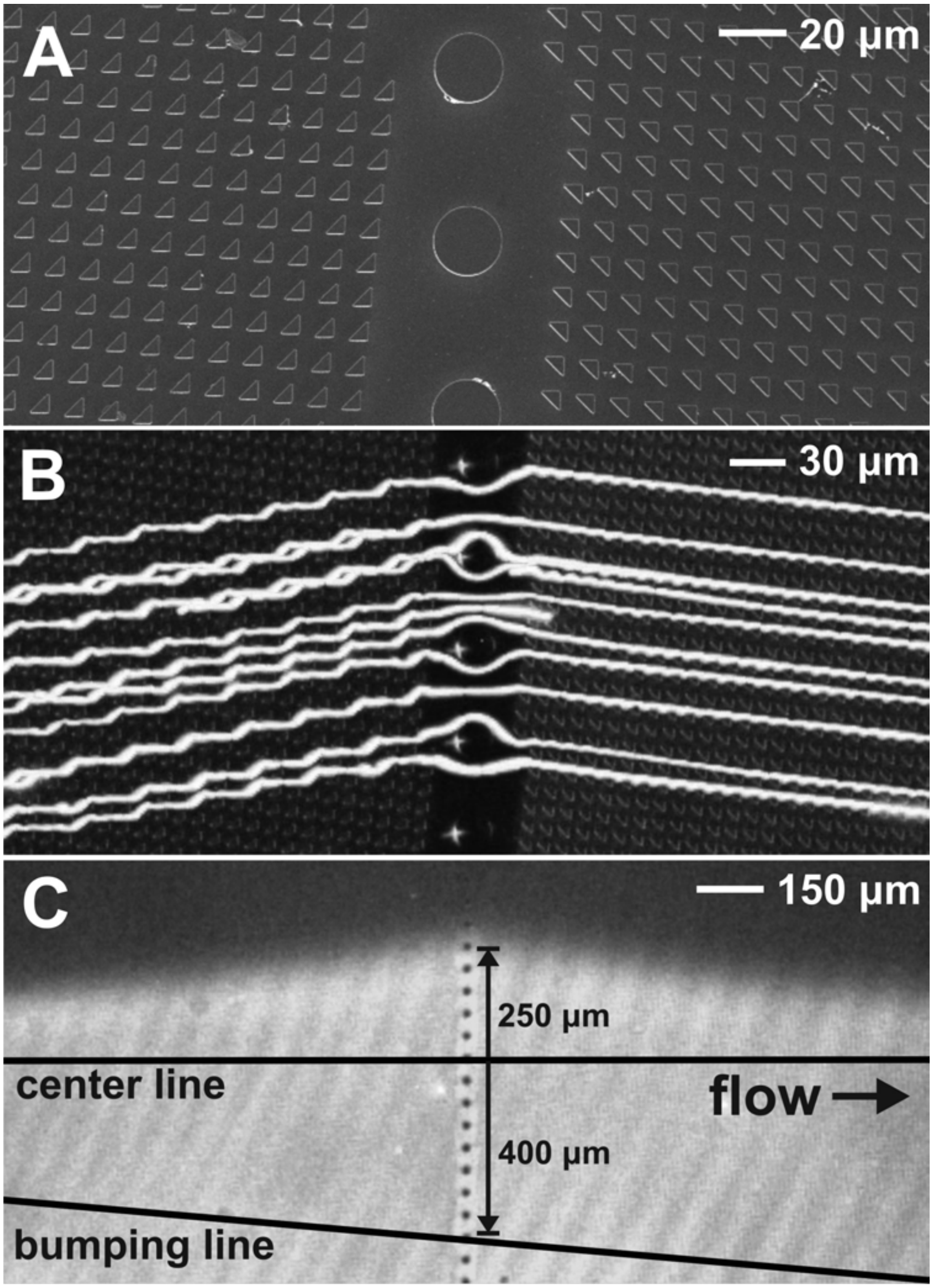

Figure 3.7: **Anisotropic conduction leads to flow irregularity at interfaces**. **A** Micrograph of interface between two triangular post DLD arrays where the posts in the second section have been rotated 270° with respect to the first section while all other array parameters are the same. **B** Trajectories of 3.1 μm fluorescent particles deviate from usual behavior (bumping) near interface. In first section, particles move in opposite direction of array tilt and then return to follow array tilt in second section. **C** Fluorescent dye injected in lower half of device shows flow deviates upward from the centerline as it approaches the interface in the first section, and then downward towards the centerline in the second section. The deviation (250 μm) is comparable to the expected displacement from the centerline for bumping particles (400 μm).

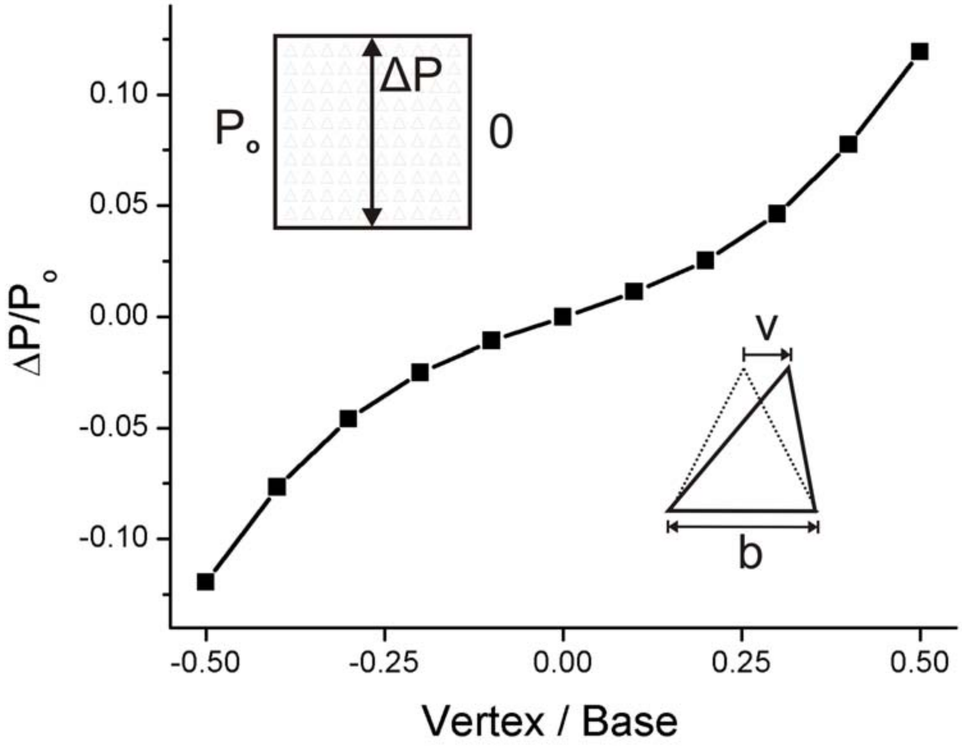

Figure 3.8: A 10x10 array of 10 μm triangular posts with 5 μm gaps and no array tilt was used to determine array anisotropy for triangular posts with varying vertex location. The left wall of the square was maintained at a constant pressure P_o while the right wall was held at zero pressure. The pressure gradient ΔP between the top and bottom walls was measured from a linear fit of the pressure across a vertical line at the middle of the array for triangular posts with a fixed base, but variable top vertex location.

understanding of the mechanism of this anisotropic fluid conduction effect is outside of the scope of this thesis, but we would like to find a post shape that preserves the ratcheting behavior demonstrated in this chapter while minimizing deviation from horizontal flow at interfaces between array sections and at the array inlet and outlet. This will allow arrays with triangular posts to be used when there are multiple inlet and outlet channels where one can collect ratcheted particles or, as will be shown in the next chapter, for continuous flow operation of DLD arrays with triangular posts.

The observed behavior in Figure 3.7 is suggestive of what one would see in an anisotropic conductor [55]. An anisotropic material with a horizontal pressure gradient and no flux along the top and bottom walls will develop an internal vertical pressure gradient to keep the fluid moving horizontally. At an open boundary with constant pressure, this internal pressure gradient must either build up or be released which likely causes the deviation from horizontal flow that we see. One apparent observation from Figure 3.7B&C is that the deviation follows the direction of the hypotenuse of triangle. This suggest that by changing the shape of the triangle, we may be able to reduce or eliminate this effect. To find the triangular shape that minimizes anisotropy, we performed a series of simulations to measure the vertical pressure gradient that builds up in a square array with triangular posts for various triangular posts. A 10x10 array of 10 μm triangular posts with 5 μm gaps and no array tilt was used. The left wall of the square was maintained at a constant pressure P_o while the right wall was held at zero pressure. The pressure gradient ΔP between the top and bottom walls was measured from a linear fit of the pressure across a vertical line at the middle of the array for triangular posts with a fixed base, but variable top vertex location. The pressure gradient normalized to the applied pressure $\Delta P/P_o$ as a function of the vertex position normalized to the base width is plotted in Figure 3.8. From the plot, we can see that right triangular posts ($\pm 0.5B$) are the most anisotropic, producing vertical pressure gradients in excess of 10% of the applied pressure gradient, and that the direction of the pressure gradient follows the slope of the longer triangle leg, as observed in Figure 3.7C. While these are interesting observations in themselves, the more salient point to take from the figure is that to minimize the anisotropy in an array with triangular posts, isosceles triangles with the vertex at the center of a base should be used. This shape will allow triangular posts to be used in DLD arrays while minimizing post shape-induced nonuniformities in the flow.

3.6 Summary

In this chapter, we presented a device for separating particles in an oscillating flow using a DLD array with triangular posts. This device functions as deterministic ratchet for particles whose size falls between the two critical sizes created by the skewed parabolic profile induced by posts with a sharp vertex on one side and a flat edge on the other, with no net displacement of the fluid itself. In an oscillating flow, particles in this range will be displaced orthogonal to the oscillating flow while those above and below will show no net displacement. The underlying mechanism of this ratchet is shown to be connected to irreversible particle-post interactions and the asymmetric fluid velocity distribution through the gap between the triangular posts. Analysis of the flow profiles following Iglis *et al.* [29] showed that the ratcheting size range for a given set of array parameters agrees with experimental observations. Experimental deviations from expected flow behavior at array boundaries were shown by numerical simulations to be minimized by using triangular posts whose upper vertex was centered with respect to the triangle base. Diffusion plays no role in this ratchet, and hence the device parameters presented here can be scaled up to high rates of flow, of clear importance in separation technologies. The particle velocities in this work were in the range of 250 μm/sec and the characteristic length was about 4 μm, corresponding to a Reynolds number of $\frac{1}{1000}$. Thus, the velocities could be increased by several orders of magnitude while remaining in the limit of low Reynolds number flow.

Chapter 4

Continuous Flow Improvements with Triangular Posts

4.1 Introduction

A key step in many analytical and preparative techniques in medicine and biology is to separate cells, functionalized beads, or other particles from a solution which may contain other undesirable elements [46, 56, 60, 65, 79]. Deterministic lateral displacement, a size-based particle sorting method, has shown extremely high size selectivity, adaptability to sorting multiple particle sizes[24]. However, several limitations hinder the broader applicability of this technique. The sorting mechanism relies on particles being physically displaced by an array of posts, with the open space between posts on the same order as the critical sorting size. As a result, the maximum particle size that an array can accept without clogging is the size of the gap and multiple separation stages are needed if the input sample has a broad distribution of particle sizes [11]. Furthermore, the small gaps between the posts can lead to a large pressure drop across the device for a reasonable throughput compared to competing methods that rely on inertial effects and have much larger feature sizes [5, 14].

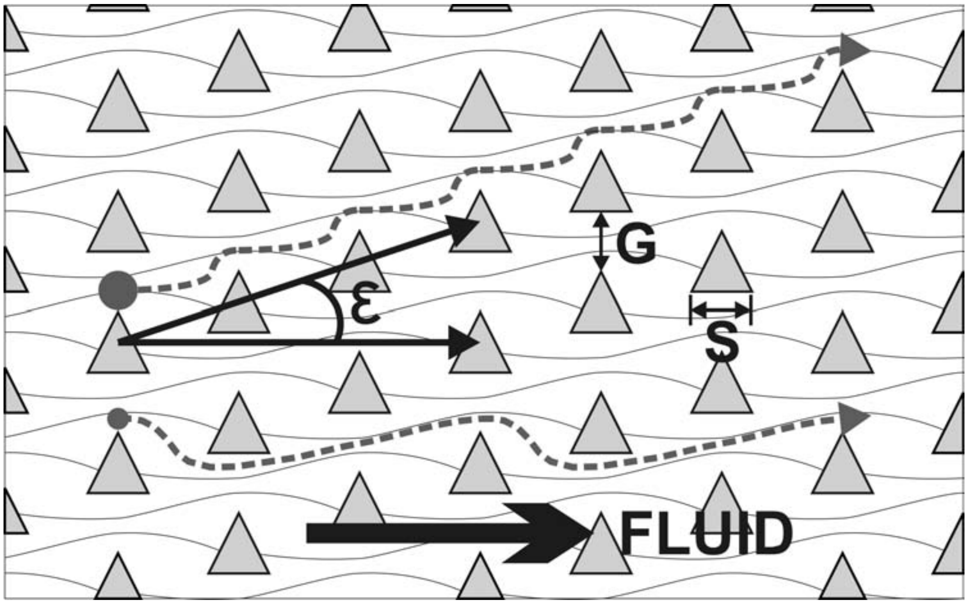

Figure 4.1: Deterministic lateral displacement array with triangular posts results in reduced clogging and lower hydrostatic pressure requirements by allowing for larger gaps for a given critical particle size. Posts are oriented so that large particles are displaced by the triangle vertex.

In the previous chapter, we discussed how changing the post shape can result in two distinct critical particle sizes by changing the shape of the flow profile through the gap. By changing the posts from the usual circular to triangular shape, an asymmetry is created in the flow profile through the gap that shifts fluid flux towards the triangle vertex. For example, as the particles in Figure 4.1 move left to right, they will be displaced by the vertex of the triangle and the critical size will be the stream width just above the vertex. This reduction is central to the improvements that will be discussed in this chapter, where we discuss additional improvements in continuous flow particle separation enabled by changing the post shape. In addition to experimental work confirming that triangular posts result in a reduced critical particle size compared to DLD arrays with circular posts, we will show that this post shape results in reduced clogging and lower hydrostatic pressure requirements by allowing for larger gaps for a given critical particle size. We will then show a series of simulations exploring practical considerations, such as vertex rounding, post size and shape, that affect design choices for further applications.

4.2 Comparison with Circular Posts

For any practical tilt angle (ϵ between 1/5 and 1/100), the critical size in an array with triangular posts is substantially smaller than a similar array with circular posts, with the difference as large as 10% of the gap for the steeper tilt angles. Predicted critical particle sizes as a function of array tilt are plotted as solid and dashed lines for circular and triangular posts, respectively, in Figure 4.2A along with observed behavior (displaced or not displaced) of fluorescent beads of various sizes. Critical sizes normalized to the gap are also listed in Table 4.1. Fluorescent beads with diameters ranging from 1.9 to 3.8 μm were used to characterize the behavior of particles in arrays with 4.7 μm posts, 6.3 μm gaps and various tilt angles. Obstacles were placed in a larger channel 3.4 mm wide and 16.8 mm long that maintains the tilt angle between the array axis and direction of bulk flow. Equilateral triangle posts were used to minimize anisotropy following the discussion in the previous chapter. Fluid motion is driven by applied pressure of a hand-operated syringe. Between five and ten particles were observed at each size and tilt to determine characteristic behavior. Examples of these behaviors are shown in Figure 4.2B. The Reynolds number was $\sim 10^{-4}$ for L $\sim$ 1 μm, V $\sim$ 100 $\mu m/s$ and the Peclet number was $\sim$100 for D $\sim$ 1 $\mu m^2/s$ from the Einstein-Stokes relation for diffusion coefficient of a spherical particle so effects of flow velocity and particle diffusion should not affect these observations. Particles above the line should be displaced by the array while those below the line should not. The theoretical predictions seem to set a lower bound on the size of a particle that will be displaced in the array. Notice that no displaced particles are seen below the predicted line.

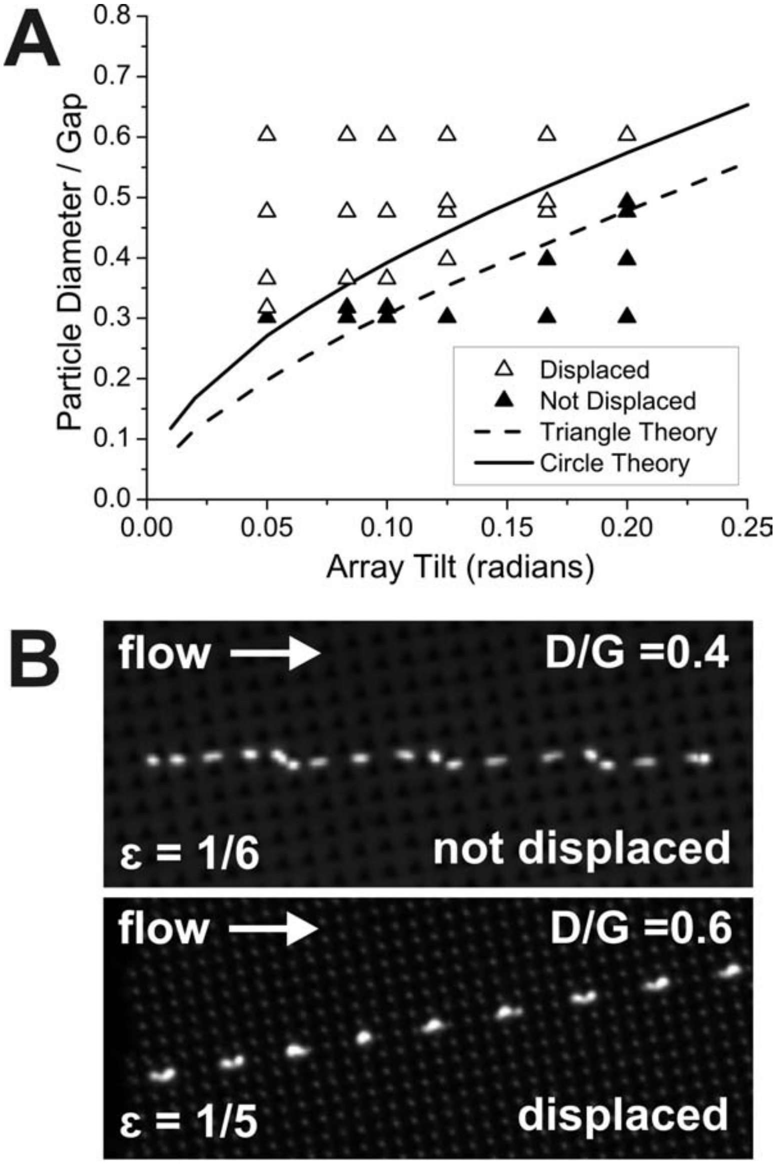

Figure 4.2: **A** Experimentally observed behavior of fluorescent beads compared to theoretical prediction of critical particle size for triangular posts with dimensions defined in Section 4.2. Particles of various sizes, normalized to the gap, are open if they were displaced by the array and closed if they were not displaced by the array. Theoretically predicted behavior is denoted by the dotted (triangular posts) and solid (circular posts) lines. Both theoretical critical size lines are plotted to emphasize the reduction enabled by triangular posts. **B** Example bead trajectories. A 2.5 μm bead is not displaced by an array with 6.3 μm gap and 1/6 tilt angle while a 3.8 μm bead is displaced by an array with 6.3 μm gap and 1/5 tilt angle.

Tilt Angle	D_C/G Triangle	D_C/G Circle
1/5	0.45	0.56
1/6	0.39	0.50
1/8	0.32	0.43
1/10	0.28	0.38
1/12	0.24	0.34
1/15	0.21	0.30
1/20	0.17	0.26
1/30	0.13	0.21
1/50	0.09	0.16
1/100	0.06	0.11

Table 4.1: Critical particle sizes normalized to gap height for arrays with triangular posts and circular posts for various array tilts.

There are three ways to take advantage of the reduced critical particle size with triangular posts. First, for the same gap and tilt, an array using triangular posts can separate smaller particles. Second, for the same critical particle size and gap, the tilt of the array can be increased, reducing the overall length of the array and providing a small increase in throughput for a given applied pressure. The third and most important is to allow an expansion of the gap while achieving the same critical particle size and array tilt. It is this last improvement that leads to both reduced array clogging and higher throughput.

Particles larger than the gap will clog the array. Biological samples often contain a broad range of particles with various sizes so multiple separation stages are sometimes necessary to ensure that the array continues to function [11]. Using triangular posts allows one to increase the size of the gap for a given critical particle size and reduce the chances that the array will clog. Figure 4.3 shows the theoretical ratio of triangular gap size G_T to the circular gap size G_C for fixed critical particle size as a function of array tilt. In the range of array tilts from 1/100 to 1/5, the ratio scales from 1.94 to 1.27.

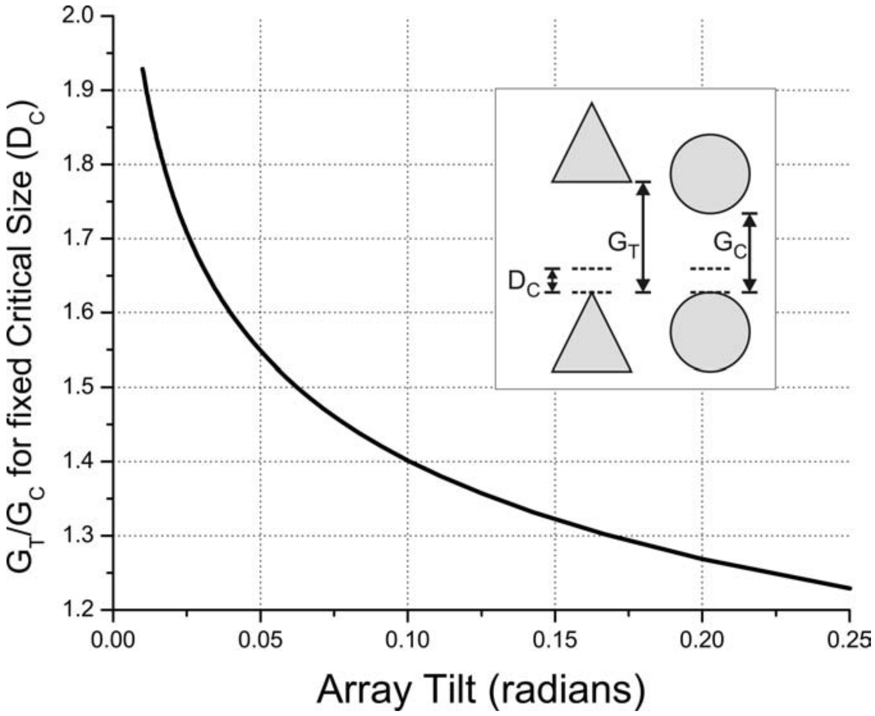

Figure 4.3: Ratio of gaps for triangular (GT) and circular (GC) post arrays for fixed critical particle size as a function of array tilt.

The larger gap enabled by triangular posts provides an increase in flow rate (or throughput) for a given applied pressure. This was confirmed experimentally by measuring average velocity of beads in two similar arrays. Two arrays were constructed with nearly identical characteristics for triangular and circular posts. They each had the same overall channel width (5 mm) and length (20 mm), etch depth (20 μm), tilt (1/10), and critical particle size of 3.2 μm. One array had circular posts with diameter 6 μm with a gap of 8.3 μm and the second had equilateral triangular posts arranged as in Figure 4.1 with side length 6 μm and gap 10.5 μm. The trajectories of 500 nm fluorescent beads were recorded with an EMCCD camera capturing video at 10 frames per second and then analyzed in MATLAB for various pressure gradients across the array. Pressure gradients were varied with a bleeder valve attached to a vacuum pump and measured with manometer attached in line with the pump. Small particles that would not be displaced by the array were chosen so they would sample each of the flow streams evenly and provide an accurate representation of the average fluid velocity [43]. Bead trajectories were isolated and an average velocity for each bead was determined by averaging its instantaneous velocity as it traversed several periods of the array. These values were then averaged together to produce an overall average bead velocity for a given pressure drop across the array. Between 4 and 19 beads with an average of 10.5 beads were tracked for each data point. The average particle velocities are plotted in Figure 4.4 as a function of pressure drop along with a weighted least squares fit for each array. Comparing the slopes of the two linear fits, it can be seen that particles in the array with triangular posts traveled $85 \pm 10\%$ faster on average than those in an array with circular posts. The large spread in this result can be partially attributed to particles traversing different regions in the vertical cross section of the device and also to the relatively high speed of the particles, which crossed the field of view of the microscope ($\sim$1 mm) after only a few frames of video. Nevertheless, this experiment shows that arrays with triangular posts can operate at significantly higher flow rates for a given pressure drop.

This result agrees with numerical simulations performed on similar array geometries with COMSOL that showed that the average velocity in the array with triangular posts was 82% faster than an array with circular posts for the same pressure gradient. The mechanism behind these findings can be understood qualitatively by drawing an analogy to Poiseuille flow between two parallel plates [77], where the average velocity for a fixed pressure gradient is proportional to the square of distance between plates. Experimentally, the flow rate does not scale exactly as the square of the gap because the confining structure is an array of posts instead of two parallel plates.

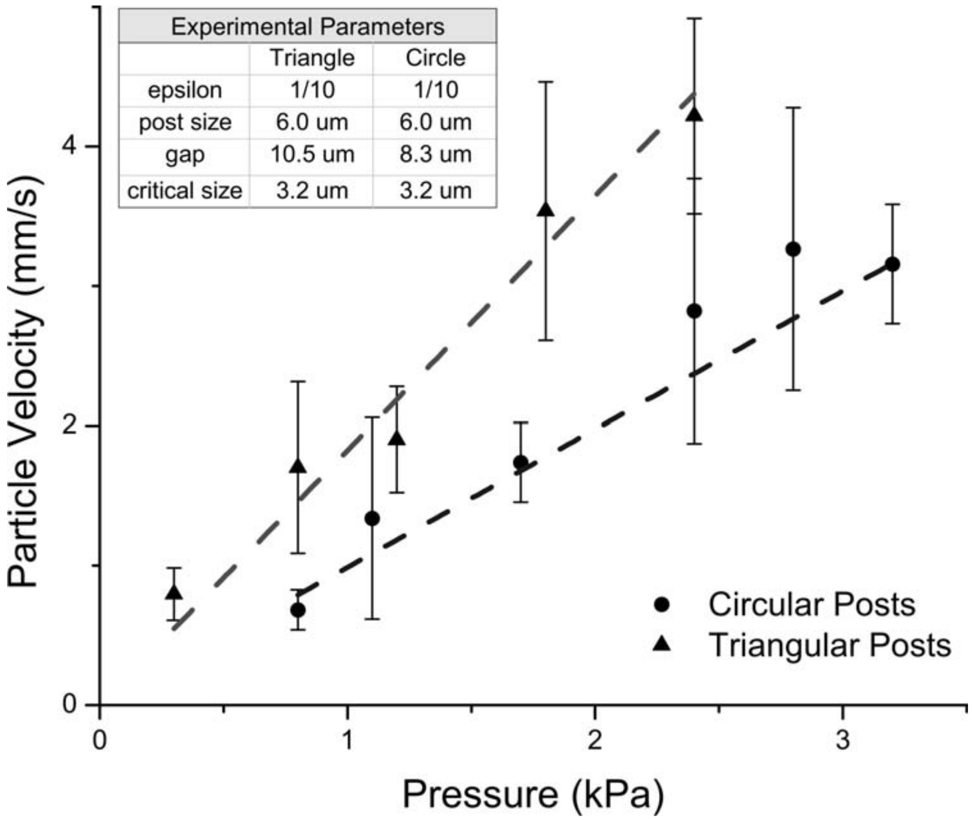

Experimental Parameters		
	Triangle	Circle
epsilon	1/10	1/10
post size	6.0 um	6.0 um
gap	10.5 um	8.3 um
critical size	3.2 um	3.2 um

Figure 4.4: Experimental throughput comparison of arrays with triangular and circular posts with same calculated critical particle size. The average velocities of beads that were not displaced by the array are plotted as a function of pressure drop along with a linear fit for each array. The average particle velocity for the same pressure gradient is 85% faster in an array with triangular posts than circular posts. Array dimensions are listed in the inset table.

4.3 Post Shape Exploration

Simulations were performed to explore the effect of post shape on array performance. Figure 4.5 shows the results of a series of simulations using regular polygons from three to eleven sides as the post shape. Arrays with 10 μm post altitude and 10 μm gaps between posts were simulated in COMSOL and flow profiles across the gap between were extracted for each array. Posts were oriented as shown in the figure inset to examine the difference between having sharp edges on both sides (even number of sides) versus a sharp edge and a flat edge (odd number of sides) on alternate sides of the gap. Critical particle sizes were calculated for tilt angle $\epsilon = 1/10$ for the top

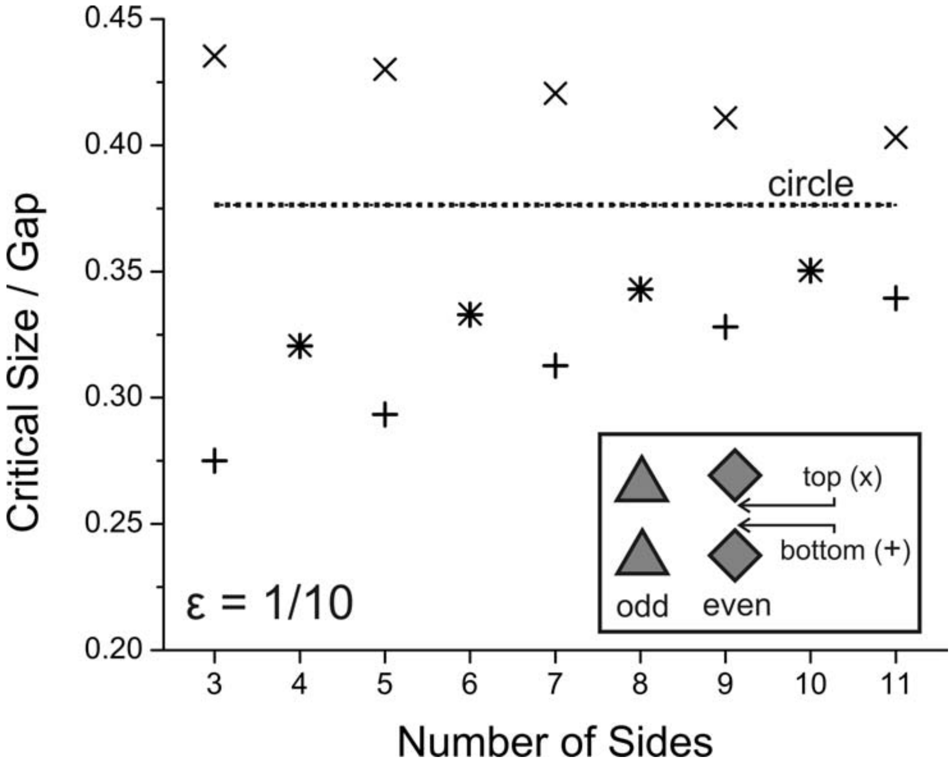

Figure 4.5: Critical particle size for arrays with regular polygon posts with varying number of sides. Arrays consist of posts with 10 μm altitude with 10 μm gap. Numerically simulated flow profiles across each gap were extracted from flow field simulations and critical particle size plotted for both top and bottom of post for array tilt $\epsilon = 1/10$ with critical particle size for circular posts plotted as a dotted line for reference.

and bottom of the gap and to show the effect of the asymmetric flow profile in posts with an odd number of sides. The critical particle size for circular posts has also been plotted as a dotted line for reference. The plot shows that a sharp vertex coupled with a flat edge act in unison to produce a smaller critical particle size. The figure shows that sharper vertices reduce the critical particle size. As the number of sides increases, the vertices become less sharp and the critical size increases, approaching that of circular posts. The effect of having a flat edge on the alternate side of the gap is also captured in the figure. In every instance, posts with an odd number of sides have a smaller critical particle size than the even numbered post with one less side, even though its vertices are not as sharp. While the critical size for even numbered

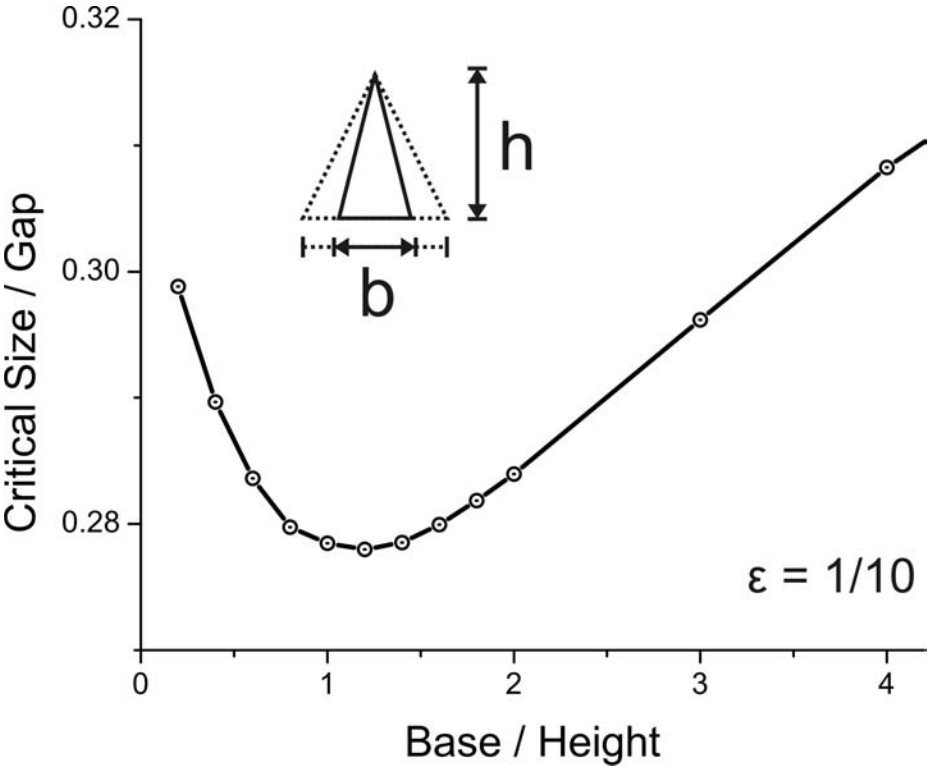

Figure 4.6: Critical particle size for arrays of triangular posts with varying base:height ratios. Flow profiles were numerically simulated across gaps between triangular posts in arrays with varying base width. Height of posts and gap between posts was fixed at 10 lm. Critical size for array tilt $\epsilon = 1/10$ calculated and plotted as a function of ratio of the post base width to height.

posts should be the same for the top and bottom of the gap because of symmetry, the differing geometry across the gap induces an asymmetry in the flow profile that shifts flow towards the bottom half of the gap. Thus, introducing a flat edge opposite a sharp vertex leads to an additional reduction in the critical size. It is when both of these characteristics are combined, as in the case of the equilateral triangle post, that the greatest reduction in critical particle size is seen.

The previous result might lead one to expect that further reduction of the critical particle size might be possible by using triangular posts with sharper vertices, but additional simulations show that there is a limit to the gains that can be achieved with this approach. Figure 4.6 shows the results of a series of simulations using triangular posts with varying base width. Arrays with 10 μm post height, 10 μm gaps between

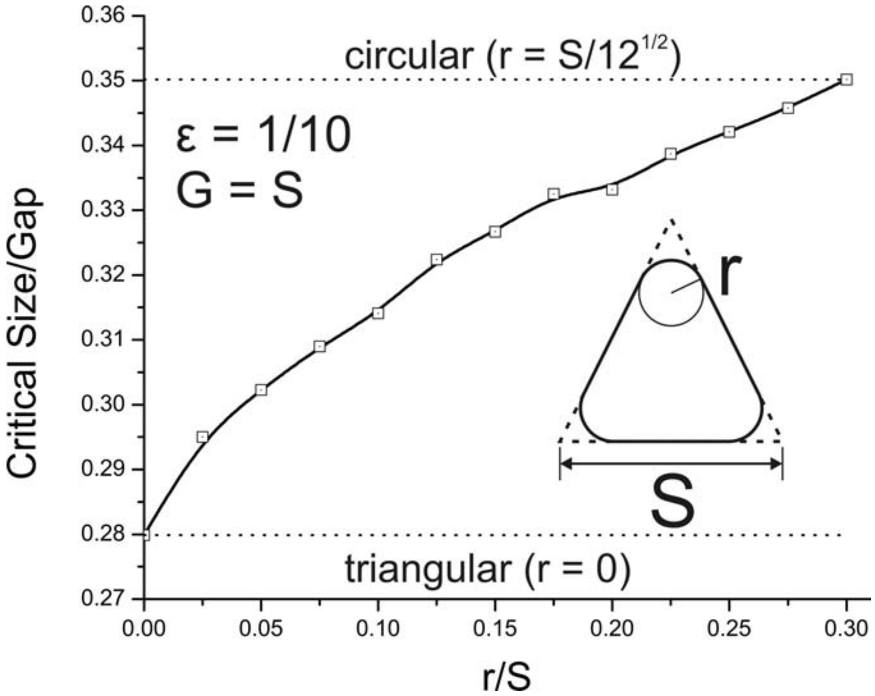

Figure 4.7: Effect of Vertex rounding on critical particle size as a ratio of the gap. Starting with 10 μm posts with 10 μm gaps, flow profiles across were numerically simulated across gaps between post with no vertex rounding (r=0) to complete vertex rounding ($r = S/12^{1/2}$). Critical size for array tilt $\epsilon = 1/20$ calculated for resulting gap is plotted as a function of ratio of the rounding to the initial triangle side length.

posts and base width between 2 and 40 μm were simulated and flow profiles across gaps were extracted for each array. Critical particle sizes were calculated for tilt angle $\epsilon = 1/10$ and plotted as a function of the ratio of the base width to the height of the triangular post. The figure shows that there is an optimal base to height ratio between 1.0 and 1.4 that minimizes the critical particle size to 28% of the gap. Similar to the result with regular polygons, increasing the width of the base beyond 1.4 times the height decreases the sharpness of the vertices and the critical particle size increases. On the other hand, decreasing the base width seems to make the base act more like a sharp vertex. As the base becomes narrower, the two sides of the gap begin to look the same and the flow profile more closely resembles one of the regular polygons with an even number of sides. Thus, further improvement beyond equilateral triangles by making the post vertices sharper does not seem likely.

The gains achieved by changing the post shape are degraded if care is not taken to maintain sharp post vertices. Figure 4.7 shows the effect of rounding the post edges on the critical particle size. An array with 10 μm posts, 10 μm gaps between posts, and tilt angle of 1/10 was simulated in COMSOL with the vertices rounded to various radii of curvature ranging from none (r = 0) to complete rounding where the final shape is a circle ($r = S/12^{1/2}$). Flow profiles across the gaps were extracted for each rounding and the critical size for the given tilt was calculated as a percentage of the new gap (10 μm plus the amount of vertex removed to round the vertex). As shown, the critical particle size, starting at 0.28 G when the post is completely triangular, increases 25% to 0.35 G as the post shape transitions from triangular to circular. This transition is a result of the loss of asymmetry in the flow profile that occurs as the vertices become more round. The transition suggests that the post edges should be made as sharp as possible relative to the post side length. Not captured in the figure, but also relevant is the increase in gap size that results from vertex rounding. For a fabrication process that produces a given vertex rounding, it is advisable to use larger posts (increasing S) to decrease r/S and preserve the gains discussed previously and maintain the designed gap size.

Examining the effect of the post to gap ratio on the critical particle size further demonstrates the benefit of using large posts. In circular posts, large posts with small gaps give a more parabolic profile while small posts and large gaps give a more plug-like profile. Figure 4.8 shows the effect of changing the post size on the critical particle size. An array with 10 μm gaps between posts and tilt angle of 1/10 was simulated in COMSOL with equilateral triangle posts varying logarithmically from 1 μm to 100 μm. Flow profiles across the gaps were extracted for each post size and the critical size for the given tilt was calculated as a percentage of the new. The critical particle size decreases with increasing post size until the post side length is about twice gap, and then remains roughly constant for increases in post size thereafter.

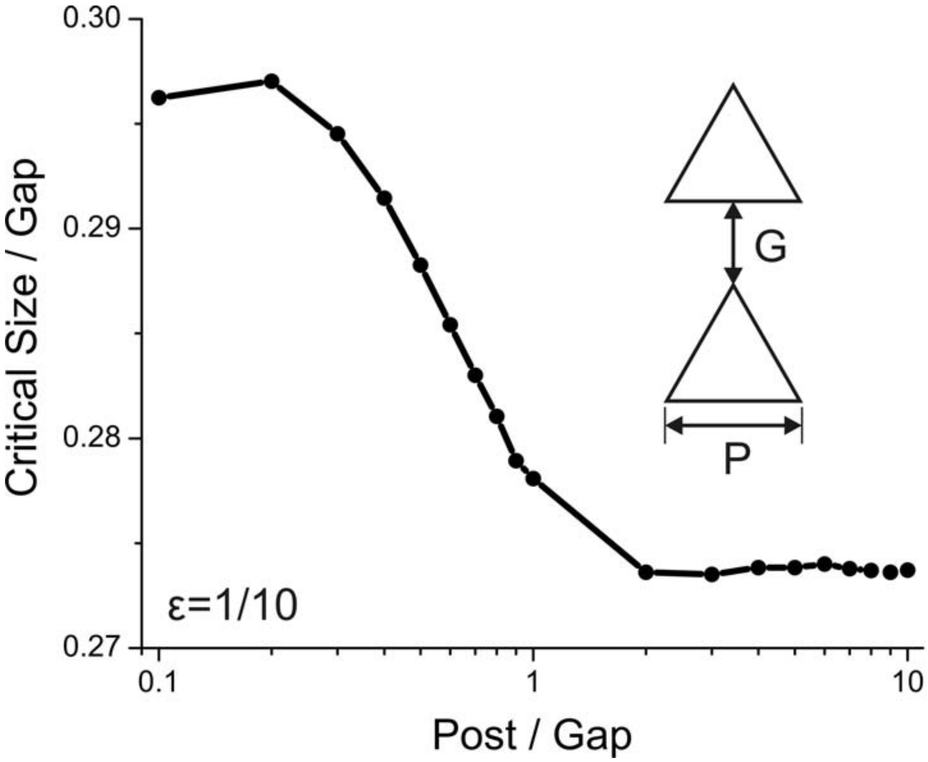

Figure 4.8: Critical particle size for arrays of triangular posts with varying post side length to gap ratios. Flow profiles across gaps between triangles were numerically simulated for arrays with varying side length. Gap between posts was fixed at 10 μm. Critical size for array tilt $\epsilon = 1/10$ calculated and plotted as a function of ratio of the side length to the gap height.

This transition underscores the effect of the varying post geometry on creating a skewed flow profile also shown in Figure 4.6. When the posts are smaller than the gap, they produce a flow profile that is more plug-like and less skewed towards the triangle vertex. It is therefore advisable to make the post side length at least larger than the size of the gap and probably twice the size of the gap to ensure a small critical particle size.

4.4 Trimodal Separations

Simulations suggest that if the flat of the triangle is used as the displacement surface instead of the triangle vertex as discussed in the rest of this chapter, there should

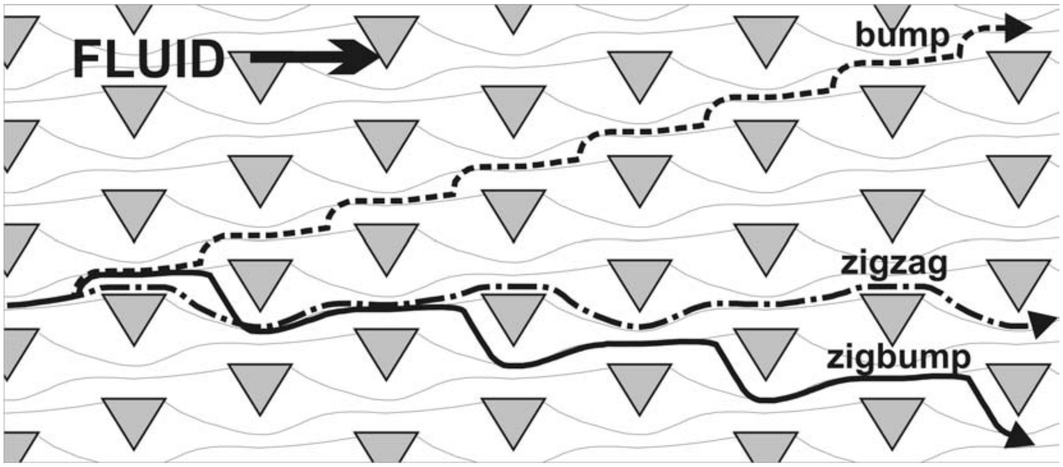

Figure 4.9: Simulated particle trajectories in DLD arrays with posts are oriented so that particles are displaced by the triangle flat. The usual bumping and zigzag trajectories are observed in addition to a third mode that moves in the opposite direction as the array tilt. These “zigbump” particles are displaced by the triangle vertex as they move through the top stream in a gap and fall in the same size range as those that show ratcheting behavior in oscillating flows discussed in Chapter 3.

be three particle separation modes. Shown in Figure 4.9, representative trajectories of the three displacement modes were were calculated in MATLAB using flow fields (v_x, v_y) extracted from COMSOL simulations of flow through an array with 10 μm posts with 10 μm gaps between the posts and array tilt of 1/3. 9.4 μm (bump), 8.0 μm (zigbump), and 1.0 μm (zigzag) particles were propagated along streamlines until the particle came within one radius of an obstacle. The particles were then shifted perpendicular to the surface of the obstacle a small distance ($\leq$50 nm) and allowed to continue forward, representing steric repulsion when particles are displaced by a post. From the figure, it can be seen that the 9.4 μm and 1.0 μm particles exhibit the standard behaviors observed in the DLD array while the 8.0 μm particle travels at an angle against the array tilt. While large particles are displaced upward as they traverse the array, these particles are displaced downward.

To explain the “zigbump” displacement mode, we need to look back to the previous chapter on the microfluidic ratchet. Because the post shape is asymmetric, there will be two critical particle sizes associated with the top and bottom of the post. Since the triangular posts are oriented such that the triangle flat is the displacement surface, the critical size for the bumping mode will be the larger of these two sizes. Therefore, particles below this size should follow follow the fluid flow in a zigzag trajectory. However, as we showed with the ratchet, it is possible that a particle can be smaller than the critical size for bumping along the flat, but larger than the critical size along the vertex. Particles that fell between these two critical sizes showed ratcheting behavior in an oscillating flow, and it is these particles that follow the zigbump trajectory. A particle below the critical size will sample each of the flow streams going through a gap evenly. When an intermediate-sized particle zigs around a post, it is in the stream closest to the triangle vertex. It is too large to fit within this stream, so it is displaced downward towards into the next stream. This displacement will not occur again until it zigs around another post so the resulting periodicity of this trajectory is $1/\epsilon - 1$. In Figure 4.9, the array is periodic after three columns of posts while the zigbump trajectory is periodic after two columns. The careful reader will have noticed this is also the case for the left to right motion of the ratcheting particle trajectory shown in Figure 3.4B.

The single displacement imparted by the post vertex reduces the periodicity of the particle trajectory by one column and makes intermediate-sized particles travel at a negative angle with respect to the flow direction and the array tilt. With some geometric manipulation, it can be shown that the zigbump displacement angle α is equal to $\frac{\epsilon^2}{1-\epsilon}$ for parallelogram arrays and $\frac{\epsilon^2}{1-\epsilon+\epsilon^2}$ for tilted square arrays. These displacement angles are plotted with respect to the array angle in Figure 4.10. As shown, they are always less than the array tilt angle and decrease rapidly with decreasing array tilt. For an array tilt ϵ of 1/5, the zigbump displacement angle α is expected to be around 1/20.

Experimental observation of this displacement mode has yet to be attempted, but is an informative example of the mechanisms at work in the DLD array. A particle

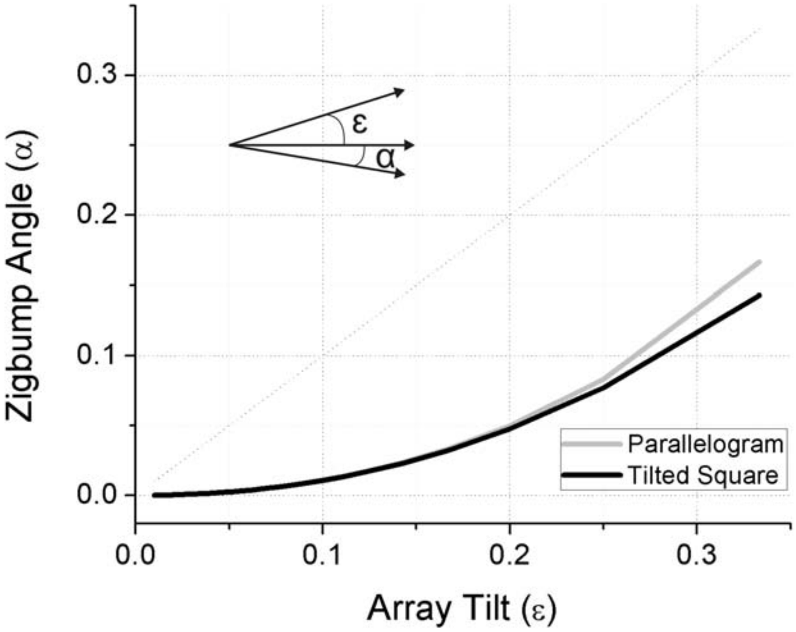

Figure 4.10: Zigbump displacement angle as a function of array tilt for parallelogram and tilted square DLD arrays.

will travel along a streamline unless it is too large to fit in a flow stream as it goes through a gap between posts, in which case it will be displaced into the next stream. While previous instances of the DLD array only showed displacement in the same direction as the array tilt, we have shown here that it is possible for particles to be displaced in a direction against the array tilt when different post shapes are used.

4.5 Summary

In this chapter, we have demonstrated that changing the post shape from circular to triangular in a DLD array results in a reduced critical particle size as a percentage of the gap. This allows smaller particles to be separated for the same gap and array tilt, larger array tilt for the same critical particle size and gap, and a larger gap for the same critical particle size and array tilt. This last improvement is especially useful as it allows arrays to be designed with a decreased chance of clogging and lower pressure requirement for a desired flow rate. Through a series of simulations, we showed that these gains are accomplished by inducing both a more plug-like flow along the post with a sharp vertex and by producing a shift in flux towards that vertex by having a flat edge on the opposite side of the gap. Of the shapes examined, equilateral triangles with sharp vertices and side length at least twice the size of the desired gap provided the greatest reduction in critical particle size and we contend that that future deterministic lateral displacement designs should employ equilateral triangular rather than circular posts. To take advantage of these gains, posts should be oriented such that particles are displaced by the triangle vertex, although we have shown trimodal separations are possible if the posts are instead oriented so the displacement surface is the triangle's flat edge.

Chapter 5

High Throughput Particle Separations

5.1 Introduction

Microfluidic devices have classically focused on processing or analyzing small volumes of fluid, preaching the virtues of less sample and reagent use while taking advantage of the the small channel dimensions to enhance analytical processes that rely on mixing [65]. However, there are many cases, such as searching for rare cells [19, 22, 23, 54] or industrial processing[31, 62, 71], which require large volumes to be processed, preferably in a short a time as possible. In this chapter, we will discuss efforts to produce DLD arrays capable of processing macroscopic fluid volumes. The is accomplished by designing arrays that are capable of being tiled on a single device layer and stacked vertically, allowing many devices to be run in parallel while minimizing external connections. We then increase the flow rate in individual devices by increasing the driving pressure.

A spring-loaded manifold was designed to accommodate multilayer devices and the increased pressure load and flow rates of 10 mL/min have been achieved with

50 psi applied pressure on a single layer device. These results constitute a 10^5-fold improvement over the 10s of $\mu L/min$ historical flow rates in DLD arrays [11, 25] and a 100-fold improvement over more recent efforts by Inglis *et al.* [32] and are the fastest reported operation of these devices. With internal velocities exceeding 1 m/s and Re $\sim$ 40, we confirm that the size-based separation functionality is preserved even outside the low Reynolds number flow regime. Within the area of continuous flow particle separations[20], these results represent the fastest reported volumetric flow rates with only recent work from the Di Carlo[27] group surpassing flow rates of 1 mL/min. A clear approach to higher throughput is to increase the number of arrays operating in parallel on a single planar device or vertically stack devices using the method we present.

5.2 Device Design

Devices are designed to use a minimal number of input and output connections and to be easily integrated so many arrays can be operated in parallel. The layout of a device subunit is shown in Figure 5.1. While the array parameters may vary, each mirrored arrays presented in this chapter and the next is 2.5 mm wide and 25 mm long. Each single layer device has three mirrored array units for a total array width of 7.5 mm and length of 25 mm. The function of this array is to concentrate dilute particles above a given size from a single input and collect them at a narrow collection output while discarding any unconcentrated particles as waste. There are two mirrored arrays within a single device, the top array in the figure directs particles downward while the bottom array directs them upward. This allows the device width to be doubled without increasing the array length, which must typically be scaled with the array width as W/ϵ to ensure the array displaces all large particles to the central wall. Since the channel resistance scales linearly with the device length and the mirror

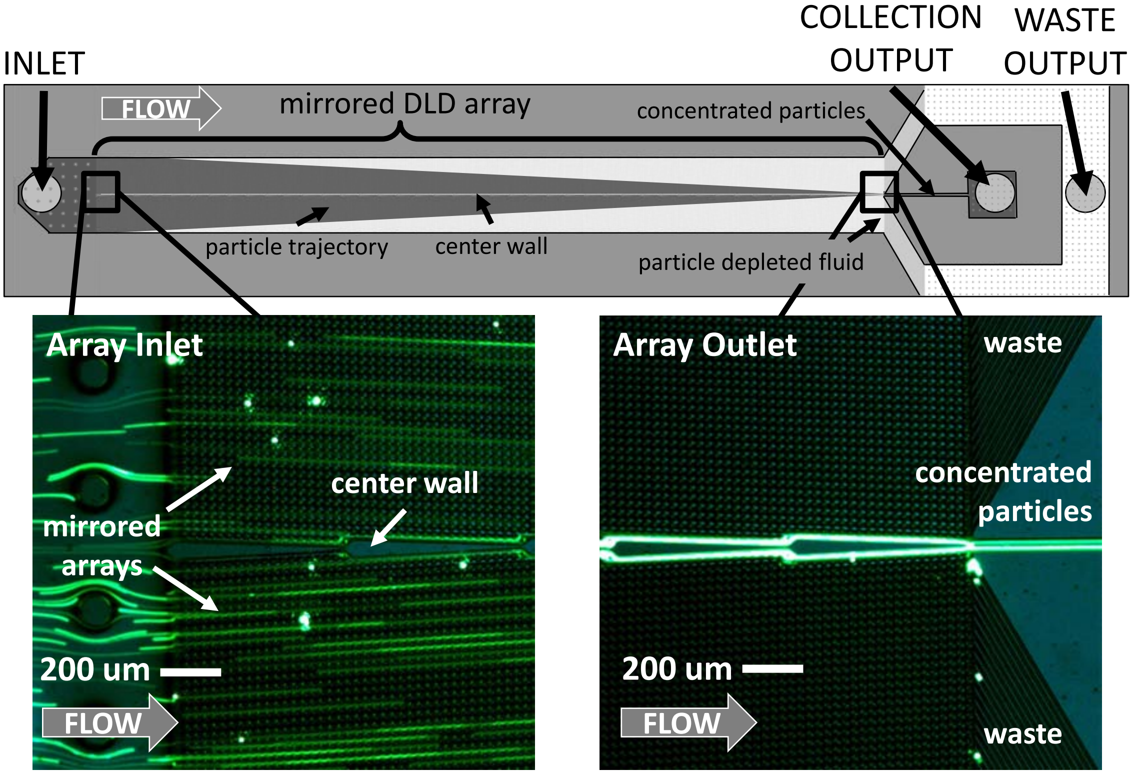

Figure 5.1: **High Throughput Device Subunit**. A concentrator with one input and two outputs (collection and waste) is used. Devices are designed to allow tiling in plane and vertical stacking using etched through holes to increase throughput. Fluorescent micrographs of the trajectories of 3.1 μm beads in arrays with 12 μm gaps, 18 μm triangular posts, 1/20 array tilt and 2.0 μm critical size highlight device function. Using a mirrored design, large particles dispersed in the inlet are focused against the central channel wall, where they can be collected at the narrow collection output while other particles enter the waste outlet.

design allows two arrays to be operated in parallel, this design provides twice the flow rate without increasing channel resistance. This is the central motivation for parallelization. By running many arrays in parallel, the cross section for separation can be increased without increasing the device length, resulting in higher throughput for the same applied pressure.

Triangular posts are used for increased throughput and less clogging following the discussion in the previous chapter and Inglis' wall design is used to ensure flow uniformity near channel walls where particles are concentrated [28]. The device functionality is shown in the fluorescent trajectories of 3.1 μm particles in an array with

12 μm gaps, 18 μm posts, 1/20 array tilt and 2.0 μm critical size in Figure 5.1. Beads that are uniformly distributed at the array inlet are directed towards the central wall as they travel through the array. At the outlet, nearly all of the beads are concentrated against the wall and collected in the narrow collection output. This simple design is ideal for a sample where one wants to collect all of the particles in the fluid, but has some limitations with heterogeneous mixtures of particles because there is no input buffer stream next to the central wall to isolate collected particles from the input fluid. As such, there will always be a background of small particles in the collected output and the enrichment factor will be limited to the ratio of the separation efficiency to the reduced volume from the inlet to the narrow collection channel. The extra input buffer stream was omitted for experimental simplicity in these high throughput experiments.

5.3 Parallellization & Stacking

Process throughput can be scaled up without increasing the driving pressure by running many devices in parallel. Shown in Figure 5.2A, three of the design subunits presented in the previous section were tiled to form a single planar device. Made in silicon with etched through-wafer holes, these devices can then be stacked vertically using the through holes for alignment. Because the diameter of the device through holes (1 mm) is much greater than the channel dimensions ($\sim 10\,\mu m$) and the resistance scales as the smallest dimension cubed or to the fourth power, a deep stack of through holes should still be considered a zero resistance connection and we will consider stacks of devices as operating in parallel with the same applied pressure gradient. Devices are fabricated by growing a thick ($\sim 1\ \mu m$) oxide on a silicon wafer and patterning the device features in the oxide using photolithography and wet etching with BOE. The undercut on the device features is approximately the same as

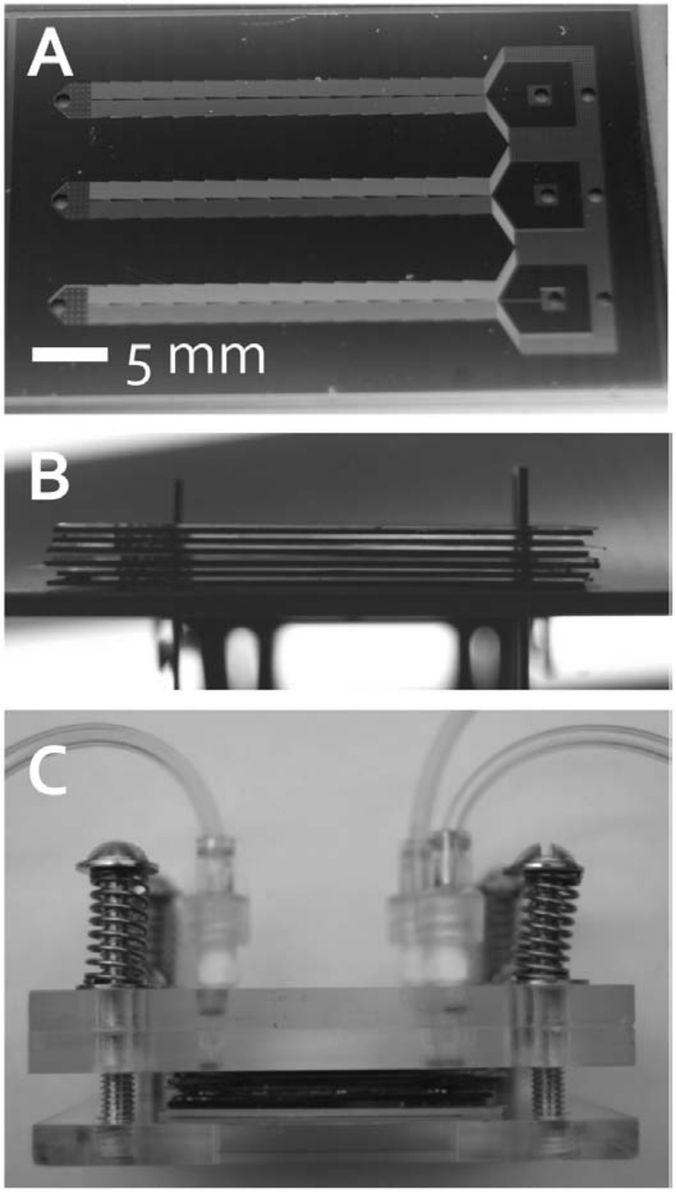

Figure 5.2: **Device Parallelization**. **A** Three devices subunits from Fig. 5.1 are tiled to make a single layer device fabricated in silicon. **B** Six devices are stacked vertically using PDMS gaskets with punched through holes. Steel rods threaded through etched through-wafer holes are used for alignment between layers. **C** Spring-loaded manifold accomodates multilayer devices and routes input/output from array subunits together into three (input, cells, waste) macroscopic connections.

the thickness of the oxide so design dimensions should take this into account. Device through holes are then patterned in on the wafer in 8 μm of AZ4330 photoresist. Through wafer holes and device features are etched using a Bosch process in a deep silicon etcher. Because the etch recipes are optimized for photoresist etch masks, we found that the etch depth in the device features was limited to about 60 μm for a 1 μm oxide etch mask and that is the etch depth for the devices presented in this chapter. However, a process developed by Joseph D'Silva using backside alignment and photoresist to pattern both device and through hole features has recently been developed that allows fabrication of much deeper devices.

Devices are stacked vertically using a PDMS gasket in between silicon layers to seal device features and bottom of next device. Gaskets are made by spinning approximately 10 g of uncured PDMS on a 10 cm trimethoxysilane-coated silicon wafer for 1-2 minutes and then curing for 1 hour at 65 $^{\circ}C$. The PDMS sheet is then cut to size, holes are punched with a hollow syringe tip to line up with device through holes, and the sheet is used to seal a device. The last device in the stack is sealed with a PDMS-coated glass slide to allow optical inspection during operation. Six devices are shown stacked in Figure 5.2B with PDMS gaskets between each layer. This stack is then place in a spring-loaded manifold that routes all of the internal connections to three macroscopic inlet/outlet connections made by luer-lock connections. Shown with a multilayer device mounted in Figure 5.2C, the manifold is designed to withstand high applied pressures. Tests of the failure mode of the manifold showed that devices could withstand up to 70 psi, at which point the PDMS gaskets delaminate from the silicon devices. It is possible that this failure mode could be overcome by using oxygen plasma to permanently bond the gaskets to the devices or making the devices out of plastic that can be bonded together, in which case the next most likely failure point would be at the o-rings that connect the device in/out connections to the manifold.

We can estimate the pressure at which the device seals will break by dividing the applied force from the springs by the area of the array, where most of the pressure drops. In the current configuration, four springs with a spring constant of 28.5 N/cm are compressed 0.6 cm when screwed into the manifold, applying a total force of 73.1 N. The total array area on a single layer device is 3 x 25 mm x 2.5 mm = $1.9x10^{-4}m^2$, which corresponds to a pressure of 390 kPa or 56 psi. If the internal pressure from the flow exceeds this value, then we would expect the Si-PDMS to delaminate. This underestimates our experimental observations but is a useful guideline for how high a pressure can be safely applied without breaking the device seals and indicates using stronger springs or compressing them further may allow higher pressures to be used.

5.4 Transport Characteristics

To assess the flow rates we could expect in future experiments, a simple measurement of the pressure drop across an array with a given flow rate was performed. A single layer device with 42 μm gaps, 58 μm posts, 1/20 array tilt and 60 μm etch depth was used. The flow rate was controlled by a syringe pump and the pressure was measured with a gauge attached at the manifold to the device inlet. Flow rates were increased from 0.5 mL/min to 8 mL/min before the syringe ran out of fluid. The running fluid was phosphate-buffered saline (PBS) with 1% bovine serum albumin (BSA). As shown in Figure 5.3, there is a linear relationship between the flow rate and pressure across the array with a slope of the linear fit of 5 psi/(mL/min)[1] . Flow rates of up to 10 mL/min have been observed in other experiments with no leakage, which corresponds to 50 psi applied pressure. The three 2.5 mm wide devices etched 60 μm deep have a cross sectional area of 0.45 mm^2 in the open areas and 0.18 mm^2 in the gaps between posts. A flow rate of 10 mL/min corresponds to average fluid velocities of 37 cm/s in the open areas and 92 cm/s in the gaps between posts. Numerical

---

[1] Slope depends linearly on the fluid viscosity. Water was used for this experiment

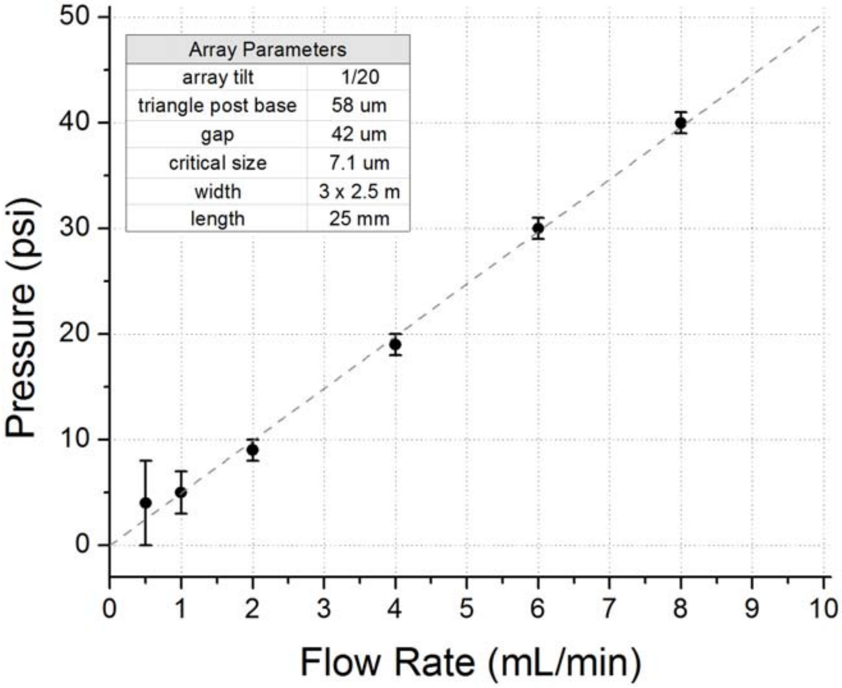

Array Parameters	
array tilt	1/20
triangle post base	58 um
gap	42 um
critical size	7.1 um
width	3 x 2.5 m
length	25 mm

Figure 5.3: Pressure across single layer device as a function of flow rate for a single layer device with 58 μm posts and 42 μm gaps.

simulations show that the maximum velocity in the device under these conditions is 1.5 m/s with shear rates on the order of $10^5\ s^{-1}$ near the post vertices. The Reynolds number Re with $L = 40\ \mu m$ and $v = 0.9\ m/s$ is approximately 40.

It is important to understand how these results will scale with different array parameters. We can use a fluidic version of Ohm's law where the ratio of the pressure drop ΔP to flow rate Q is equal to a hydrodynamic resistance R. Darnton *et al.* showed that the hydrodynamic resistance of a rectangular channel is proportional to $R \sim L/hZ^3$, where L is the channel length, Z is the smaller channel dimension and h is the other dimension [10]. In DLD arrays, the smallest dimension is typically the gap ($Z = G$) while the device depth h is the larger dimension. For simplicity, we will model the DLD array as G/W rectangular channels in parallel, where G is the gap between posts and W is the total array width. The resistance of the array is then $R \sim \frac{G}{W}\frac{L}{hG^3} \sim \frac{L}{hWG^2}$, assuming that the gap is the smaller dimension because we will want deep devices to maximize throughput. As stated earlier, the array length is usually about W/ϵ so particles are completely displaced across the array so $R \sim \frac{W}{\epsilon hWG^2} \sim \frac{1}{\epsilon hG^2}$. Finally, a power law fit of critical particle size as a function of gap G and array tilt ϵ shows that $D_c \sim \epsilon^{1/2}G$ (exponent = 0.53 for circular posts, 0.65 for triangular posts) so

$$R \sim \frac{1}{hD_c^2}$$

We could have chosen 2/3 as the exponent in the power law fit which would give $R \sim \frac{\epsilon^{1/3}}{hD_c^2}$ and a weak dependence on the array tilt, but this term does not have much variation over the typical range of array tilt from 1/5 to 1/100 so the previous relation should still hold. From this relationship, we can see that deeper channels are an easy way to get higher flow rates, with the resistance inversely proportional to the channel depth, and that the flow resistance will increase quadratically when smaller critical sizes are used. For example, the array from the previous experiment was designed with a 7 μm critical size. If we were to try similar experiments with an array of the width with 1 μm critical size by decreasing the gap G while keeping array tilt ϵ, width W, length L and etch depth h the same, we should expect a flow rate 50 times less for the same applied pressure.

5.5 Re $\sim$ O(1) Considerations

At the velocities presented in the previous section, the channel Reynolds number is large enough that low Re simplifications to the Navier-Stokes equations are no longer applicable and inertial effects must be considered. These affects, which typically take the form of forces transverse to the flow in the form of lift from shear-gradients and wall effects are only somewhat understood in simple geometries such as straight or curviilnear channels [13]. As such, a complete treatment on their effect of particle motion in the complex geometries of DLD arrays would be quite difficult to obtain and we will just summarize the relevant forces.

Forces that act transverse to the flow direction, and hence can cause particle migration between streams, are relevant in the operation of the DLD array. Di Carlo *et al.* have shown that inertial lift forces have two forms depending on particle location in the channel. A "shear-gradient" lift that is dominant in the center of a channel and scales as $F_L \sim \rho v^2 a^3/L$ whereρ is the fluid density and v,a and L are characteristic velocity, particle diameter and length scales, respectively. This force pushes particles in the center of a channel towards the walls. A "wall effect" lift that dominates near channel walls scales as $F_L \sim \rho v^2 a^6/L^4$ and pushes particles away from walls towards the channel centerline. Of these, wall lift is likely to be relevant to particle dynamics in the DLD array because the trajectory particles take depends on their motion in the stream near a post wall. Since this force has a strong dependence on particle size, it may decrease the effective critical size as particles near the critical particle size are pushed across a stream boundary by some combination of displacement from posts and lift forces from the flow near the wall. Experimental observation of the behavior of various beads of well-defined size across a range of flow velocities will likely be necessary elucidate effect of intermediate Reynolds number on the critical sorting size in DLD arrays.

5.6 Summary

We developed a highly parallelized DLD array architecture for processing macroscopic fluid volumes by operating many arrays in parallel and showed flow rates on the order of 10 mL/min with a single-layer device. With internal velocities exceeding 1 m/s, we showed that the DLD array continues to function even outside of the low Re regime and this flow rate represents the fastest ever operation of a DLD array and the highest reported flow rate in any microfluidic sorting application. We developed a spring-loaded manifold to accommodate high pressure operation of these devices and allow multiple devices to be stacked vertically using a PDMS gasket in between silicon layers.

Chapter 6

High Throughput Applications

6.1 Introduction

In this chapter, we apply the high throughput DLD arrays from the previous chapter towards two problems where processing large volumes is necessary. We first discuss isolating rare viable circulating tumor cells from blood and then discuss concentrating algae from culture for biofuel production.

6.2 Circulating Tumor Cells

6.2.1 Motivation

Malignant cancer is thought to spread throughout the body to form secondary tumors via the circulatory system. Circulating tumor cells (CTCs) have been identified in the blood of patients with metastatic disease and can be used as a diagnostic for the severity of disease and to assess the efficacy of different treatment strategies [9]. Much of the recent work in this area has focused on the development of diagnostics to differentiate and enumerate CTCs from blood, with the most prominent results relying on capturing cells on epithelial antibody-coated surfaces in microfluidic flow channels

[54, 67]. However, there is a critical need to isolate, propagate and characterize large numbers of viable circulating tumor cells to expand on understanding of the biology of metastasis [48], enable new methods for studying the emergence of drug resistance [39], and aid in the development personalized treatments [61]. However, since antibody-based methods strongly bind cells on surfaces, viable cells cannot be retrieved from these devices.

CTCs (diameters 15 - 30 μm) are larger than other cells in blood (2 - 15 μm) [50], giving the possibility of enrichment with a size-based separation technique. Several methods involving membrane based filtration [42, 75, 80] or devices relying on inertial effects [4, 27] have been developed to exploit this size difference. Both of these approaches have yielded CTCs from blood with high capture efficiencies and enrichment factors. However, because of the rarity of these cells in blood ($10^1 - 10^3$ cells/mL) [9] compared to other cells in the blood (red blood cells - 10^9 cells/mL, platelets - 10^8 cells/mL, and white blood cells - 10^6 cells/mL), large volumes of blood will have to be processed to deliver a sufficient number for study. In these cases, clogging may be an issue with membrane-based technology and the throughput of inertial techniques is limited by the heavy dilutions that are necessary to limit reductions in separation resolution that result from cell-crowding.

In this section, we discuss preliminary experiments towards high flow rate, continuous-flow capture of viable CTCs from blood using deterministic lateral displacement arrays. Using the high throughput design from the previous chapter, we demonstrate that DLD arrays can capture CTCs from milliliter volumes of blood at mL/min flow rates with high efficiency, little enrichment of background white blood cells and no effect on cell vitality or device clogging. Further development in the device design will be needed to remove background blood cells, but this is a promising first step towards a device that can quickly capture viable CTCs from blood for further study.

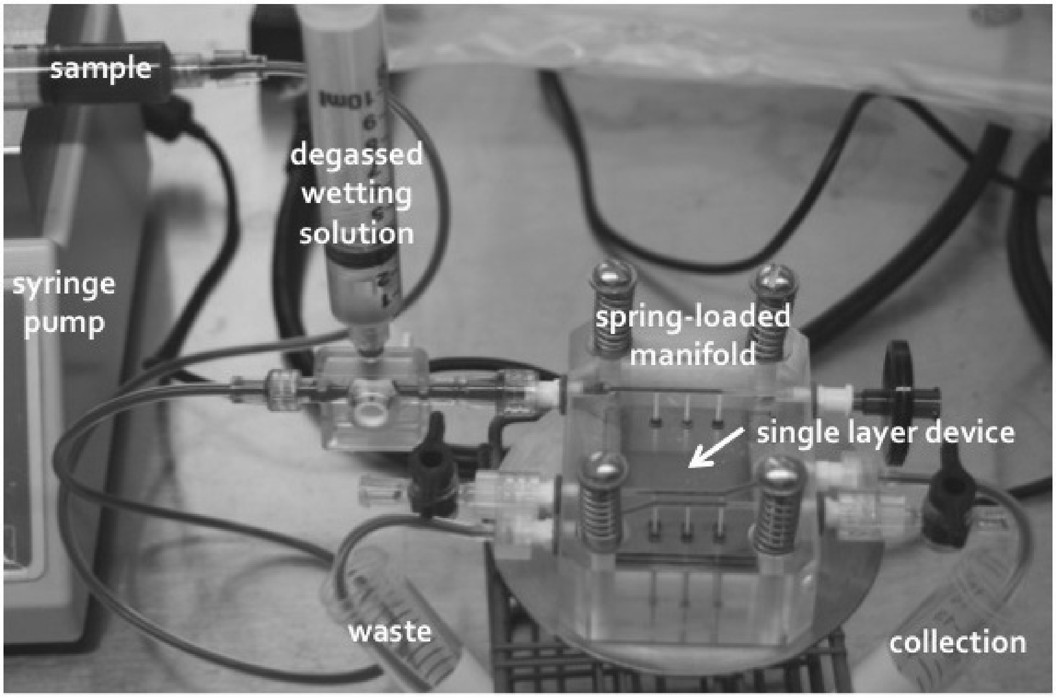

Figure 6.1: **Experimental setup for high throughput experiments**. Sample fluid, usually spiked with cancer cells, is driven through device with a syringe pump to waste and collection outputs. Spring-loaded manifold maintains seals during high pressure operation (up to 70 psi).

6.2.2 Experimental Design & Procedures

A single layer silicon device with a PDMS-coated cover slide was used in these experiments to demonstrate the potential of DLD arrays for high throughput enrichment of viable cancer cells from blood. Arrays with 42 μm gaps, 58 μm triangular posts, 1/20 array tilt, and 7.0 μm predicted critical size were used in the design architecture presented in the previous chapter. Following the discussion from Chapter 4, triangular posts allow a 55% larger gap between posts compared to circular posts with the same critical particle size. The experimental setup is shown in Figure 6.1. Manifold, devices, and tubing are first wet with a degassed running solution of 1x PBS (isotonic with blood), 1% BSA (reduces cells sticking), and 1 mM EDTA (anticoagulant). Hydrophobic filters attached to the manifold allow air to be pushed out and ensure the setup is free of bubbles. 5 mL of fluid was processed in each experiment at various flow rates. For flow rates less than 1 mL/min, a magnetic stir-bar was placed in the sample syringe and placed over a stir-plate to minimize cell sedimentation.

Experiments were performed with approximately 10^7 cancer cells from breast or prostate cell lines in 1 mL of growth medium spiked into the the running solution or blood diluted with the running solution. The cancer cells are cultured using standard methods and used immediately after passage. Premalignant (MCF10A) and malignant (MDAMB231) epithelial breast cells contained a GFP or RFP construct that allowed them to be easily differentiated from other non-fluorescent cells in solution. Breast cancer cells were provided by Joseph Aslan of the Scripps Research Institute. In experiments with blood, a nucleic acid stain (SYTO 9 for green or SYTO 61 for red) in the alternate color was applied to quantify leucocytes. Blood was supplied by donors from the Interstate Blood Bank (Memphis, TN), shipped overnight and used within one day to ensure white blood cell viability. After experiments were completed, fluids were disposed of in a 10% bleach solution and manifold and tubing were rinsed with a 10% bleach solution and then soaked in 1% bleach in DI water until their next use. Glass lids were removed from silicon devices and devices were rinsed with bleach, Contrad 70, and soaked in DI water until their next use. Before reuse, devices were rinsed with acetone and isopropanol, dried, and cleaned in oxygen plasma for 90 s.

6.2.3 Results

Device functionality was confirmed by observing the trajectories of malignant MDAMB231 breast cells expressing GFP with epifluorescent microscopy at a flow rate of 100 $\mu L/min$. This is shown in Figure 6.2. Using only cells in media and the wetting solution, we can clearly see the trajectories of cells at the inlet and outlet of the device. From the single device inlet, cells are evenly dispersed as they enter the array and follow a bumping trajectory. By the time the cells reach the outlet, the

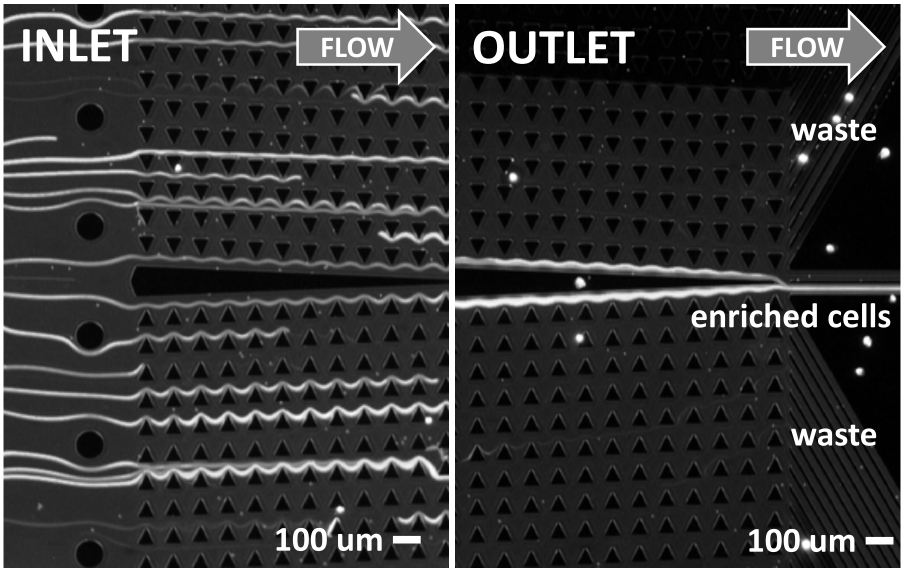

Figure 6.2: **CTC enrichment in DLD array**. Trajectories of GFP-expressing MDAMB231 breast cells in an array with 42 μm gaps, 1/20 array tilt, and 7 μm critical particle size at device inlet and outlet at flow rate of 500 $\mu L/min$. Cells are evenly dispersed at inlet but are concentrated against central wall at outlet and directed to narrow collection outlet. Chip design is described in Figure 5.1.

mirrored array has focused them against the central wall and they are directed into the collection output at the end of the array.

We confirmed that the DLD array still functions at higher flow rates by processing premalignant MCF10A breast cells spiked in the wetting solution at a flow rate of 10 mL/min. 1 mL of growth medium with $\sim 10^7$ cells was diluted to 10 mL with the wetting solution and 5 mL of sample was processed in 30 s. Concentrations and size distribution of cells were measured for input, collection, and waste solutions using a Coulter counter with a threshold of 9 μm. From an initial concentration of 3.75 x 10^6cells/mL with average size 19.5 μm, the collection output had a concentration of 2.1 x 10^7 cells/mL with average size 19.5μm while waste output had a concentration of 3.7 x 10^5 cells/mL with average size 19.0 μm. Factoring in the volume of each output ($V_c = 0.8$ mL, $V_w = 4.2$ mL), we can calculate the capture efficiency as the ratio of cells in the collection output to the total number of cells in both outputs $\frac{\#\,collected\,cells}{total\,cells} = \frac{C_cV_c}{C_cV_c+C_wV_w}$. Using this definition, 91% of the targeted cells were collected by the device. Ideally, 100% of the cells would end up in the collection channel, but there may be a reduction in collection efficiency from cell crowding against the channel wall or velocity-induced morphology changes reduce the effective cell size as suggested by the slight difference in average size between waste and collection channels. It is also possible that a portion of the cell population was below the critical size as these cells tend to have a wide size variation [50].

Experiments were then performed with cancer cells spiked into blood to assess the separation efficiency for isolating CTCs from blood. 500 μL of blood was added to 1 mL of growth medium with $\sim 10^7$ malignant MDAMB231 breast cells and then diluted to a total volume of 10 mL with the running solution. 5 mL of this mixture was processed at 10 ml/min flow rate and the output solutions were analyzed with a flow cytometer. MDAMB231 cells used expressed a red fluorescent protein dTomato that was used to distinguish them from other cells in the mixture which had no fluorescence. 50,000 cells were analyzed in each run and the number of large, fluorescent cells were enumerated from multivariable analysis. 4.9% of the input cells were cancer cells, while 16.7% of collection output cells and 0.6% of waste output cells were cancer cells. If we assume that the concentrations of other cells remain constant, we can normalize these percentages to the ratio of cancer cells to other cells in each solution and get 0.05, 0.2 and 0.006 for input, collection and waste solutions respectively and a capture efficiency in these conditions of 86%.

Finally, we examined whether white blood cells, which have may some size overlap with CTCs, were concentrated by the arrays. Future designs for this application will incorporate an input buffer stream so that CTCs can be displaced into a solution with no background blood cells. If WBCs are concentrated by the device, then both detection and propagation of viable CTCs will be much harder because there are

>1000 times as many WBCs than CTCs in blood. 2 mL of whole blood was diluted to 10 mL with the running solution and one drop ($\sim 100 - 200\,\mu L$) of $5.0\,\mu m$ green beads (Duke Scientific, 1% solids). A red nucleic acid stain (SYTO 61) was applied to label white blood cells and the solution was processed at 5 mL/min because of the increased fluid viscosity from using a high volume fraction of blood [15]. The concentration of beads, which are below the critical size, should remain constant in every solution so they act as a reference to measure the change in concentration of white blood cells. The ratio of white blood cells to beads was measured optically with an epifluorescent microscope that allowed observation of red and green fluorescence. From an initial ratio of 1.8±0.5 WBC:bead, we observed a ratio of 1.9±0.4 WBC:bead in the collection channel and 1.2±0.3 WBC:bead in the waste channel. This suggest that may be a mild concentration of leucocycytes by the the array which may warrant further study. It is possible a small number of leucocytes will always be present in the enriched sample because of size overlap. In this case, it may still be possible to propogate cells via preplating techniques [35].

6.2.4 Viability

Cell viability was measured to ensure the high shear rates in the array did not damage cells. The typical range of shear rates in the body is 10 to $10^3\,s^{-1}$ [15]. While simulations suggest that shear rates exceed $10^5\,s^{-1}$ at 10 mL/min flow rate very close to the post vertices, here we will use a simple estimate of the maximum velocity in the gap divided by half the gap. This gives a quick estimate of the order of the shear rate $\partial v_x/\partial y$. Cell viability is measured by application of 0.4%w Trypan blue in saline at a 10:1 dilution to input and output samples, vortexing, incubating for 5 min at room temperature, and examining the resulting solution with a haemocytometer. Trypan blue is a vital stain that selectively colors dead cells blue. An example of a mixture of live and dead cells is shown in Figure 6.3, which shows MDAMB231 cells that were

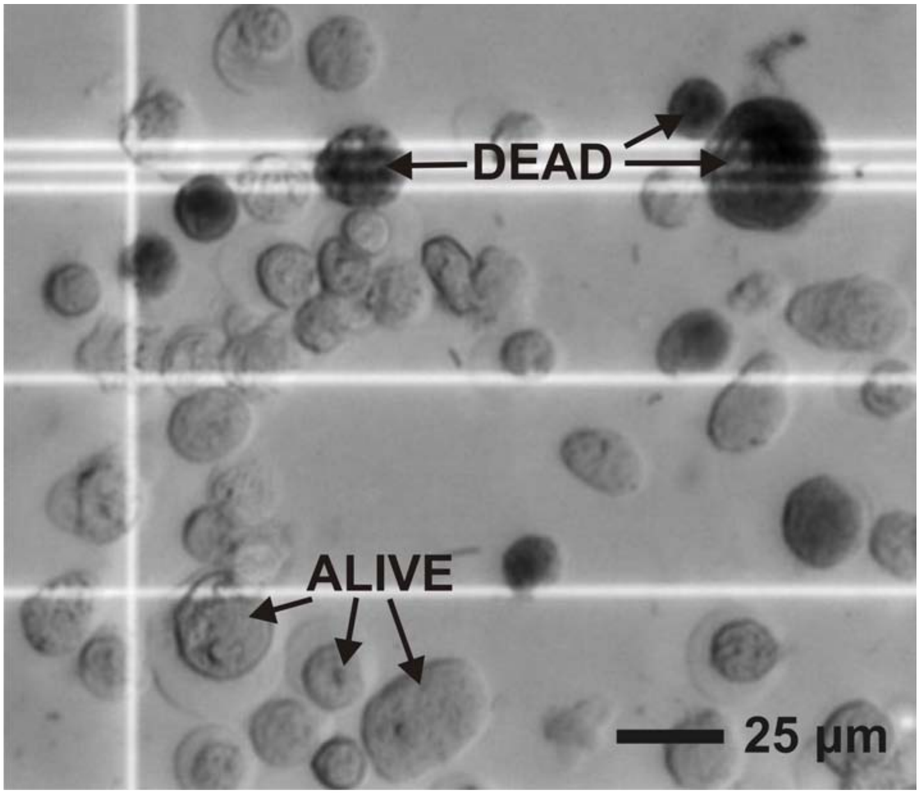

Figure 6.3: Vital stain Trypan blue is used to assess cell vitality. Live cells can exclude the die and appear transparent while dead cells absorb the dye and appear black. Pictured cells are MDAMB231 breast cells that were intentionally left in a vial for 16 hours after passage to produce a mixture of alive and dead cells.

intentionally left for 16 hours in a vial in the incubator after passage. There is a clear difference between live cells, which appear transparent, and dead cells, which appear black.

Passing through the DLD array had no effect on cell viability in several different cell lines suspended in a 1x PBS, 1% BSA, and 1 mM EDTA solution across a wide range of flow rates. In experiments, summarized in Table 6.1 with three epithelial cell lines (MDAMB231, PC3, MCF10A) at various flow rates from 0.1 to 10 mL/min, greater than 95% of the cells survived in each experiment. PC3 are malignant prostate cancer cells provided by the Getzenberg Lab at Johns Hopkins University. While the shear rates in these devices greatly surpasses physiological levels (1-2000 s^{-1} [18], we speculate that the reduced exposure time at the higher flow rates limits cellular

Flow Rate (mL/min)	Cell Type	Viability	Cells Counted	V_{max} (cm/s)	Shear Rate (s^{-1})	Transit Time (s)
0.1	MDAMB231	0.95	61	1.5	750	7.0
0.1	PC3	0.96	28	1.5	750	7.0
0.5	MCF10A	0.96	51	7.5	3750	1.4
5.0	MCF10A	1.00	123	75	37500	0.14
10.0	MCF10A	0.99	125	150	75000	0.07

Table 6.1: **Vitality Experiment Summary.** V_{max} defined as maximum velocity across a gap extracted from numerical simulation, shear rate $\partial v_x / \partial y$ estimated as maximum velocity in the gap divided by half the 42 μm gap. Array length is 25 mm.

damage. At 10 mL/min, cells traverse the entire 25 mm array in about 70 ms. This observation matches with observations of white blood cells in a rotary pump that suggest shear-induced damage is an integral effect [69]. That is, cell vitality decreases the longer cells are exposed to high shear. Experiments done by Di Carlo *et al.*[26] to examine gene expression in cells exposed to high shear showed no significant changes. As a result, we do not expect shear-induced cell death or alteration to be a significant limitation in the operation of these devices.

6.2.5 Future Directions

These experiments demonstrated that high efficiency capture of CTCs from blood is possible at flow rates greater than 1 mL/min with no effect on cell vitality. These results open up the possibility of developing a continuous-flow technique for rapid collection of viable circulating tumor cells from the blood of patients with metastatic disease. Capturing and propagating viable cells from patients could allow various chemotherapeutic treatments to be studied in vitro to determine which may be the most effective in vivo and allow better study of the development of drug resistance. However, several important improvements must be made to the current design. Because this device has only a single inlet, there will always be a background of blood cells in the collection output that may interfere with attempts to propagate cells. A better design would add a second buffer input that large cells could be directed into to minimize the background of other cells from blood. While there is no evidence that cells are damaged by flow through the device, additional experiments should be performed to ensure that cells cultured from these experiments are healthy when grown in culture.

6.3 Biofuel Algae

6.3.1 Motivation

Alternate, renewable energy sources are needed to offset consumption of petroleum-based fuels, minimize the effects of fluctuating oil prices, and meet the needs of increased energy security. Biofuels produced from renewable sources of biomass are a promising candidate to meet this need. Of the potential sources of biomass, microalgae stand out for their ability to produce oil at much higher densities per unit area of land used than crop sources [7, 41]. Furthermore, algae can be grown on non-arable land that will not compete with food crops, can use non-potable water as a growth medium, and will fix large quantities of CO_2 [73]. Biofuel derived from algal sources have the potential to broadly compete with petroleum-based fuels without adversely affecting supply of food and other crop products.

One current challenge in algael biofuel production is to reduce the cost so that it is competitive with petroleum-based fuels. A significant portion (20-40%) in the traditional processing cost comes from concentrating (dewatering) the algae from the dilute concentrations at which they are cultured to levels necessary for oil extraction [2]. This key step is classically performed by centrifugation, which is costly, energy intensive and must operate in a batch processing mode. In this section, we present a scaleable microfluidic separation technology that can continuously concentrate algae from culture using DLD arrays and operated passively using the pressure head from a tank. Using the high throughput architecture presented in the previous chapter, we designed arrays to concentrate two species of algae and that produed a 10 times concentration increase while capturing 51% of the algae that passed through the device. One limitation that appeared is the tendency of algae to stick to device surfaces in areas with slower flow, resulting in device clogging. While we show that it is possible to concentrate algae using a microfluidic device, further development in manufacturing materials and coatings will be necessary to scale up this technique to handle industrial-scale fluid volumes.

6.3.2 Experimental Design

In these experiments, a single layer silicon device with a PDMS-coated coverslide was used to concentrate algae in solution. Arrays with 12 μm gaps, 18 μm posts, 1/15 array tilt, and 2.5 μm predicted critical size and 60 μm etch depth were used in the design architecture presented in the previous chapter. Triangular posts allow a 40% larger gap between posts compared to circular posts with the same critical particle size. The experimental setup is shown in Figure 6.4. Manifold, devices, and tubing are first wet with a degassed running solution of algae growth medium with 1 g/L pluronic F108 (surfactant). Hydrophobic filters attached to the manifold allow air to be pushed out of the manifold to ensure the setup is free of bubbles.

Experiments were performed by flowing several mL of *Neochloris oleoabundans* or *Chlorella* algae from culture through devices and analyzing waste and collection solutions in a Coulter counter. *Neochloris* algae were obtained from the UTEX Culture Collection grown in an artificial sunlight ($\sim$ 3000 Lux) environment at 26^{o}C in Alga-gro Freshwater Medium (Carolina Biological) with humidified air bubbled into the culture vessel. *Chlorella* algae were obtained from our industrial collaborator Phycal LLC and grown in similar conditions but using High Salt medium. Algae were grown to a density between between $10^8 - 10^9$ cells/mL and between 4 and 10 mL of undi-

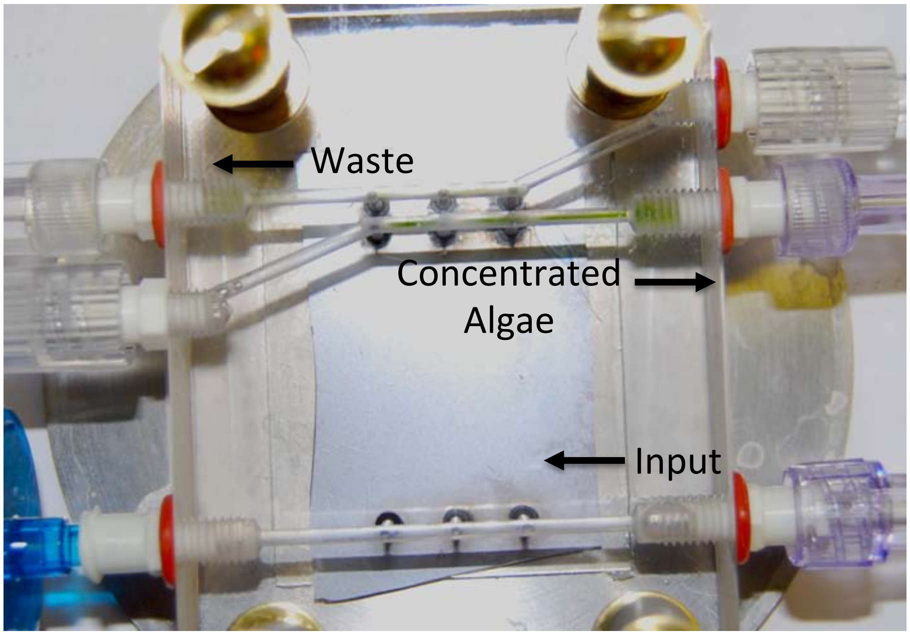

Figure 6.4: Algae Dewatering Experimental Setup. Algal culture is pushed through the device with a syringe pump and concentrated algae and waste fluid exit the device into collection tubes for analysis.

luted cell solution was processed in each experiment. Cells were passed through a 20 μm filter before experiments to remove any aggregates that would clog the device. Cell trajectories were observed during experiments using chlorophyll fluorescence by epifluorescent microscopy using excitation from a Hg lamp and a chlorophyll longpass filter (Chroma). After experiments were completed, fluids were disposed of in a 10% bleach solution and manifold and tubing were rinsed with a 10% bleach solution and then soaked in 1% bleach in DI water until their next use. Glass lids were removed from silicon devices and devices were rinsed with bleach, Contrad 70, and soaked in DI water until their next use. Before reuse, devices were rinsed with acetone and isopropanol, dried, and cleaned in oxygen plasma for 90 s.

6.3.3 Results

Array performance was first confirmed by observing the trajectory of cells in the device with epifluorescence microscopy. Chlorella cells, with an average size of 3.6

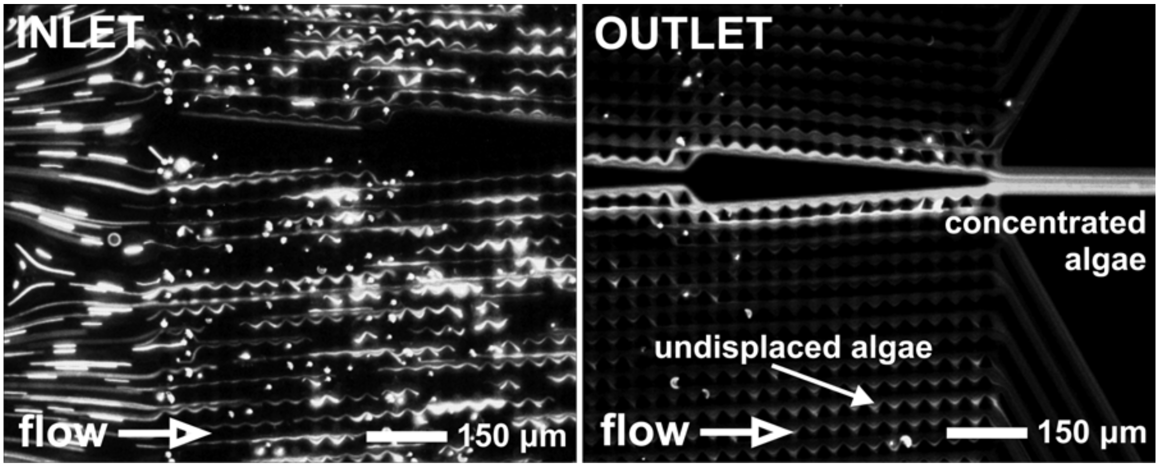

Figure 6.5: **Algae Concentration in Device.** Trajectories of chlorella algae in an array with 12 μm gaps, 1/15 array tilt, and 2.5 μm critical particle size at device inlet and outlet. Cells, visualized by chlorophyll fluorescence, are evenly dispersed at inlet but are concentrated against central wall at outlet and directed to narrow collection outlet.

μm were flowed through the device at a flow rate of 1 mL/min. As shown in Figure 6.5, dispersed cells enter the array from a single inlet and are directed towards the central channel wall. At the device outlet, concentrated algae are directed into the the collection output channel. There is a portion of the algae that are not displaced by the array that can be seen as streaks entering the wider waste channels. These cells are likely to be below the critical size in the array. Because these algae split into four or more algae when they divide[64], there can be a large variation in cell size. It may be possible to decrease the array dimensions to capture these smaller cells, but this must be balanced against the increased likelihood of clogging the array with larger cells.

Separation efficiency was then quantified by measuring the algae density in two output channels with a Coulter counter with a 2.2 μm threshold. 3.7 mL of algae culture with 3.4x10^8 cells/mL and average size 4.4 μm was processed at a flow rate of 1 mL/min before the device clogged. From this, 0.15 mL of solution with a cell density of 3.3x10^9 cells/mL and average size of 4.6 μm went to the collection channel while 3.55 mL of solution with cell density of 1.2x10^8 cells/mL with average size 4.3 μm.

From this, we can see that the device provides a 10 times increase in concentration in a greatly reduced volume (3.7 mL to 0.15 mL). Taking the volume into account, we get 51% of the cells in the collection output. This low capture efficiency is likely due to the array clogging diverting the flow and leading to deviations from the expected particle trajectories.

6.3.4 Scalability

While these experiments were performed with a single layer device, industrial application of this technique will require thousands to millions of arrays to be run in parallel. As such, it will be useful to discuss the device footprint. Because the diameter of the device through holes (1 mm) is much greater than the channel dimensions ($\sim 10\,\mu m$) and the resistance scales as the smallest dimension cubed, a deep stack of through holes can be considered a zero resistance connection and we will consider stacks of devices as operating in parallel with the same applied pressure gradient. 1300 L of algal culture must be processed to produce 1 L of oil from algae with a mass density of 1.5 g/L in culture and 40% lipid by weight [2]. The footprint of a single device is 40 x 25 x 1 mm with a PDMS gasket seal while the manifold is 60 x 40 x 15 mm. If we stack 100 devices etched 100 μm deep with flow rates of 1 mL/min/layer, we'll need 217 100-device stacks to process 1300 L/hr. Rounding to 220 stacks gives a footprint of 60x90x12 cm. Since we are interested in conserving energy, passive operation using the pressure head from a raised tank would be the preferred operation method. The pressure required to drive fluid at 1 mL/min in the algae devices was measured to be 20 psi. Since we are increasing the etch depth from 60 μm to 100 μm, we will need less pressure to get the same flow rate - 12 psi or 28 feet of water to passively drive the devices at 1300 L/hr flow rates. In the previous section, we showed that the device provided cells in a volume that was about a 25 times less than the input volume (3.7 mL to 0.15 mL). Using this volume reduction, we'll get 54 L of concen-

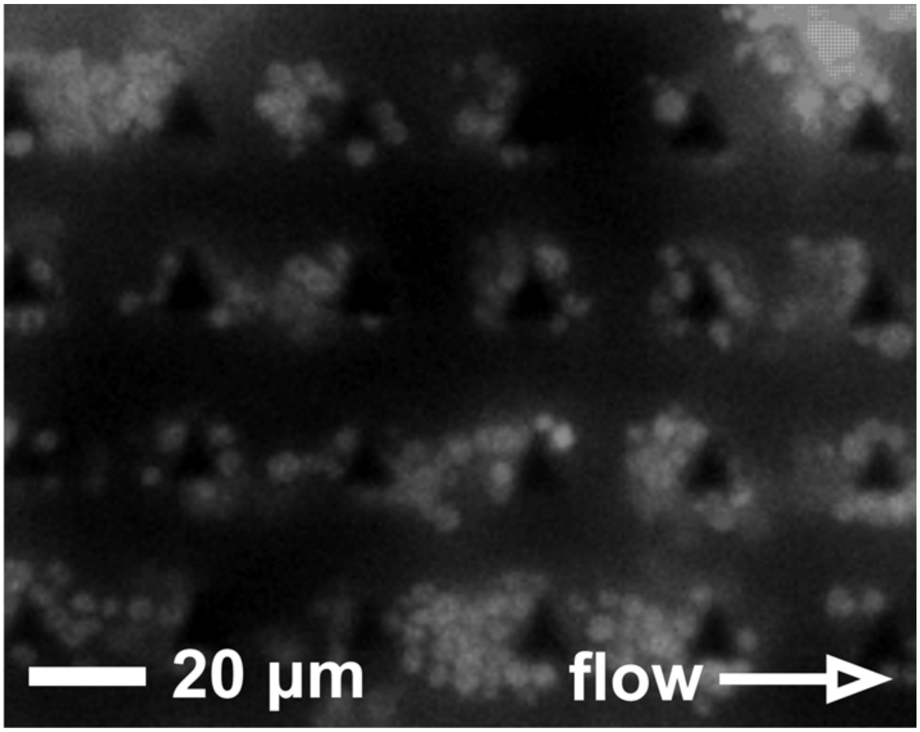

Figure 6.6: Algae clog the array by sticking to device surfaces and then to each other. They are most likely to stick in the region between posts where the fluid velocity is low.

trated algae solution from 1300 L of algal culture that may be further dewatered by drying or other techniques [41]. If we assume that yield remains limited to around 50%, twice as many devices will be needed get 1 L of oil per hour. In general, this argument shows that we would need about 1 m^2 of space per liter of biofuel we hoped to produce per hour.

6.3.5 Clogging

We examined array clogging and found that the source was algae sticking to post surfaces and then to each other. The usual source of clogging in DLD arrays is large particles building up at the inlet to the array, eventually creating a dense plug that prevents fluid from entering the array. However, we observe that the source of clogging with algae is cells adhering to surfaces. This is shown in Figure 6.6 with Neochloris oleoabundans cells in an array with 20 μm gaps, 10 μm posts, and 1/20 array tilt at 1 mL/min flow rate. Most of the cells are stuck in the region between posts, where the flow rate tends to be slowest, but the cells also stick to each other and eventually clog the array. In addition to F108 surfactant, BSA was also added to the running solution to try to reduce cell adhesion, but it showed limited effectiveness. It is possible that cell sticking is a stress response akin to flocculation[34]. PEG-based coatings were not attempted, but are the next common method to attempt [37].

6.3.6 Future Directions

Industrial scale application of DLD arrays will require new materials and manufacturing methods as the silicon microfabrication techniques used here are prohibitively expensive. A more suitable manufacturing method would be hot embossing or injection molding [3], that could produce many devices quickly with cheap materials using a single mold. There is a great deal of room for optimization in the design to increase throughput per device and optimize the footprint. The devices presented here were meant to demonstrate the capabilities of the DLD array for dewatering algae for biofuel production and should serve only as a template upon which to build more advanced designs. A non-stick coating, better understanding of what causes algae to stick to surfaces, or some other method that prevents cell adhesion is essential for the application of this technique. Finally, finding a larger algae cell with similar oil production capabilities may be a useful endeavor that will allow throughput to increase quadratically following the discussion of the array resistance's relationship to the critical particle size.

Chapter 7

Conclusion

7.1 Summary

We hope to have shown that deterministic lateral displacement (DLD) arrays are a powerful tool for particle separation and manipulation. We began with a discussion of performing sequential on-chip chemical treatments using the DLD array to direct particles in the "bumping" trajectory across co-flowing reagent streams and demonstrated the utility of this method by performing on-chip platelet label and washing and *E. Coli* lysis and chromosomal separation. This was followed by an analysis of washing between treatment streams and a discussion of how to design treatment stages to obtain sufficient washing in between steps.

We developed a deterministic microfluidic ratchet that could separate particles in an intermediate size range using a DLD array with triangular posts in an oscillating flow. We identified the mechanism of separation as resulting from skewed flow profile between posts caused by the triangular posts. This causes a direction-dependent critical particle size that was characterized by numerical simulation and found to show excellent agreement with experimental results. We discussed the observation of anisotropic conduction in arrays with right triangular posts and how to mitigate this affect in further applications.

We then extended this idea of using triangular posts in DLD arrays to continuous-flow operation and showed significant performance enhancements over arrays with circular posts when the triangle vertex is used as the displacement edge. With a combination of experiments and simulation that arrays with triangular posts, we showed that arrays with triangular posts have higher throughput and less clogging because the gap between posts can be increased while maintaining a fixed critical particle size. An exploration of other post shapes was performed to optimized the post shape and it was found that equilateral triangular posts at least twice the size of the gap should be used in most applications.

Taking this idea of increasing device throughput to the next step, we developed a highly parallelized DLD array architecture for processing macroscopic fluid volumes by operating many arrays in parallel and showed flow rates on the order of 10 mL/min with a single-layer device. With internal velocities exceeding 1 m/s, we showed that the DLD array continues to function even outside of the low Re regime and this flow rate represents the fastest ever operation of a DLD array and the highest reported flow rate in any microfluidic sorting application. We developed a spring-loaded manifold to accommodate high pressure operation of these devices and allow multiple devices to be stacked vertically using a PDMS gasket in between silicon layers.

Finally, we developed two applications to take advantage of high throughput DLD arrays. We demonstrated that the DLD array can be used to isolate quickly isolate circulating tumor cells from blood by showing high efficiency capture of cancer-related epithelial cells spiked in blood with no effect on cell vitality and little concentration of background white blood cells. We then showed the DLD array can be used to passively concentrate of algae for biofuel production and characterized the capture efficiency, concentration capabilities, and discussed considerations of scaling these devices up to handle the thousands of liters that will be necessary for industrial applications.

7.2 Future Work

Broad scale application of DLD arrays will require new materials and manufacturing methods as the silicon microfabrication techniques used here are prohibitively expensive. A more suitable manufacturing method would be rely on plastics that can be produced quickly using inexpensive materials. While important array parameters (critical size, wall design, post design) have been thoroughly explored and are well understood, more work in understanding and optimizing the inlet and outlet structures that connect microfluidic channels to macroscopic fluid reservoirs is will be useful to ensure that flow into the arrays occurs as designed.

While we have shown that high flow rates are possible, there is a great deal of room for layout optimization to increase the cross-sectional area available for separation per device and optimize the footprint. Further, the development of a robust nonstick coating will be vital to ensure devices continue to function after processing samples containing billions to trillions of cells. Finally, a careful analysis of inertial effects on particle motion in DLD arrays is likely to prove fruitful in understanding what additional considerations need to be taken when we leave the low Re regime to pursue higher flow rates.

Appendix A

Publications and Presentations

A.1 Peer-reviewed Publications

- **K Loutherback**, J D'Silva, L Liu, S Vyawahare, C Lane, RH Austin, and JC Sturm. Stacking and Parallelization of Microfluidic Devices for High Throughput Cell Separations. (in preparation)
- **K Loutherback**, J D'Silva, A Wu, L Liu, RH Austin, JC Sturm. Continuous High Throughput Enrichment of Viable Circulating Tumor Cells with Deterministic Lateral Displacement Arrays. (in preparation)
- **K Loutherback**, KS Chou, J Newman, J Puchalla, RH Austin, and JC Sturm. Improved Performance of Deterministic Lateral Displacement Arrays with Triangular Posts. Microfluidics and Nanofluidics 9, no.6 (2010):1143-1149.
- L Liu, **K Loutherback**, D Yeater, G Lambert, et al. A Microfluidic Device for Continuous Cancer Cell Culture and Passage with Hydrodynamic Forces. Lab on a Chip 10, no. 14 (2010): 1807-1813.
- **K Loutherback**, J Puchalla, RH Austin, and JC Sturm. Deterministic Microfluidic Ratchet. Physical Review Letters 102 (2009): 045301.

- KJ Morton, **K Loutherback**, DW Inglis, et al. Crossing Microfluidic Streamlines to Lyse, Label and Wash Cells. Lab on a Chip 8, no. 9 (2008): 1448-1453.
- KJ Morton, **K Loutherback**, DW Inglis, et al. Hydrodynamic Metamaterials: Microfabricated Arrays to Steer, Refract, and Focus Streams of Biomaterials. PNAS 105, no. 21 (2008): 7434-7438.

A.2 Conference Presentations

- **Gordon Research Conference Microfluidics 2011**, Waterville Valley, NH - High Throughput Microfluidic Enrichment of Viable Cancer Cells. (poster)
- **MRS Fall Meeting 2010**, Boston, MA - Parallelized Microfluidic Separations for Large-scale Dewatering of Biofuel Algae. (poster)
- **APS March Meeting 2010**, Portland, OR - Improved Performance of Deterministic Lateral Displacement Arrays with Triangular Posts. (talk)
- **MRS Spring Meeting 2009**, San Francisco, CA - Critical Size, Dynamic Range, and Throughput Improvements in Sorting by Deterministic Lateral Displacement Enabled by Triangular Posts. (talk)
- **APS March Meeting 2009**, Pittsburgh, PA - Deterministic Microfluidic Ratchet. (talk)
- **APS March Meeting 2008**, New Orleans, LA - Crossing Streamlines to Lyse, Label, and Wash Cells. (talk)

Bibliography

[1] J. Atencia and D.J. Beebe. Controlled microfluidic interfaces. *Nature*, 437(7059):648–655, 2004.

[2] J.T. Bargiel. Commercialization of lateral displacement array for dewatering of microalgae. Master's thesis, Case Western Reserve University, 2009.

[3] H. Becker and L.E. Locascio. Polymer microfluidic devices. *Talanta*, 56(2):267–287, 2002.

[4] A.A.S. Bhagat, H.W. Hou, L.D. Li, C.T. Lim, and J. Han. Pinched flow coupled shear-modulated inertial microfluidics for high-throughput rare blood cell separation. *Lab Chip*, 2011.

[5] A.A.S. Bhagat, S.S. Kuntaegowdanahalli, and I. Papautsky. Continuous particle separation in spiral microchannels using dean flows and differential migration. *Lab Chip*, 8(11):1906–1914, 2008.

[6] D.C. Birdsell and E.H. Cota-Robles. Production and ultrastructure of lysozyme and ethylenediaminetetraacetate-lysozyme spheroplasts of escherichia coli. *Journal of bacteriology*, 93(1):427, 1967.

[7] Y. Chisti. Biodiesel from microalgae. *Biotechnology Advances*, 25(3):294–306, 2007.

[8] C.F. Chou, O. Bakajin, S.W.P. Turner, T.A.J. Duke, S.S. Chan, E.C. Cox, H.G. Craighead, and R.H. Austin. Sorting by diffusion: An asymmetric obstacle course for continuous molecular separation. *Proceedings of the National Academy of Sciences of the United States of America*, 96(24):13762, 1999.

[9] M. Cristofanilli, G.T. Budd, M.J. Ellis, A. Stopeck, J. Matera, M.C. Miller, J.M. Reuben, G.V. Doyle, W.J. Allard, L.W.M.M. Terstappen, et al. Circulating tumor cells, disease progression, and survival in metastatic breast cancer. *New England Journal of Medicine*, 351(8):781–791, 2004.

[10] N. Darnton, O. Bakajin, R. Huang, B. North, JO Tegenfeldt, EC Cox, J. Sturm, and RH Austin. Hydrodynamics in 21/2 dimensions: making jets in a plane. *Journal of Physics: Condensed Matter*, 13:4891, 2001.

[11] J.A. Davis, D.W. Inglis, K.J. Morton, D.A. Lawrence, L.R. Huang, S.Y. Chou, J.C. Sturm, and R.H. Austin. Deterministic hydrodynamics: Taking blood apart. *Proceedings of the National Academy of Sciences*, 103(40):14779, 2006.

[12] I. Derényi and D.R. Astumian. Ac separation of particles by biased brownian motion in a two-dimensional sieve. *Phys. Rev. E*, 58(6):7781–7784, 1998.

[13] D. Di Carlo. Inertial microfluidics. *Lab Chip*, 9(21):3038–3046, 2009.

[14] D. Di Carlo, D. Irimia, R.G. Tompkins, and M. Toner. Continuous inertial focusing, ordering, and separation of particles in microchannels. *Proceedings of the National Academy of Sciences*, 104(48):18892, 2007.

[15] L. Dintenfass. *Blood microrheology: viscosity factors in blood flow, ischaemia, and thrombosis: an introduction to molecular and clinical haemorheology.* Appleton-Century-Crofts, 1971.

[16] D. Erickson and D. Li. Integrated microfluidic devices. *Analytica Chimica Acta*, 507(1):11–26, 2004.

[17] R.P. Feynman, R.B. Leighton, and M. Sands. *The Feynman Lectures on Physics.* Addison-Wesley, 1966.

[18] R.A. Freitas. *Nanomedicine, volume I: Basic capabilities.* Landes Bioscience Georgetown, TX, 1999.

[19] V.I. Furdui, J.K. Kariuki, and D.J. Harrison. Microfabricated electrolysis pump system for isolating rare cells in blood. *Journal of Micromechanics and Microengineering*, 13:S164, 2003.

[20] D.R. Gossett, W.M. Weaver, A.J. Mach, S.C. Hur, H.T.K. Tse, W. Lee, H. Amini, and D. Di Carlo. Label-free cell separation and sorting in microfluidic systems. *Anal Bioanal Chem*, 397(8):3249–3267, 2010.

[21] J. Happel and H. Brenner. *Low Reynolds number hydrodynamics.* D. Reidel Publishing Co., Hingham, MA, 1983.

[22] S.H. Holm, J.P. Beech, M.P. Barrett, and J.O. Tegenfeldt. Separation of parasites from human blood using deterministic lateral displacement. *Lab Chip*, 2011.

[23] X. Hu, P.H. Bessette, J. Qian, C.D. Meinhart, P.S. Daugherty, and H.T. Soh. Marker-specific sorting of rare cells using dielectrophoresis. *Proceedings of the National Academy of Sciences of the United States of America*, 102(44):15757, 2005.

[24] L.R. Huang, E.C. Cox, R.H. Austin, and J.C. Sturm. Continuous particle separation through deterministic lateral displacement. *Science*, 304(5673):987, 2004.

[25] R. Huang, TA Barber, MA Schmidt, RG Tompkins, M. Toner, DW Bianchi, R. Kapur, and WL Flejter. A microfluidics approach for the isolation of nucleated red blood cells (nrbcs) from the peripheral blood of pregnant women. *Prenatal diagnosis*, 28(10):892–899, 2008.

[26] S.C. Hur, N.K. Henderson-MacLennan, E.R.B. McCabe, and D. Di Carlo. Deformability-based cell classification and enrichment using inertial microfluidics. *Lab Chip*, 2011.

[27] S.C. Hur, A.J. Mach, and D. Di Carlo. High-throughput size-based rare cell enrichment using microscale vortices. *Biomicrofluidics*, 5:022206, 2011.

[28] D.W. Inglis. Efficient microfluidic particle separation arrays. *Applied Physics Letters*, 94:013510, 2009.

[29] D.W. Inglis, J.A. Davis, R.H. Austin, and J.C. Sturm. Critical particle size for fractionation by deterministic lateral displacement. *Lab on a Chip*, 6(5):655–658, 2006.

[30] D.W. Inglis, J.A. Davis, T.J. Zieziulewicz, D.A. Lawrence, R.H. Austin, and J.C. Sturm. Determining blood cell size using microfluidic hydrodynamics. *Journal of immunological methods*, 329(1-2):151–156, 2008.

[31] D.W. Inglis, N. Herman, and G. Vesey. Highly accurate deterministic lateral displacement device and its application to purification of fungal spores. *Biomicrofluidics*, 4:024109, 2010.

[32] D.W. Inglis, M. Lord, and R.E. Nordon. Scaling deterministic lateral displacement arrays for high throughput and dilution-free enrichment of leukocytes. *Journal of Micromechanics and Microengineering*, 21:054024, 2011.

[33] D.W. Inglis, K.J. Morton, J.A. Davis, T.J. Zieziulewicz, D.A. Lawrence, R.H. Austin, and J.C. Sturm. Microfluidic device for label-free measurement of platelet activation. *Lab Chip*, 8(6):925–931, 2008.

[34] G.A. Jackson. A model of the formation of marine algal flocs by physical coagulation processes. *Deep Sea Research Part A. Oceanographic Research Papers*, 37(8):1197–1211, 1990.

[35] R.J. Jankowski, C. Haluszczak, M. Trucco, and J. Huard. Flow cytometric characterization of myogenic cell populations obtained via the preplate technique: potential for rapid isolation of muscle-derived stem cells. *Human gene therapy*, 12(6):619–628, 2001.

[36] P.J.A. Kenis, R.F. Ismagilov, and G.M. Whitesides. Microfabrication inside capillaries using multiphase laminar flow patterning. *Science*, 285(5424):83, 1999.

[37] P. Kingshott, S. McArthur, H. Thissen, D.G. Castner, and H.J. Griesser. Ultrasensitive probing of the protein resistance of peg surfaces by secondary ion mass spectrometry. *Biomaterials*, 23(24):4775–4785, 2002.

[38] J.B. Knight, A. Vishwanath, J.P. Brody, and R.H. Austin. Hydrodynamic focusing on a silicon chip: mixing nanoliters in microseconds. *Physical Review Letters*, 80(17):3863–3866, 1998.

[39] Z.S. Lalmahomed, J. Kraan, J.W. Gratama, B. Mostert, S. Sleijfer, and C. Verhoef. Circulating tumor cells and sample size: the more, the better. *Journal of Clinical Oncology*, 28(17):e288, 2010.

[40] J. Laufer. *Investigation of turbulent flow in a two-dimensional channel.* PhD thesis, California Institute of Technology, 1948.

[41] Y. Li, M. Horsman, N. Wu, C.Q. Lan, and N. Dubois-Calero. Biofuels from microalgae. *Biotechnology progress*, 24(4):815–820, 2008.

[42] H.K. Lin, S. Zheng, A.J. Williams, M. Balic, S. Groshen, H.I. Scher, M. Fleisher, W. Stadler, R.H. Datar, Y.C. Tai, et al. Portable filter-based microdevice for detection and characterization of circulating tumor cells. *Clinical Cancer Research*, 16(20):5011, 2010.

[43] R. Lindken, M. Rossi, S. Gro, and J. Westerweel. Micro-particle image velocimetry ([small micro] piv): Recent developments, applications, and guidelines. *Lab on a Chip*, 9(17):2551–2567, 2009.

[44] K. Loutherback, K.S. Chou, J. Newman, J. Puchalla, R.H. Austin, and J.C. Sturm. Improved performance of deterministic lateral displacement arrays with triangular posts. *Microfluidics and nanofluidics*, pages 1–7, 2010.

[45] K. Loutherback, J. Puchalla, R.H. Austin, and J.C. Sturm. Deterministic microfluidic ratchet. *Physical Review Letters*, 102(4):45301, 2009.

[46] H. Lu, S. Gaudet, M.A. Schmidt, and K.F. Jensen. A microfabricated device for subcellular organelle sorting. *Analytical chemistry*, 76(19):5705–5712, 2004.

[47] D. Magde, E.L. Elson, and W.W. Webb. Fluorescence correlation spectroscopy. ii. an experimental realization. *Biopolymers*, 13(1):29–61, 1974.

[48] S. Maheswaran and D.A. Haber. Circulating tumor cells: a window into cancer biology and metastasis. *Current opinion in genetics & development*, 20(1):96–99, 2010.

[49] S. Matthias and F. Muller. Asymmetric pores in a silicon membrane acting as massively parallel brownian ratchets. *Nature*, 424(6944):53–57, 2003.

[50] S. Meng, D. Tripathy, E.P. Frenkel, S. Shete, E.Z. Naftalis, J.F. Huth, P.D. Beitsch, M. Leitch, S. Hoover, D. Euhus, et al. Circulating tumor cells in patients with breast cancer dormancy. *Clinical cancer research*, 10(24):8152, 2004.

[51] K.J. Morton, K. Loutherback, D.W. Inglis, O.K. Tsui, J.C. Sturm, S.Y. Chou, and R.H. Austin. Crossing microfluidic streamlines to lyse, label and wash cells. *Lab Chip*, 8(9):1448–1453, 2008.

[52] K.J. Morton, K. Loutherback, D.W. Inglis, O.K. Tsui, J.C. Sturm, S.Y. Chou, and R.H. Austin. Hydrodynamic metamaterials: Microfabricated arrays to steer, refract, and focus streams of biomaterials. *Proceedings of the National Academy of Sciences*, 105(21):7434, 2008.

[53] KJ Morton, JC Sturm, RH Austin, and SY Chou. Nanoimprinted fluidic device for continuous separation of nanoparticles. *Proc of* μ *TAS*, 1:1014–1016, 2006.

[54] S. Nagrath, L.V. Sequist, S. Maheswaran, D.W. Bell, D. Irimia, L. Ulkus, M.R. Smith, E.L. Kwak, S. Digumarthy, A. Muzikansky, et al. Isolation of rare circulating tumour cells in cancer patients by microchip technology. *Nature*, 450(7173):1235–1239, 2007.

[55] M.N. Ozisik. *Heat conduction*, volume 300. John Wiley & Sons New York., 1993.

[56] N. Pamme. Continuous flow separations in microfluidic devices. *Lab Chip*, 7(12):1644–1659, 2007.

[57] J. Pipper, M. Inoue, L.F.P. Ng, P. Neuzil, Y. Zhang, and L. Novak. Catching bird flu in a droplet. *Nature medicine*, 13(10):1259–1263, 2007.

[58] C. Prinz, J.O. Tegenfeldt, R.H. Austin, E.C. Cox, and J.C. Sturm. Bacterial chromosome extraction and isolation. *Lab Chip*, 2(4):207–212, 2002.

[59] E.M. Purcell. Life at low reynolds number. *Am. J. Phys*, 45(3):11, 1977.

[60] A. Rida and MAM Gijs. Manipulation of self-assembled structures of magnetic beads for microfluidic mixing and assaying. *Analytical chemistry*, 76(21):6239–6246, 2004.

[61] S. Riethdorf and K. Pantel. Advancing personalized cancer therapy by detection and characterization of circulating carcinoma cells. *Annals of the New York Academy of Sciences*, 1210(1):66–77, 2010.

[62] M.A. Shannon, P.W. Bohn, M. Elimelech, J.G. Georgiadis, B.J. Mariñas, and A.M. Mayes. Science and technology for water purification in the coming decades. *Nature*, 452(7185):301–310, 2008.

[63] H. Song, J.D. Tice, and R.F. Ismagilov. A microfluidic system for controlling reaction networks in time. *Angewandte Chemie*, 115(7):792–796, 2003.

[64] C. Sorokin and R.W. Krauss. Effects of temperature & illuminance on chlorella growth uncoupled from cell division. *Plant Physiology*, 37(1):37, 1962.

[65] T.M. Squires and S.R. Quake. Microfluidics: Fluid physics at the nanoliter scale. *Reviews of modern physics*, 77(3):977, 2005.

[66] H.A. Stone, A.D. Stroock, and A. Ajdari. Engineering flows in small devices. *Annu. Rev. Fluid Mech.*, 36:381–411, 2004.

[67] S.L. Stott, C.H. Hsu, D.I. Tsukrov, M. Yu, D.T. Miyamoto, B.A. Waltman, S.M. Rothenberg, A.M. Shah, M.E. Smas, G.K. Korir, et al. Isolation of circulating tumor cells using a microvortex-generating herringbone-chip. *Proceedings of the National Academy of Sciences*, 107(43):18392, 2010.

[68] A.D. Stroock, S.K.W. Dertinger, A. Ajdari, I. Mezić, H.A. Stone, and G.M. Whitesides. Chaotic mixer for microchannels. *Science*, 295(5555):647, 2002.

[69] Y. Takami, S. Yamane, K. Makinouchi, J. Glueck, and Y. Nosé. Mechanical white blood cell damage in rotary blood pumps. *Artificial organs*, 21(2):138–142, 1997.

[70] J.O. Tegenfeldt, C. Prinz, H. Cao, R.L. Huang, R.H. Austin, S.Y. Chou, E.C. Cox, and J.C. Sturm. Micro-and nanofluidics for dna analysis. *Analytical and bioanalytical chemistry*, 378(7):1678–1692, 2004.

[71] J. Theron, JA Walker, and TE Cloete. Nanotechnology and water treatment: applications and emerging opportunities. *Critical reviews in microbiology*, 34(1):43–69, 2008.

[72] D. Therriault, S.R. White, and J.A. Lewis. Chaotic mixing in three-dimensional microvascular networks fabricated by direct-write assembly. *Nature Materials*, 2(4):265–271, 2003.

[73] D. Tilman, R. Socolow, J.A. Foley, J. Hill, E. Larson, L. Lynd, S. Pacala, J. Reilly, T. Searchinger, C. Somerville, et al. Beneficial biofuels—the food, energy, and environment trilemma. *Science*, 325(5938):270, 2009.

[74] A. Van Oudenaarden and S.G. Boxer. Brownian ratchets: molecular separations in lipid bilayers supported on patterned arrays. *Science*, 285(5430):1046, 1999.

[75] G. Vona, A. Sabile, M. Louha, V. Sitruk, S. Romana, K. Schutze, F. Capron, D. Franco, M. Pazzagli, M. Vekemans, et al. Isolation by size of epithelial tumor cells: A new method for the immunomorphological and molecularcharacterization of circulating tumor cells. *American Journal of Pathology*, 156(1):57, 2000.

[76] B.H. Weigl and P. Yager. Microfluidic diffusion-based separation and detection. *Science*, 283(5400):346, 1999.

[77] FM White. *Viscous fluid flow*. McGraw Hill, 2006.

[78] P. Yager, T. Edwards, E. Fu, K. Helton, K. Nelson, M.R. Tam, and B.H. Weigl. Microfluidic diagnostic technologies for global public health. *Nature*, 442(7101):412–418, 2006.

[79] C. Yi, C.W. Li, S. Ji, and M. Yang. Microfluidics technology for manipulation and analysis of biological cells. *Analytica Chimica Acta*, 560(1-2):1–23, 2006.

[80] S. Zheng, H. Lin, J.Q. Liu, M. Balic, R. Datar, R.J. Cote, and Y.C. Tai. Membrane microfilter device for selective capture, electrolysis and genomic analysis of human circulating tumor cells. *Journal of Chromatography A*, 1162(2):154–161, 2007.